UNIVERSITAT POLITÈCNICA DE VALÈNCIA

ESCUELA TÉCNICA SUPERIOR INGENIEROS INDUSTRIALES VALENCIA

TRABAJO FIN DE MASTER EN INGENIERÍA INDUSTRIAL

STUDY OF THE SET UP OF A FLUID STRUCTURE COUPLING INTERFACE (FSI) BETWEEN PWR FUEL ASSEMBLIES AND THE REACTOR COOLANT

AUTHOR: JAIME G. RUIZ ANTÓN-PACHECO

SUPERVISOR: RAFAEL MIRÓ HERRERO

SUPERVISOR RAFAEL JUAN MACIÁN (TUM)

Academic year: 2016-17

Acknowledgements

"First of all I would like to thank Prof. Dr. Macián-Juan for giving me the opportunity to carry out this Project in the Department of Nuclear Engineering. I have learnt a lot from his knowledge, expertise and extensive experience in the field of nuclear engineering and fluid mechanics.

I would also like to express my deepest gratitude to Dipl. Ing. Andreas Wanninger for his guidance and disposition towards this Thesis. I am enormously thankful for his constant patience and for his willingness to help when complicated problems appeared, while always maintaining the most positive of attitudes. Having learnt so much from this Thesis would have not been possible without him. I truly wish him all the best for his future and thank him for being my mentor during these months.

Many thanks indeed to Prof. Rafael Miró Herrero for his guidance in the readaptation of this Thesis to the requirements of my home university (UPV). His willingness to help and his support in the conversion of this work have meant a lot.

Besides this, I also want to thank my parents (Manuel and Marina) and older brother (Manu) for there continuous support despite of being so far away. Thank you for teaching me the value of endeavor, commitment and of work well done in order to reach your personal goals.

One last and special thank you has to be said to my fellow companion and great friend Luis Rafecas. With him I have shared the day-to-day basis of this Thesis, making these months truly unforgettable, and taking with me the best possible memories of the long hours in the PC Raum. I am sure this has just been the first chapter of many to come in our great friendship".

Erklärung

Hiermit versichere ich, die vorliegende Arbeit selbstständig und ohne Hilfe Dritter angefertigt zu haben. Gedanken und Zitate, die ich aus fremden Quellen direkt oder indirekt übernommen habe, sind als solche kenntlich gemacht. Diese Arbeit hat in gleicher oder ähnlicher Form noch keiner Prüfungsbehörde vorgelegen und wurde bisher nicht veröffentlicht.

Ich erkläre mich damit einverstanden, dass die Arbeit durch den Lehrstuhl für Nukleartechnik der Öffentlichkeit zugänglich gemacht werden kann.

Report of authenticity of the original Master Thesis work carried out under the Double Degree Prorgam framework with the Technical Univeristy of Munich in the academic year 2015-16.

München, den 30.08.16

Jaime Ruiz

Abstract

Fuel Assemblies within the core of Pressurized Water Reactor (PWR) are affected by the bow phenomenon. This in turn impacts the performance of nuclear Power Plants. Bowing leads to the appearance of bending moments in the fuel rods, therefore the whole Fuel Assembly structure is deformed (as the fuel rods are tightly held together by spacer grids).

An excessively distorted FA can induce both safety and operational problems to the reactor. With respect to the safety impact, deformation of the FA can interfere in the correct insertion and functionality of Control Rods. These are in charge of regulating and controlling the nuclear chain fission reaction in the core and, hence, Incomplete Rod Insertion (IRI) episodes will represent a potential threat should there be a Scram event or the necessity for a quick shutdown. On the other hand, FA distortion also induces performance problems. The irregular shape of the FAs will originate unequal gaps through which the coolant (H20) will flow, and this will affect the Thermal Margins that will no longer be optimal for operation.

As bowing involves many different processes, it becomes a challenging issue to predict. For this reason, several computational models have been created over the last years attempting to predict FA bow. The objective of this Thesis is to implement a Fuel-Structure Interaction model (FSI) to predict the effect of Lateral Hydraulic Forces on the Fuel Assembly Core Structure AND vice-versa.

As Lateral Hydraulic Forces are thought to be the drivers of the FA bow, results should show a considerable difference between one and the other. However, it must also be taken into account that there are other causes of bow such as excessive hold down forces or irradiation induced creep that can also influence the phenomenon and the outcome.

A Porous Medium Approach will be considered in this research to simulate the hydraulics of a PWR Fuel Assembly.

Key words: Fluid Structure Interaction Interface, bow phenomenon, hydraulics, PWR coolant, fuel assemblies.

Table of Contents

DOCUMENTS CONTAINED IN THIS MASTER THESIS:

- **Thesis Report**
- **Thesis Budget**

THESIS REPORT:

THESIS BUDGET:

List of Figures

List of Tables

THESIS REPORT:

THESIS BUDGET:

List of Equations

List of Acronyms

PWR	Pressurized Water Reactor
FA	Fuel Assembly
FEM	Finite Element Method
FR	Fuel Rod
GT	Guide Tube
IRI	Incomplete Rod Insertion
APDL	Ansys Paramteric Design Language
CFD	Computational Fluid Dynamics
ANSYS CFX	Analysis of Systems for Computational Fluids
CV	Control Volume
RS	Reference System
RDT	Reynolds Drag Theorem
EOC	End of Cycle

THESIS REPORT

1 Introduction

1.1 General Interest of the Work

As stated in the Copenhagen Accord, by 2030 global energy consumption is projected to be 55% higher than it is today [1]. This will be caused by very diverse factors such as increased population growth, continued urbanization, progressive industrialization of the developing countries, and economic expansion.

The modern world faces two main problems. On one hand, it is not yet clear how this growing energy demand will be satisfied, as most of the energy supplies derive from fossil fuel consumption. Fossil Fuels, by their very definition, will sooner or later run out. On the other hand, not only satisfying the increased need of energy, but also satisfying it in a sustainable way also seems a major challenge.

Renewable energies such as hydroelectric, wind, solar, biomass and geothermal are gaining considerable importance in the modern energy and electricity supply systems. Significant breakthroughs in their usage and optimization are being carried out and this, of course, is something on which further research has to be promoted. However, the collective capacity of these technologies to produce electricity in the decades ahead is limited, all natural resources acting as energy sources are unpredictable and change regardless of the energy demand at that time. This lack of reliability in the supply united with their high maintenance costs and the challenge of supplying whole economies of scale will limit their further development and, hence, create the need for a complementary source.

Nuclear Energy is the only proven option with the capacity to produce vastly expanded supplies of clean energy on a global scale. Far from being competitors, Nuclear Energy and Renewables are urgently needed as partners if the world´s immense clean energy needs are to be met. The study and optimization of Nuclear Energy Power Plants operation will, therefore, result in the benefit of all.

1.2 Pressurized Water Reactors (PWRs)

Pressurized Water Reactors (PWRs) are currently the most widely used type of nuclear Power Plants. PWRs obtain the thermal energy released by the fission of a nucleus of Uranium and use this energy to heat water that is used to produce steam. This steam will then drive a generator that will provide electrical energy.

A special characteristic of this reactor type is that the water flowing through the primary loop is kept at a very high pressure, so that boiling inside the reactor is prevented (something that could derive in the melting of the core). The reactor core contains the fuel and this is where the nuclear reaction takes place. Once the fission chain is running, the water flows up the reactor and is heated and used to produce steam within the steam generator. Thermal energy is hence transmitted to the secondary loop, where the lower pressures lead to the generation of steam. The steam then travels to the Power Plant Turbine where this thermal energy is

transformed into mechanical energy that will drive the generator. Finally, electrical energy is obtained from the generator. The reactor cycle is closed using the condenser. In the condenser, the steam coming from the turbine is condensed with cold water taken from an external source (a river, a lake or the sea). To restart the cycle again, the cooled condensed water is pumped through to the steam generator and the process is repeated. Figure 1 shows a diagram of the basic PWR configuration.

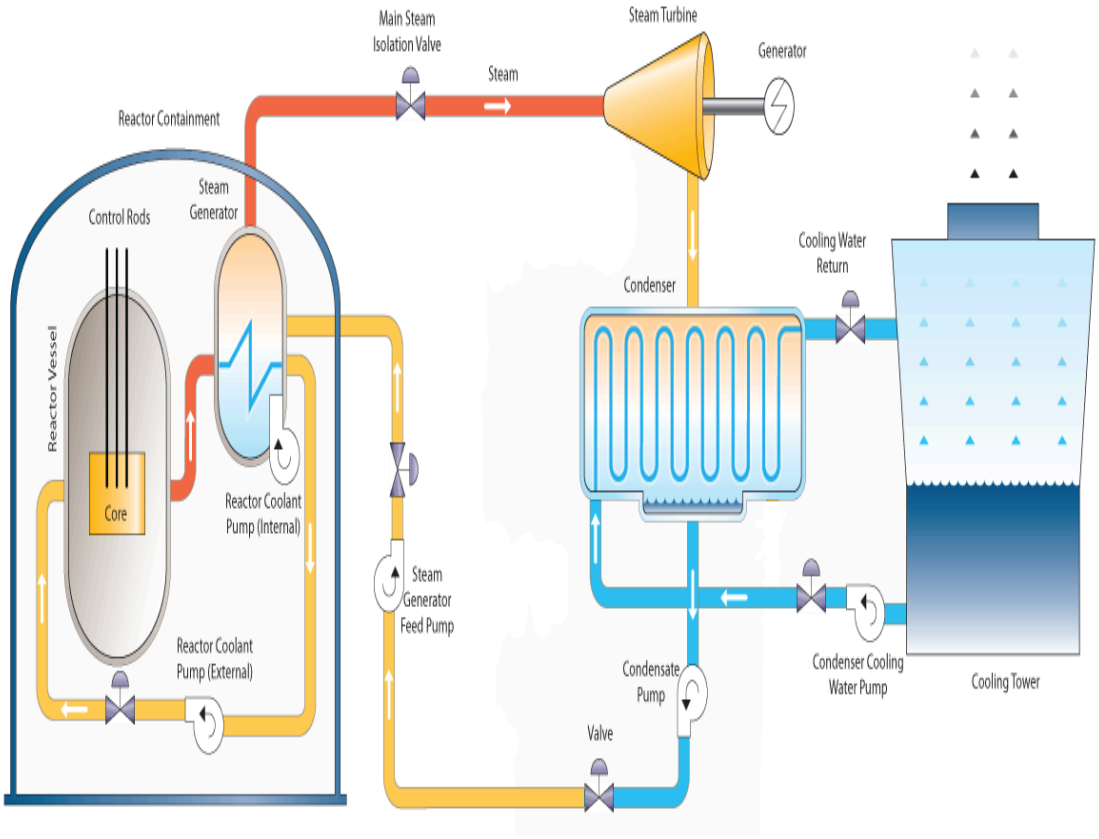

Figure 1: Typical PWR Power Plant Diagram [2].

1.2.1 Reactor Pressure Vessel

The Reactor Vessel consists of a big cylindrical structure in which the Fuel Assembly is contained. The coolant (H2O) enters the vessel through the coolant inlet nozzles and is distributed from the down-comer into the lower plenum, from there it enters the core from below. It travels up the core and through the Fuel Assembly Array and absorbs all the thermal heat coming from the fuel rods. After travelling through the core, the coolant flow is collected in the upper plenum and leaves the core through the coolant outlet nozzles. Figure 2 shows a cutaway of a typical Reactor Pressure Vessel, while Figure 3 shows a complete cross section of a PWR Reactor Pressure Vessel.

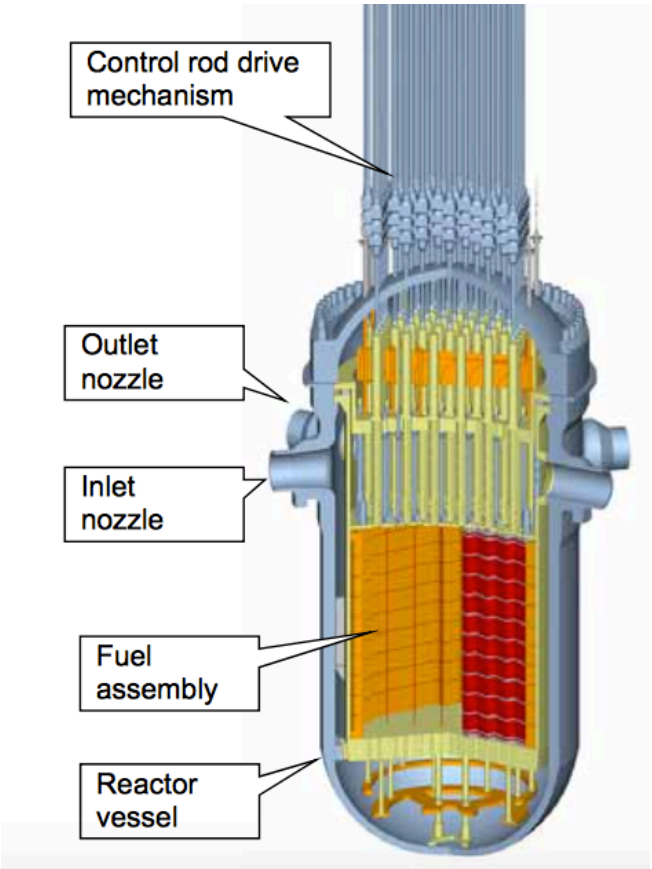

Figure 2: Cutaway of a PWR [3].

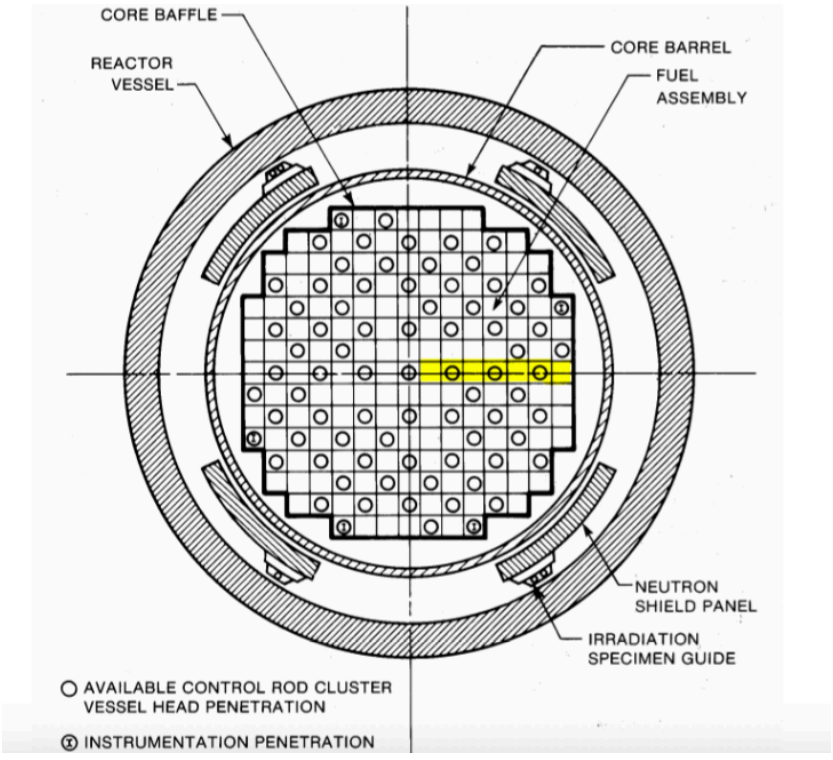

Figure 3: Cross Section of a PWR Core Vessel [3].

1.2.2 Fuel Assembly

The Fuel Assembly is the array structure in form of squares that represents the fuel rods gathered into bundles. Its top and bottom parts are fastened to guide thimbles, for the control rods and instrumentation. It also contains spacer grids (around 9) spaced along the length of the fuel rods. PWR Fuel Assemblies form a square lattice arrangement, with the top and bottom nozzles providing the mechanical support.

Within the Fuel Assembly, rods are placed forming a square matrix usually $17x17$ in dimensions, making a total of 289 rods of almost 4 m in length. However, not all of them contain fuel within their structure. A total amount of 264 rods contain fuel, while 24 are intended for the control rod guide Thimbles and the one left, for the instrumentation Thimble.

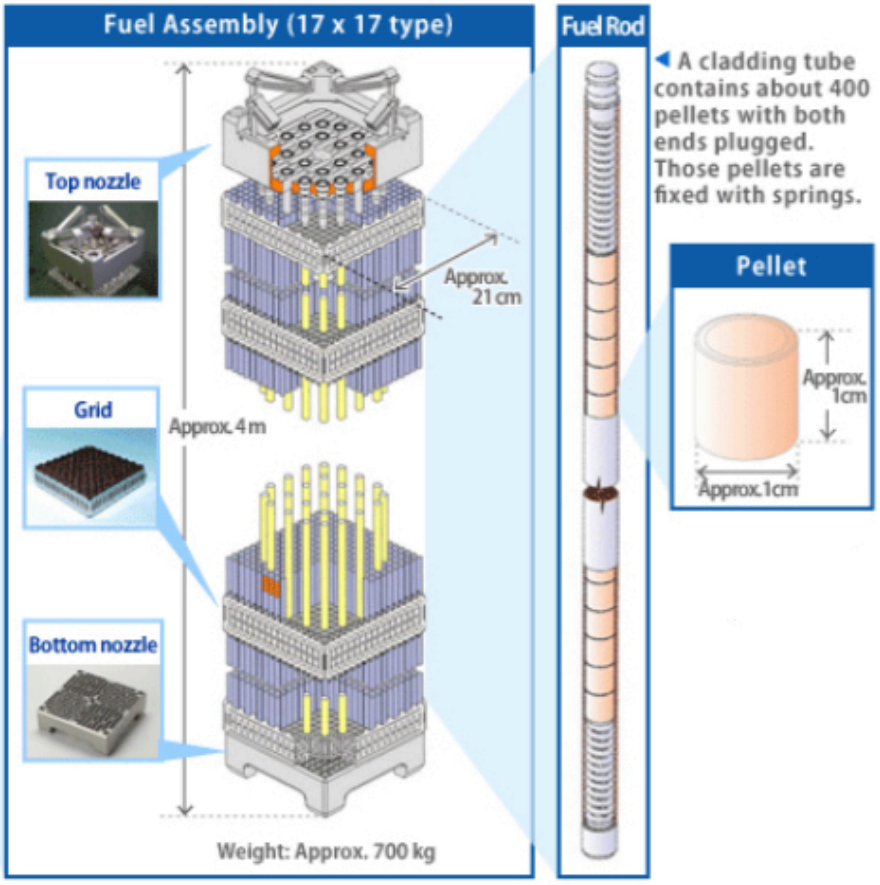

Figure 4: Fuel Assembly Structure and Configuration [3].

1.2.3 Fuel Rods and Fuel Pellets

Fuel Rods contain the nuclear fuel. This fuel is composed of enriched Uranium Powder (UO2) that has been condensed by cold sintering and pressing to form small pellets. Dimensions are shown in Figure 4. They are ceramic to be able to withstand very high temperatures. The Pellets are then inserted into tubes of Zircaloy, which are then filled with helium gas in order to enhance the heat convection across the pellet-to-cladding gap and towards the coolant, as Figure 5 shows.

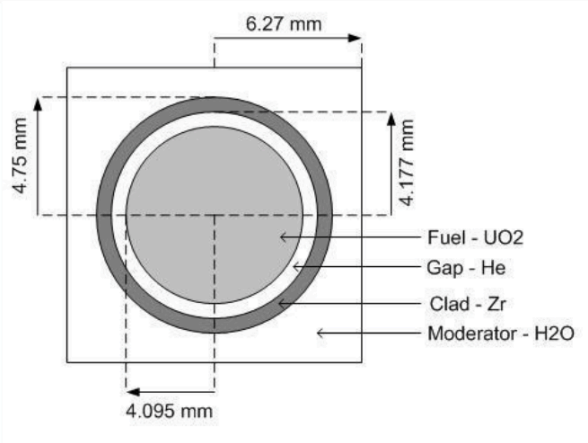

Figure 5: Cross Section of an individual Fuel Rod and the Zr Clad [3].

1.2.4 Control Rods & Reactor Control

Control Rods are perhaps the most vital part of the reactor. They are in charge of controlling and moderating the fission chain reaction. Especially during reactor startup and shutdown (where there safety role is essential). Control Rods are similar to Fuel Rods but composed by materials like boron, cadmium and hafnium, these are all good neutron absorbers (Figure 6). Therefore, when inserted, they capture neutrons throughout the Vessel and slow down the fission chain reaction. This results in a lower thermal energy emission and a lower power output of the Nuclear Plant.

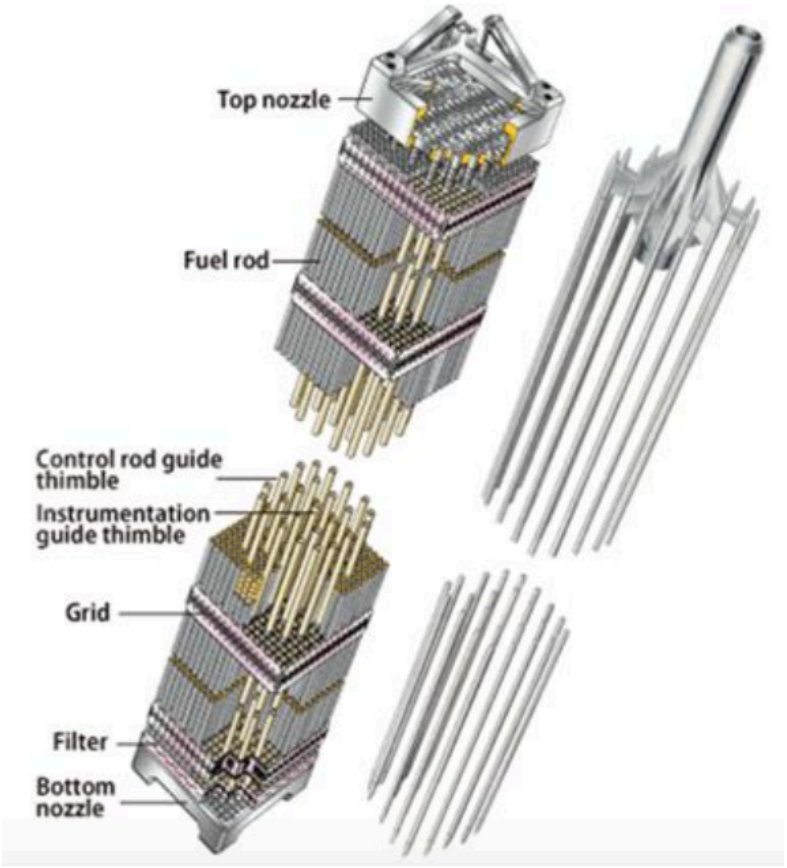

Figure 6: Fuel Assmebly and Respective Control Rod Cluster [3].

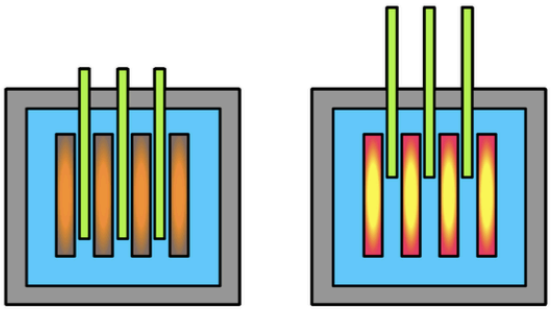

Figure 7: Control Rod States.

Figure 7 shows both states of the regulation of the power density in the core. On the left hand side the green control rods are completely inserted. The reaction is, therefore, in a subcritical state (new neutron emission is lower than old neutron absorption). On the right hand side, the control rods are completely removed from the core. This results in a supercritical state (new neutron emission due to the chain reaction is higher than old neutron absorption).

1.2.5 Spacer Grids

Spacer Grids are in charge of providing structure and mechanical support to the Fuel Assembly. They hold the 289 rods in their position and act as a kind of union. Therefore, when lateral hydraulic forces induce bowing on each individual fuel rod, the whole Fuel Assembly is displaced and bows in the same direction and with a similar shape (C or S). Spacer grids also have rather unusual shapes and blades sticking out of their structure. This intends to maximize the creation of turbulent flow in order to enhance the heat exchange along the height of the core. It is, hence, here, where very high pressure losses occur, leading to axial and lateral loads on the structure.

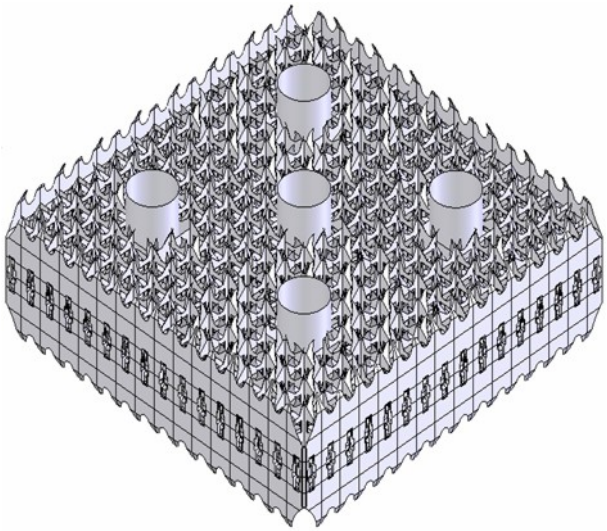

Figure 8: Spacer Grid with Control Thimbles [3].

1.3 Theoretical Framework of the Thesis

In the recent decades excessive Fuel Assembly deformation has been noticed in many PWR reactor cores. This FA deformation or bowing is mainly in C & S shapes and is an issue of considerable importance due to its impact on the Power Plant´s performance [4]. During reactor operation Fuel Assemblies are affected by several processes that are governed by a wide variety of factors.

To begin with, changing Power Density gradients cause different growth of the Zircaloy materials and different dilatation rates of fuel rods as well as different elongations due to uneven thermal expansion. The axial and lateral forces originated within the Fuel Assembly united to irradiation induced creep and hold down forces then lead to bending moments being transmitted to the structure [5].

At the same time, water moving through the core is affected by the resulting FA geometry. The velocity profile moving up the whole core is a turbulent profile, with the highest velocities occurring towards the centerline of the core vessel, as shown in Figure 9. The pressure drop within the rod bundles generates hydromechanics forces, whose pressure drop coefficient depend on the mass flow rate and on the slope of the angle between the flow and the bundle itself [6].

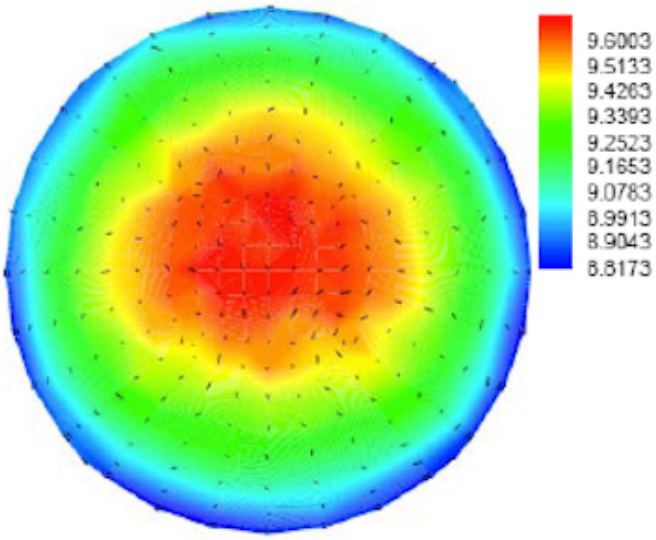

Figure 9: Cross Section of a Turbulent Velocity Profile in a Cylinder.

Occurrence of this bowing phenomenon can have a big impact on PWR operation and Power Plant performance. Bending of the FAs leads to contact between adjacent assemblies and this worsens the problem further, resulting in spacer grid wear and operational and safety issues [6].

On one hand, bowing affects the correct insertion of control rods, which is fundamental for controlling the reactor. When this occurs, both Incomplete Rod Insertion (IRI) and an increase of the time necessary to drop the control rods can be observed. If not dealt with cautiously, these IRI episodes can have a tragic effect in the case of a Scram Shut down necessity. The deformation of the Fuel Assemblies causes uneven water gaps to be formed, resulting in a perturbation of the power distribution and consequently the decrease of thermal margins and

of thermal efficiency. Finally, friction forces between assemblies complicate their extraction and reshuffling and result in higher refueling and outage times, leading to the loss of money and energy [4].

However, the variety of physical processes involved in FA bowing (structural, thermal material, hydraulic and neutronic) added to all the reactor elements being subjected to deformation make it a difficult issue to predict. In addition, the problem must be studied simultaneously on a small scale (fuel rod-to-grid connection) as well as on a larger scale (taking into account the entire core with all loads). To complicate the matter even further, the turbulent velocity profile inside the Core Vessel is not exactly known and very difficult to measure (further information in Subsection 2.1.2).

1.4 The Objective of the Bow Analysis Model

It becomes clear that FA bow is a phenomenon that has to be measured and controlled. The magnitude of these Lateral Pressure Forces and Pressure Drops must be known in the most accurate way possible, in order to efficiently prevent their negative impacts and optimize the Reactor operation [5].

As mentioned, these Lateral Pressure Drops depend strongly on local conditions and therefore make Lateral Hydraulic Forces very difficult to predict. The objectives of Bow Analysis are to implement a reliable tool that can predict FA Bow accurately, to investigate the parameters that have the strongest effect on the bowing phenomenon, and, hence, to provide assessment data for possible new FA design modifications.

To accomplish this successfully a Fluid-Structure interaction interface has to be correctly implemented, where the effects of the hydraulic loads on the structure are taken into account. The new structural characterization will in time affect the new hydraulic loads and these will, of course, influence the structure further. The quality of this coupling will determine the degree of precision of the simulation compared to real life results.

A CFD Porous Model simulation is, in the present framework, the only realistic way to approach the research challenge, as a simulation with a detailed FA geometry would be too computationally expensive. This finally derives in the need for well-defined momentum loss coefficients that replicate the real life pressure losses of the PWR geometry [7].

1.5 The Fluid-Structure Interaction Interface

The Fluid-Structure Interaction Interface composes the keystone and essential part of this Thesis. Therefore, it requires further explanation. As stated previously the quality and accuracy of the coupling will determine the precision of the bowing results with respect to authentic ones.

1.5.1 Lateral Hydraulic Forces

Subsection 1.3 states that the Lateral Hydraulic Forces are caused by the pressure drop originated in the Reactor Pressure Vessel. However, a distinction of the two pressure drops that occur has to be made: the one in the main flow direction (axial drop), and the lateral pressure drop due to radial differentials, which results in Lateral Hydraulic forces being originated. Besides the turbulent velocity profile, other mechanisms also play a significant role in these pressure drops. Following, are some of the axial losses occurring in the main flow direction.

1. Friction Pressure Drop from the Fuel Rod Bundle: channel friction originated when the coolant flows up the core and contacts the clad walls.
2. Form Losses from the Spacer Grids: Spacer Grids maintain the Fuel Assembly geometry and keep the bundles packed together. However, their presence causes an interruption of the flow and, of course, brings a form loss with it, due to the change in the flow channel.
3. Pressure Losses at the core inlet and exit flow Plenum: as in any other closed pipe, the expansion and contraction of the core plenums cause a pressure drop which is determined by the type of inlet/exit geometry.

1.5.2 Effect of Lateral Hydraulic Forces

Several papers and studies have shown that the Lateral Hydraulic forces are mostly present in the first third and the last third of the Reactor Pressure Vessel, due to the proximity to the core in- and outlets [6] [8]. Figure 10 shows this, the Lateral Velocity is particularly high close to the inlet and outlet of the Core. In these regions, the cross-flow can reach speeds in the order of 0.1 ms^{-1}, which in comparison to the axial velocity of around 7 ms^{-1}, is quite significant regarding long-term creep processes.

The result of these cross-flows is also shown in Figure 10 (provided by A. Wanninger and very representative for this Thesis´s work [9]). The figure is composed of the Fuel Assemblies 0-7 (left to right) representing one half of the central row in the core (marked yellow in Figure 3), where FA 0 would be in the centerline of the Pressure Vessel and FA 7 would be next to the Reactor wall. Meanwhile, the y-axis goes from 0-4.5 m and represents the elevation of each point within the Core. It can be observed that the linear force on the structure is greater towards the outside of the Core (FAs 5-7) and also in the lower (0-0.5 m) and upper parts (4-4.5 m) of the core, near the core outlet. The result of these higher forces acting in these locations is the C-Shaped Bow caused in many of the FAs, similar to the deformation of an inextensible beam when two shear forces are applied close to both of its ends. Figure 11 reflects the process, which is also further expanded on in J. Stabel´s work [10].

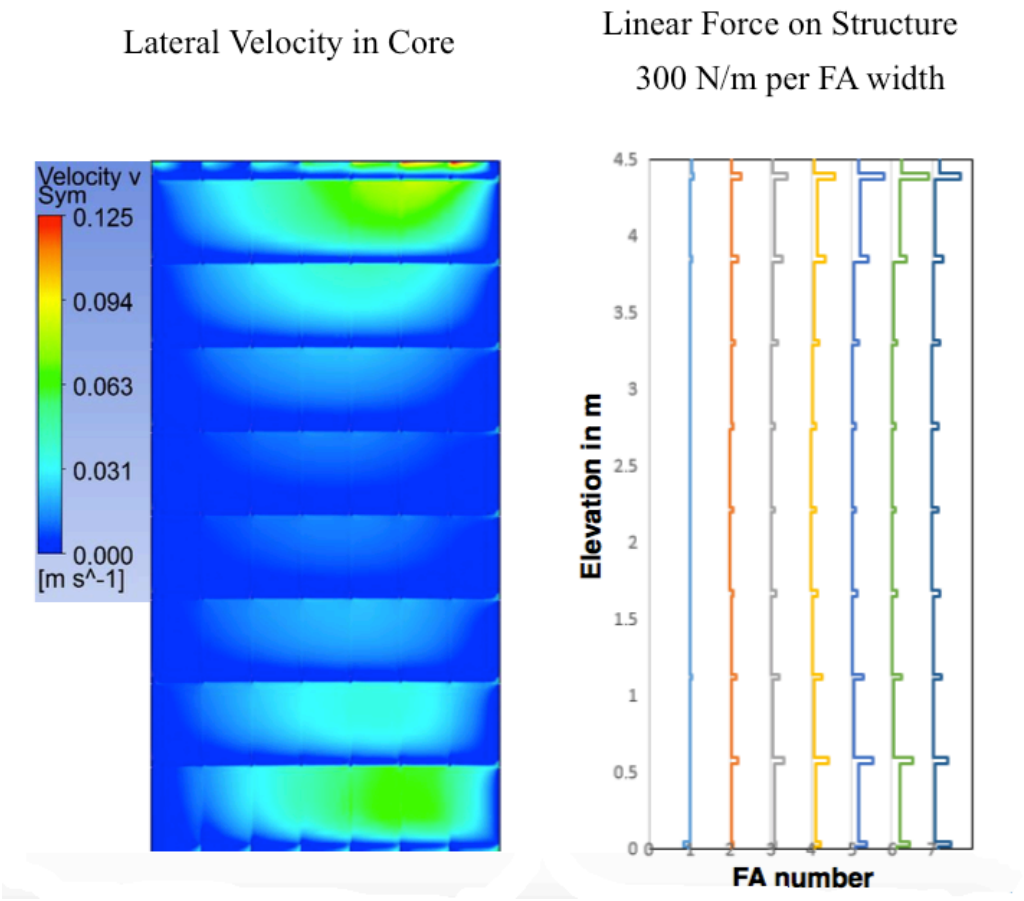

Figure 10: Lateral Velocity Distribution in the Core and Force on the Structure [9].

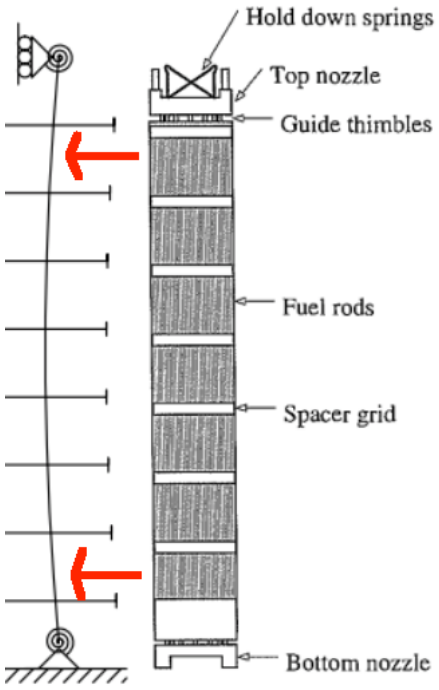

Figure 11: C-Shaped bow induced in a FA.

1.5.3 The Fluid-Structure Interface

In the recent years, the French Nuclear-Energy conglomerate AREVA has been developing a FSI Interface approach targeting FA bow prediction [11]. The objective of this FSI Interface was that of coupling a mechanical model representing the mechanical behavior of the FAs, with a hydraulic model providing the hydraulic force distribution of each FA of the core.

This Thesis aims at reproducing and presenting the different aspects and features of this professionalized FSI Interface. Due to numerical and time constraints, a complete 3D model of the whole Core is not put to use, instead a 7-row Fuel Assembly configuration is set and intends to reproduce the conditions of a real life 15 row FA array, including the initial and boundary conditions.

For the FSI simulations, the CFD code ANSYS CFX will be used for the hydraulic part and the Finite Element code ANSYS Mechanical APDL for the structural part. First of all the CFX pre-processing files will have to be adapted to the chosen structural displacement transfer files (obtained using ANSYS APDL) representing the deformed fuel assemblies. Once the pre-processing files include this new information, CFX will simulate the changed geometrical conditions in the PWR Core and obtain the new Lateral Hydraulic Force distributions. A Linux Shell Script will be used to automate the entire input (the solving and the output procedure), looping both simulation environments and their respective results. Special attention will have to be placed on fixing the most suitable time step and the load transfer. The degree of precision they attain will determine the degree of accuracy of the FA bowing and hence the quality of the FSI Interface.

2 Modeling Approach: Computational Fluid Dynamics

2.1 CFD Simulation

Computational Fluid Dynamics is a branch of Fluid Mechanics that uses numerical analysis to solve and analyze problems involving fluid flows. Computational power is used to perform the calculations required to simulate the interaction of liquids and gases with given surfaces defined by boundary conditions.

In Nuclear Energy the use of CFD is becoming vital and increasing every day. Most phenomena that have to be studied for the successful operation of Nuclear Power Plants are very costly to evaluate experimentally or simply cannot be reproduced in real life. This Thesis, therefore, works along the lines of this need and tries to make the most out of this useful tool.

2.1.1 CFD Theoretical Background

CFD is used to solve fluid governing equations such as the Navier-Stokes Equations. These types of equations are difficult to solve analytically since they are partial differential equations of higher order and require iterative solving and approximation in most cases.

CFD can be briefly explained by:

In its essence CFD is a combination of techniques that permeate the numerical resolution, both in time and in space, of the equations governing the movement of a fluid. This allows the derivation of a sufficiently accurate definition of any fluid field that presents an engineering interest [12].

The fundamental axioms of Fluid Dynamics are the conservation laws of physics that characterize any given fluid:

1. **Conservation of Mass or Continuity Equation.**

The rate of change of a fluid inside a Control Volume must be equal to the net rate of fluid entering that Control Volume. In other words, mass can neither be created nor destroyed inside the given Control Volume [13].

$$\frac{\partial}{\partial t}\iiint_V \rho\, dV = -\oiint_S \rho\mathbf{u}\cdot d\mathbf{S}$$

Equation 1: Continuity Equation. *(2-1)*

2. Conservation of Momentum.

This equation applies Newton´s Second Law of Motion to the Control Volume. Therefore, the variation of the momentum of a system must equal the sum of the resultant external forces acting on it [13].

$$\frac{\partial \rho u_j}{\partial t} + \frac{\partial \rho u_i u_j}{\partial x_i} = \frac{\partial \sigma_{ij}}{\partial x_i} + \rho B_j + S_{M,j} \qquad j = 1,\ldots 3$$

Equation 2: Conservation of Momentum. *(2-2)*

3. Conservation of Energy.

Energy is neither created nor destroyed, just transformed from one form to another. Hence, the total energy in a closed system remains constant [13]. The Equation of Conservation of Energy is particularly important in fluxes with heat exchange and with significant density variations (compressible fluids). As this Thesis is going to focus on the Hydraulic-Structure Interaction under isothermal conditions, there is no need to further expand.

$$\rho \frac{Dh}{Dt} = \frac{Dp}{Dt} + \nabla \cdot (k \nabla T) + \Phi$$

Equation 3: Conservation of Energy. *(2-3)*

2.1.2 The Closure Problem and its relation to this Work [12]

One of the main research fields in modern Fluid Dynamics is the Closure Problem. The Navier-Stokes Equations govern the velocity and the pressure of a fluid flow. As it has already been mentioned, the flow up the Core Vessel is turbulent flow, in order to maximize the heat exchange throughout the Core length.

Traditionally, when studying the Fluid Dynamics of a given flow there are seven unknowns:

- Mechanical unknowns:
  1. The Components of Velocity in X, Y & Z (+3).
  2. The Pressure (+1).
  3. The Density (+1).

- Thermodynamic unknowns:
  1. Temperature (+1).
  2. Internal Energy U (+1).

= 7

However, by using the Conservation Laws accompanied by the Equations of State the Seven unknowns can be solved. As there is a tie: 7 unknowns and 7 variable solutions for the system (7 = 7).

- Conservation Laws:
  4. Balance of Forces in X, Y & Z (+3).
  5. Conservation of Mass (+1).
  6. Conservation of Energy (+1).

- Equations of State:
  3. Density Tables: ρ [P, T] (+1).
  4. Internal Energy: U [P, T] (+1).

= 7

The instability comes when considering turbulent flow. In the turbulent flow occurring in the Reactor Vessel, the velocity is decomposed into a mean part and a fluctuating part. The pulsatile component of each individual fluid particle has to be considered and, therefore, besides the three given components of velocity in X, Y & Z, each particle vibrates upon its position in the X, Y or Z direction also. Figure 12 shows this pulsatile component Reference System in blue.

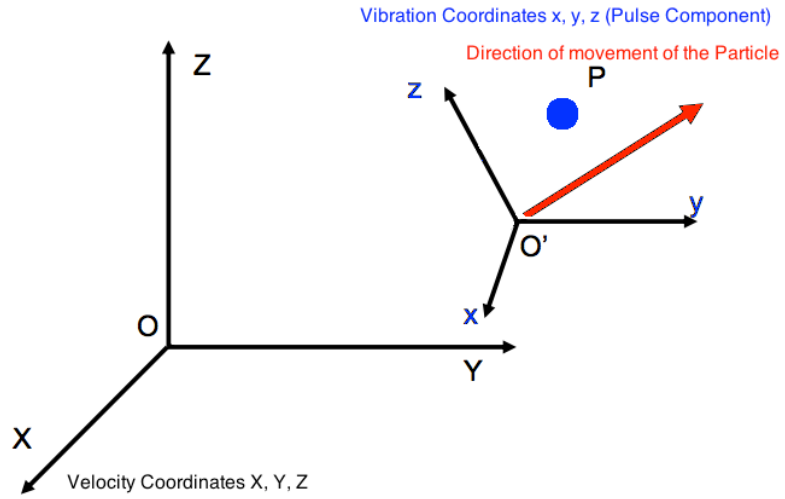

Figure 12: Reference Systems for Velocity and Vibration in Turbulent Flow.

When turbulence is studied there is, hence, no longer a tie. The three pulse components of X, Y, Z are accounted for and there are now 10 unknowns (10 ≠ 7). In this Thesis, however, the studied fluid (H2O) is an incompressible fluid and therefore its mechanical and thermodynamic properties are not interdependent. This, united to the respective Reynolds-Averaged Navier-Stokes (RANS) equations, permeates a possible solution and the determination of the magnitudes of the Lateral Hydraulic Forces acting on the Fuel Assembly. The chosen CFD software to encounter these solutions is ANSYS CFX, explained in Subsection 2.2.

2.2 ANSYS CFX

ANSYS CFX Software is a high-performance Fluid Dynamics program that can be applied to solve wide-ranging fluid flow problems. It allows the user to predict, reliably, the impact of the fluid flows on the object of study during both operation and also at end use.

It is divided into the following four modules:

1. ANSYS CFX PRE

The available preprocessing tool CFX Pre is used to define and specify the simulation settings and physical parameters required to describe the flow problem precisely. Some of the necessary tasks include: mesh import, material specification, setting boundary conditions and defining the simulation type (steady state or transient). It is also necessary to define the domain.

2. ANSYS CFX SOLVER

ANSYS CFX Solver is one of the most powerful Fluid Dynamics problem resolution interfaces. It solves the equations and parameters given by CFX Pre by taking into account the set-up conditions and allows a continual monitoring of the calculation process.

3. ANSYS CFX POST

CFX Post is a graphical post-processing tool used for interactive visualization. It presents the outcome of the CFX Solver results by providing user-defined graphical representation of data.

4. ANSYS ICEM CFD

The specified geometry can be parametrically created by ICEM to use during the CFX Pre, CFX Solver and CFX Post. In this Thesis, Andreas Wanninger´s PHD Mesh Setup Model, created using ANSYS ICEM, was used [9].

Figure 13: ANSYS CFX CFD Simulation Flow.

2.3 The Porous Model

2.3.1 The necessity for a Porous Model

A porous material is a medium of interconnected pores held together by a solid structure or skeleton. The peculiarity a porous medium has is that a flow of fluid can travel through these pores efficiently. The resistance the fluid will find during its motion can be predetermined by the porosity of the material. Porosity is defined as the fraction out of the total or percentage of the medium that is solid skeleton. That is to say a material with a porosity of 70% will allow fluid to move across a 70% of its cross-section area, and only 30% will be sturdy solid.

Ideally, the CFD Simulation of this Thesis would be carried out by constructing an exact representation of the PWR Reactor Core. This exact replica would then be used for the dynamic simulation. However, the construction of an accurate PWR FA mesh like the one in Figure 14 over the entire core is, by far, too computationally expensive to result feasible and, because of this, the CFD Simulation would not be possible.

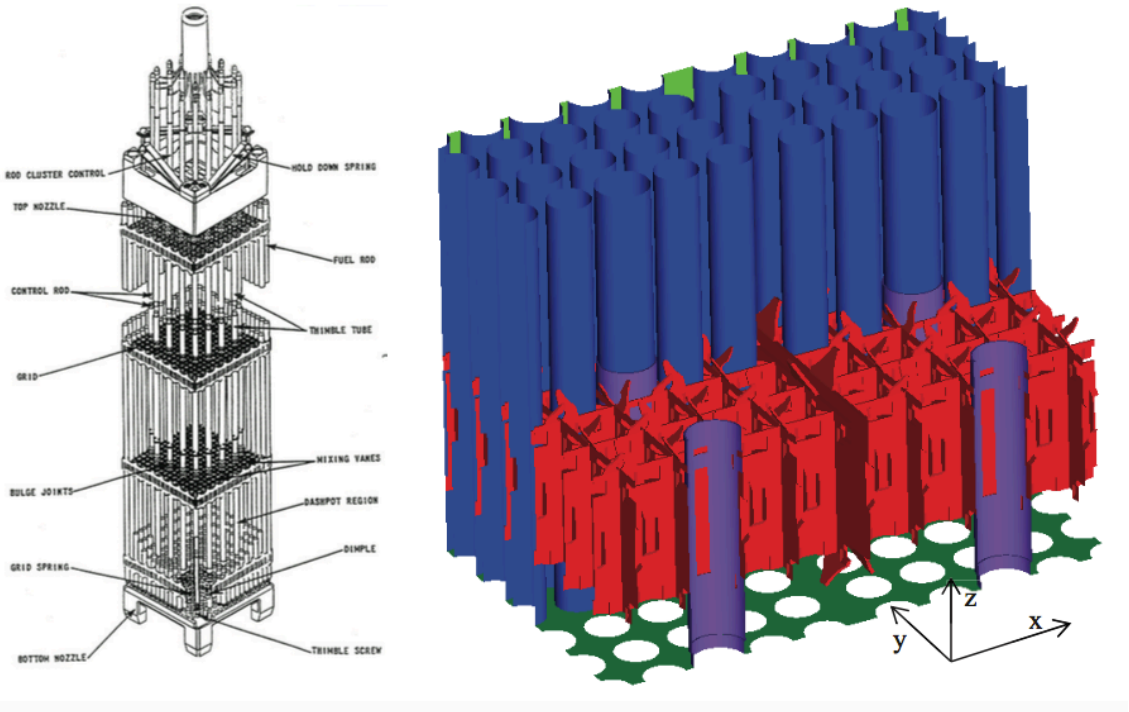

Figure 14: CAD Model of the geometry of a typical Fuel Assembly [8].

As a reliable and solid approximation, the pressure drop of any flow traveling through a given structure can be modeled by a porous medium such as the one mentioned above. The resistance to flow of the porous medium will be accounted for by establishing appropriate Loss Coefficients. This will accurately simulate the pressure drops that would occur in Real Life or in a Real Life geometry simulated model (See Subsection 3.2).

2.3.2 Modeling the Porous Model in ANSYS CFX

Before going on to displaying the actual simulation model of the PWR Core Vessel in Chapter 3, it is necessary to explain some basic concepts of how ANSYS CFX works and how the intended Loss Coefficients can be modeled [7].

Momentum Sources in ANSYS CFX

Momentum sources are mainly used to model the directional or isotropic losses in the porous regions of the medium. CFX distinguishes three types of momentum sources:

1. Directional Losses

The stream-wise direction must be specified, considering a stream-wise-oriented coordinates system (x´, y´& z´). KpermS & KpermT are the stream-wise and transverse permeabilities of the medium, and KlossS & KlossT are the equivalent quadratic loss coefficients.

$$S_{M,x'} = -\frac{\mu}{K^S_{\text{perm}}} U_{x'} - K^S_{\text{loss}} \frac{\rho}{2} |\boldsymbol{U}| U_{x'}$$
$$S_{M,y'} = -\frac{\mu}{K^T_{\text{perm}}} U_{y'} - K^T_{\text{loss}} \frac{\rho}{2} |\boldsymbol{U}| U_{y'}$$
$$S_{M,z'} = -\frac{\mu}{K^T_{\text{perm}}} U_{z'} - K^T_{\text{loss}} \frac{\rho}{2} |\boldsymbol{U}| U_{z'}$$

Equation 4: Directional Momentum Losses. *(2-4)*

2. Isotropic Losses

Like in the Directional Losses, Kperm & Kloss are the permeability and loss coefficients. The linear term (Kperm) represents the viscous losses, and the quadratic term (Kloss) the inertial losses.

$$S_{M,x} = -\frac{\mu}{K_{\text{perm}}} U_x - K_{\text{loss}} \frac{\rho}{2} |\boldsymbol{U}| U_x$$
$$S_{M,y} = -\frac{\mu}{K_{\text{perm}}} U_y - K_{\text{loss}} \frac{\rho}{2} |\boldsymbol{U}| U_y$$
$$S_{M,z} = -\frac{\mu}{K_{\text{perm}}} U_z - K_{\text{loss}} \frac{\rho}{2} |\boldsymbol{U}| U_z$$

Equation 5: Isotropic Momentum Losses. *(2-5)*

In the case of this Thesis´s model, the viscous losses will be neglected, since the pressure drop due to turbulent flow in the reactor can be obtained from these flow resistance coefficients multiplied by a dynamic pressure term. Unlike in a classical porous medium with interconnected pores, only the quadratic term resides.

True and Superficial Velocity

When working in a porous medium one last distinction has to be made, the difference between True Velocity and Superficial Velocity. True Velocity is the actual physical velocity inside the domain. In a porous model with the True Velocity formulation, the porosity modifies all the velocity terms of the governing equations. Meanwhile, in the Superficial Velocity formulation as used in this Thesis, porosity does not affect these equation terms [14]. Superficial Velocity is a hypothetical (artificial) flow velocity calculated by disregarding the skeleton or the porous medium present in the channel. It is the value that is readily known and unambiguous, and it is not variable from point to point within the domain.

$$v_{superficial} = \frac{Q_{Volume\ flow\ rate\ (m^3 s^{-1})}}{A_{Cross\ Sectional\ area\ (m^2)}}$$

Equation 6: Superficial Velocity. *(2-6)*

The relation between True Velocity and Superficial Velocity can be drawn by the porosity γ:

$$v_{true} = \frac{v_{superficial}}{\gamma}$$

Equation 7: True and Superficial Velocity. *(2-7)*

3 Simulation Setup

3.1 Model & Geometrical Dimensions

3.1.1 Geometrical Dimensions

The geometrical model and the mesh of the Fuel Assembly used in this Thesis was provided by A. Wanninger [9]. The model is composed of two types of subdomains: the ones representing the Spacer Grid region of the PWR, and the ones representing the Rod region. Each Fuel Assembly is 4.5 m high and contains 9 Spacer Grid regions and 10 Fuel Rod subdomains, as Figure 15 shows. The used mesh includes the geometrical gaps between the FAs into the adjacent rod and grid region instead of modeling them as separate regions. Their effect will be simulated by step functions of the Pressure Loss Coefficients later on.

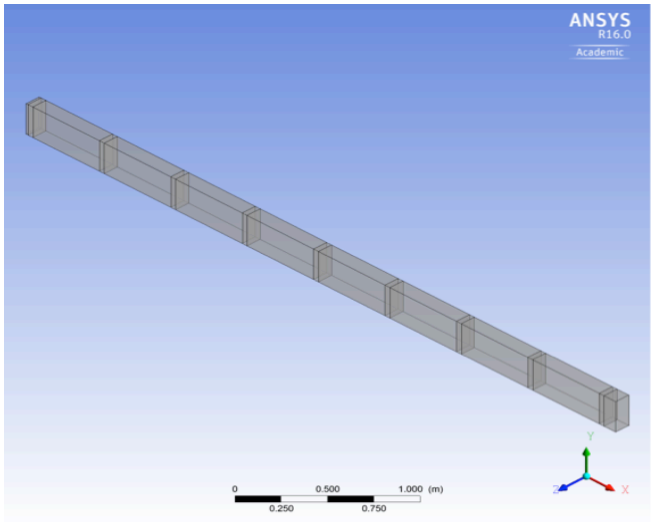

Figure 15: FA Mesh – File "Single FA_DetailParts3.cfx5".

Table 1 includes the dimensions of 1 FA. The real depth of the FA geometry would also be 0.23 m (it is a square array in real life). However, by establishing a cell depth of 1 in the Z direction, 2D conditions are simulated.

Element	Height X direction	Width Y direction	Depth Z direction
Fuel Assembly	4.5 m	0.23 m	0.1 m
Rods	0.508 m	0.23 m	0.1 m
Spacer Grids	0.05 m	0.23 m	0.1 m

Table 1: Dimensions of the FA.

Simulating the behavior of the entire core is computationally too expensive, this Thesis, therefore, simulates a complete row of 15 FA and considers it as representative of the whole Core. The file "*MeshSetupWoGaps.pre*" [9] generates the 15 Fuel Assemblies that occupy the row in the core marked in yellow in Figure 3. Figure 16 shows half of the row (the initial 7 Fuel Assemblies), while Figure 22 shows the entire central row of the Core.

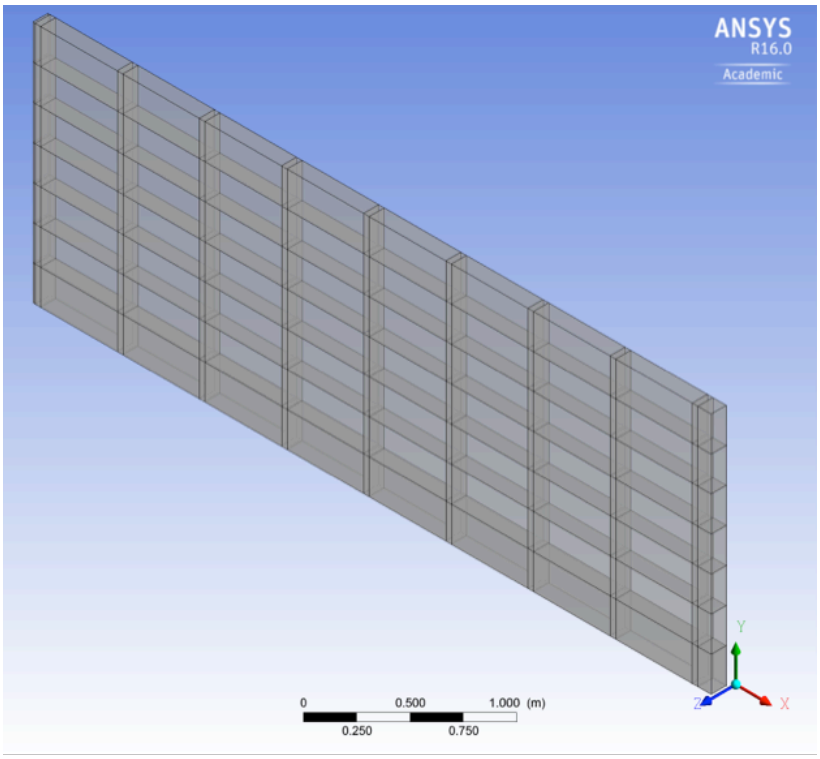

Figure 16: 7 FAs with the symmetry line in the plane Y=0.

The next step is to define the mathematical expressions needed for the simulation. The CFX Command Language File (CCL File) "*ExpressionsFluid.ccl*" was used and imported to CFX, it includes all the physical and mathematical expressions that would be needed later on.

3.1.2 Boundary Conditions

The model also requires the definition of the boundary conditions, which aim at reproducing the conditions in a real life operational PWR. They all refer to Figure 17.

1. Inlet

The inlet is where the coolant flow enters the domain (signaled by incoming black arrows). It is the bottom of the FAs and it is contained in the YZ plane (coordinate of X = 0m). The superficial inlet velocity for the porous medium is around 3.5 ms^{-1}.

2. Outlet

The outlet is where the flow exits the domain (signaled by outgoing black arrows). It represents the top of the FAs where the flow would then move on to the upper plenum and Steam Generator. It is also contained in the YZ Plane (X coordinate of 4.5 m).

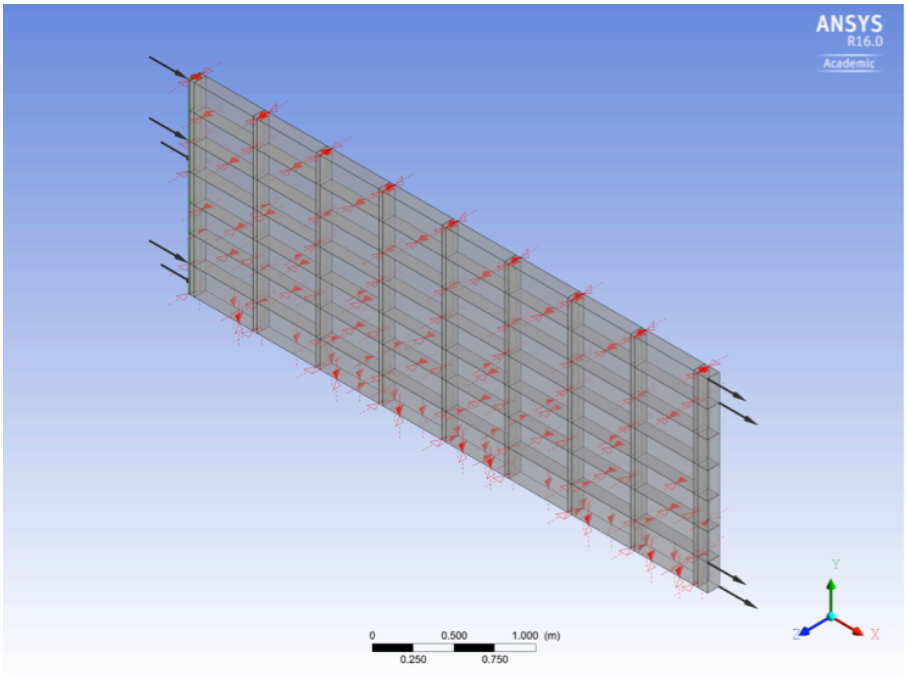

Figure 17: Boundary Conditions of the FA.

3. The exterior wall

The exterior wall represents the ends of the FA row, which would be in contact with the real reactor wall. The contact surface is in the XZ Plane (Y coordinate = $\pm$ 1.61 m). It is the outer lateral wall of the 1st and 15th Fuel Assembly and it is set as smooth non-slip surface condition in CFX.

4. Symmetry Planes

They are the front and back planes in the form of red arrows, they are necessary because flow is considered as two-dimensional and the mesh is one cell deep.

3.1.3 Thermodynamic Conditions

The model was set to isothermal conditions in CFX Pre, its mean temperature being 300 ºC and the reference pressure 15.8 MPa (similar to a real life PWR). Finally, the turbulence of the coolant water was resolved using the k – ε model.

3.2 Accounting for the Pressure Losses

As explained in Subsection 2.3.1, using a Porous Model offers the advantage of lower computational expense and higher computational efficiency. Nevertheless, for the simulation to be carried out correctly, the pressure drops that would occur in real life have to be accounted for by rigorous Loss Coefficients characterizing the porous medium.

The reviewed literature emphasizes on the importance of these pressure drops as the main drivers of FA Bow [7] [8] [9]. One of the main reference articles in the field, written by J. Peybernès, focuses on the pressure drops derived from a variety of Reynolds Numbers and from changing slope angles (30º - 90º) between the fuel bundles and the flow. The article determines the Pressure Drop Coefficients with Equation 8, where P1r is the pressure drop in FA number 1.

$$K = \frac{\Delta P1r}{\frac{1}{2}\rho V^2}$$

Equation 8: Pressure Drop Coefficient in a PWR. (3-1)

Applying these theoretical concepts to this Thesis´s simulation model, four main Loss Coefficients have to be evaluated [9]:

- Pressure loss coefficient in the Rods in axial direction $K_{loss\ rods\ axial\ flow}$.
- Pressure loss coefficient in the Rods in transversal direction $K_{loss\ rods\ crossflow}$.
- Pressure loss coefficient in the Grids in axial direction $K_{loss\ \ grid\ axial\ flow}$.
- Pressure loss coefficient in the Grids in transversal direction $K_{loss\ \ grid\ crossflow}$.

There is also a fifth pressure loss that should be accounted for, the Grid Bypass. This pressure loss is originated by the gaps existing between the Fuel Assemblies of the PWR. In this framework it is neglected, as its magnitude is very small compared to the other four.

Before going on to explain each of these four pressure losses, some of the fixed parameters that characterize the PWR Core and that will be used in the following subsection are listed in Table 2.

Parameters	Description	Symbol	Formula / Value
Pitch	Distance between FR.	p	0.0143 m
Diameter FR	FR outer diameter.	d	0.01075 m
Perimeter FR	FR perimeter.	Pfr	$d\,\pi$

Area FR pitch	Area between FR.	$Afree$	p^2
Area Subch.	Area of the Sub-channel available for flow.	$Asubch.$	$p^2 - \frac{d^2\pi}{4}$
Porosity	Flow to material ratio.	γ	$\frac{Asubch.}{Afree}$
Hydraulic Diameter	Hydraulic Diameter of the Rod Bundle based on $Asubch.$	Dh	$\frac{4\ Asubch.}{Pfr}$
Angle of Attack	Angle of coolant impact on the FR.	θ	$\arcsin\ (\frac{Uy}{u})$

Table 2: PWR Parameters.

3.2.1 Pressure Loss of the Rods in the axial direction

Like in any confined cylinder with a fluid flowing through it, friction of the coolant with the rod bundle walls causes a considerable pressure loss. This pressure loss is expressed as a function of several factors.

$$\Delta p_{friction} = f\frac{L}{D_h}\frac{\rho v_{true}^2}{2}$$

Equation 9: Axial Pressure Loss in Rods [3]. *(3-2)*

- L = Channel Length.
- D_h = Hydraulic Diameter.
- f = Average Friction Factor.
- v_{true} = True velocity, velocity of the fluid.

The friction factor for axial flow is obtained as a function of the Reynolds number with the McAdams equation, assuming Turbulent flow inside the Core (Re > 10000).

$$f_{McAdams} = 0{,}184\ Re_{Axial}^{-0,2}$$

Equation 10: McAdams Equation [9]. *(3-3)*

The velocity term is also affected due to the fact that the simulation of the FA is carried out in a Porous model with the superficial velocity formulation. As explained in Subsection 2.3.2, true velocity results by dividing the superficial velocity by the porous factor: $Vtrue = \frac{Vsuperficial}{\gamma}$.

Finally the drop coefficient is determined:

$$K_{loss\ rods\ axial\ flow} = \frac{f_{McAdams}}{D_h\ \gamma^2}$$

Equation 11: Axial Loss Coefficient in Rods. *(3-4)*

3.2.2 Pressure Loss of the Rods in the transversal direction

The review of J. Peybernès´s work in the field of Lateral Hydraulic Forces represented the keystone upon which this Thesis based its FSI Interface [7]. The EOLE Tests [15], by studying different Turbulent flows and by changing angle inclinations between the flow and the Rod bundles, enabled the establishment of an empirical correlation. This correlation relates the pressure drop coefficient per rod row as a function of the slope angle θ, and the friction factor for cross-flow ($f_{crossflow}$).

$$K_{loss\ rods\ crossflow}(\theta) = \xi(\theta) * f_{crossflow}$$

Equation 12: Transversal Loss Coefficient in Rods. *(3-5)*

The friction factor for the cross-flow can be determined as:

$$f_{crossflow} = a\ Re^b$$

with a = 1.85 and b = -2 in the case of pure transversal cross-flow ($\theta = 90$). Meanwhile, $\xi(\theta)$ is the Peybernès correction factor, which changes value depending on the angle of attack of the fluid on the rods. $\xi(\theta) = 0$ in the case of pure axial flow ($\theta = 0º$), and $\xi(\theta) = 1$ in the case of pure transversal flow ($\theta = 90º$). The correction factor can be evaluated as:

$$\xi(\theta) = \frac{sin(\theta)}{cos(\frac{90-\theta}{2})}^{1.7}$$

Equation 13: The Peybernès Correction Factor. *(3-6)*

Equation 13 shows that the Angle of Attack is of uttermost importance in the determination of the magnitudes of the Lateral Hydraulic Forces and, therefore, vital for this Thesis. In actual fact, when FA bow occurs, the Angle of Attack varies. This can lead to the increase of the slope angle and, hence, the increase of pressure drops; resulting in higher Lateral Hydraulic Forces (see subsection 5.2). In Figure 18 the composition of the Angle of Attack can be seen, it is composed by the sum of the Structural Rotation ($\theta´$) and the angle that had previously existed between the Local flow direction and the non-deformed FA (θf).

$$\theta = \theta´ + \theta f$$

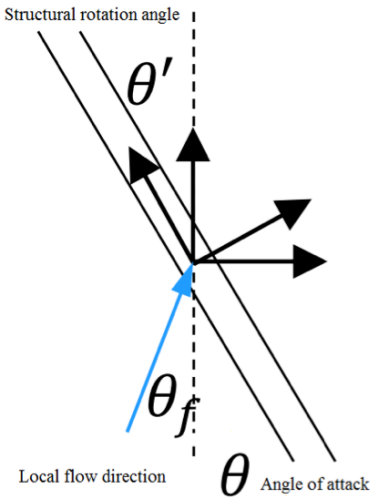

Figure 18:Composition of the Angle of Attack.

3.2.3 Pressure Loss of the Grids in the axial direction

The pressure losses that occur in the Spacer Grids are classified as form losses instead of friction losses. They are caused by the abrupt change of geometry within the FA sub-channels that the Spacer Grids originate. This geometry is deliberately designed to disturb the flow and make it more turbulent in order to enhance heat exchange.

$$\Delta p_{form} = \Delta p_{grids} + \Delta p_{inlet/outlet} = \sum_{i=1,\dots,loss} K_i \rho \frac{u_z^2}{2}$$

Equation 14: Pressure Form Losses. *(3-7)*

There can be several types of form loss factors (ki) depending on the change of geometry caused in coolant channel. Each Spacer Grid has a given form loss factor (ki) that has to be experimentally determined [3].

Using these ki´s and setting As as the area occupied by the Spacer Grid and Av as the total area occupied by the Rod Bundles:

$$\Delta p_{grids\ axial} = K_{loss\ \ grid\ axial} \frac{\rho V_{sup}^2}{2} \frac{A_s}{A_v}$$

Equation 15: Axial Pressure Loss in the Spacer Grids. *(3-8)*

Finally, the Loss Coefficient in the axial direction is evaluated by [16]:

$$K_{loss\ \ grid\ axial} = \frac{K_{form\ grid} + K_{friction\ grid} + K_{rod\ friction}}{Grid\ Height}$$

Equation 16: Axial Loss Coefficient in Spacer Grids. *(3-9)*

It can be noticed that even the Spacer Grid Loss Coefficient includes a term accounting for Rod friction within the Spacer Grid region.

3.2.4 Pressure Loss of the Grids in the transversal direction

According to the research and work of A. Wanninger [9], Lateral Hydraulic Forces on the grids are a reaction to the change in the coolant´s inertial force. That is to say, when the coolant fluid (with a certain angle of attack θ) flows into the Spacer Grid, it is redirected into a straight flow with only an axial component. The transversal component of velocity of the coolant impinges laterally on the Spacer Grid structure. This implies that the momentum loss in the transversal direction has to be equal to the Spacer Grids structural reaction.

$$Lateral\ Hydraulic\ Forces = F_{\perp} = -mv_{\perp}$$

The momentum loss in this transversal direction can be quantified as:

$$\mathrm{S_{M,\perp}} = \mathrm{F_{\perp} m v_{\perp}} = -\frac{\rho |v| v_{\perp}}{\mathrm{lgrid}}$$

While the Spacer Grid´s structural reaction remains:

$$\mathrm{S_{M,x}} = \frac{\partial \mathrm{p}}{\partial \mathrm{x}} = \frac{\rho |v| v_{\perp}}{\mathrm{lgrid}} = \mathrm{K_{loss\ grid\ axial}} \frac{\rho \mathrm{V_{sup}^2}}{2}$$

This results in:

$$K_{loss\ \ grid\ crossflow} = \frac{2}{l_{grid}}$$

Equation 17: Transversal Loss Coefficient in Spacer Grids. *(3-10)*

3.3 One-way & Two-way Coupling Methods

In physics, the interaction between fluid and structure occurs in a wide range of engineering-based problems and applications. The solutions for such problems are based on the relations of continuum mechanics and are mostly solved by using numerical methods, such as the ones used in this Thesis (CFD-CFX). As mentioned before, it is a computational challenge to solve these problems. Not only because of complex geometries, but other factors such as the intricate physics of the given fluid and complex interactions also have to be taken into account. The way in which this interaction is described gives the largest opportunity for reducing the computational effort. This Subsection is going to briefly explain the two existing approaches to describe a FSI and the one this Thesis aimed at using.

FSIs are classified as a type of multi-physics problems, characterized by the fact that the flow around a body has a strong impact on the structure, and vice-versa; the modification of the structure also has a non-negligible influence on the flow. Following this analysis, FSI is well defined by [17]:

“Coupled systems and formulations are those applicable to multiple domains and dependent variables which usually describe different physical phenomena and in which none of the domains can be solved while separated from the others, and no set of dependent variables can be explicitly eliminated at the differential equation level”.

Solution strategies for FSI simulations are mainly divided into monolithic and partitioned methods. Within partitioned methods, one-way and two-way coupling can be found. This thesis will briefly explain both and go on to explain why a one-way coupling was decided as the most suitable strategy.

For the solving of FSI problems based on partitioned methods, different physical fields are prepared. One of the fields that has to be solved is fluid dynamics, while the other is structure dynamics. At the boundary between fluids and solids lies the FSI interface, where information for the solution is shared between the fluid solver and the structure solver. The information exchanged is dependent on the coupling method and it is here where the crucial difference exists. On one hand, for one-way coupling calculations, only the fluid pressure acting at the structure is transferred to the structure solver (the hydraulics loads). On the other hand, for two-way coupling calculations the displacement of the structure on the fluid boundary is also transferred to the fluid solver *within* every single time step.

Figure 19 shows how the one-way coupling operates. Initially, the fluid field is solved until convergence criteria are reached (CFX Solver will be in charge of reaching convergence). Then, the calculated forces at the structure boundaries are transferred to the structure side. Following this, the structural side is calculated until convergence criteria are reached once again (APDL Mechanical will attain this). Finally, the fluid flow for the next time step is calculated, the solution is finished when the maximum number of time steps is reached. It is important to appreciate the fact that a one-way coupling requires convergence criteria on the hydraulic side due to changing conditions in the fluid field that are *independent* from the structural variations (other settings are responsible for the changing conditions in the fluid and not the structural deformation itself).

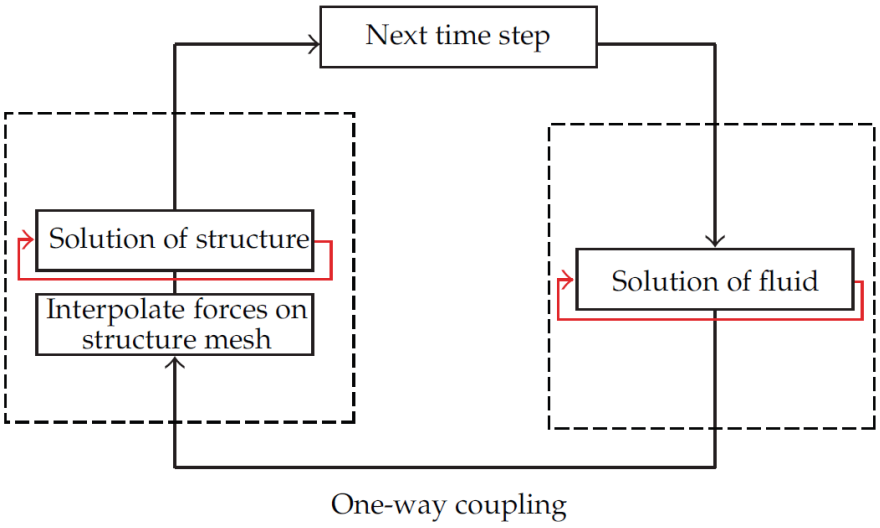

Figure 19: One-way FSI Interface Coupling.

Meanwhile, the operation of the strong two-way coupling is more complex. Within one time step during transient simulation, a fully converged solution for the flow field is required to provide the forces acting on the body. After interpolating the forces from the fluid domain to the surface mesh of the structure, a converged solution of the structural dynamics will be attained under the effect of the acting forces. However, the response of the structure to the emerging load represents a displacement of the structural grid nodes. These displacements are

interpolated to the fluid mesh again, which leads to its deformation. This step closes one inner loop of the simulation and these inner loops will be run until the variations in the flow force and structural displacements fall below a pre-set amount. Afterwards, a new time step is launched, as Figure 20 shows.

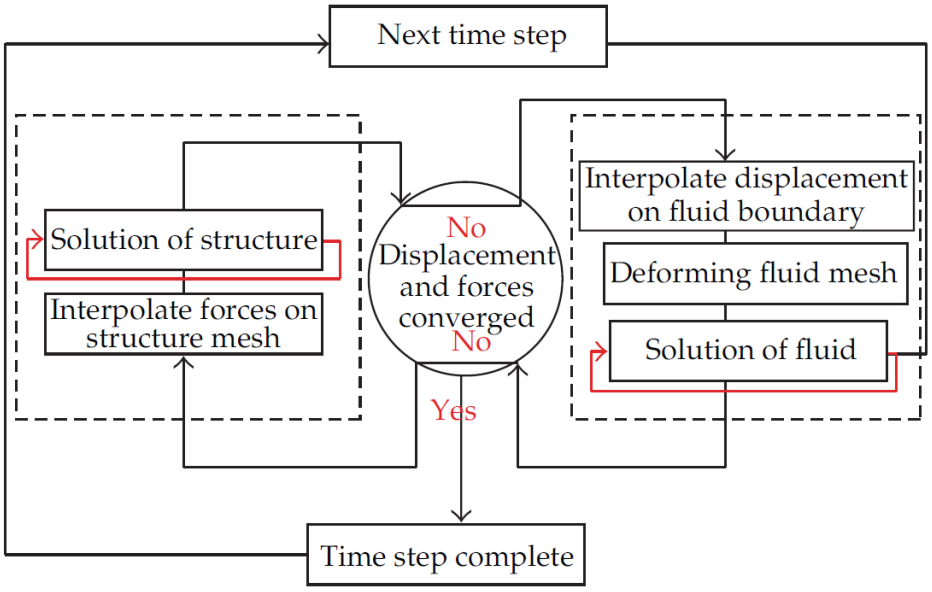

Figure 20: Strong Two-way FSI Interface Coupling.

The upside one method offers is usually the downside the other has. On one hand, the two-way coupling solution is more accurate and represents real life conditions in a more rigorous way (especially for larger deflections with a considerable influence of the structure on the fluid field). It will also guarantee energy conservation at the FSI interface and is, hence, more stable. On the other hand, one-way coupling simulation requires significantly lower computational time. A second benefit is that deformation of the fluid mesh does not need to be calculated, a mesh of constant quality can therefore be used.

The FSI coupling this Thesis aimed for lay half way in between the two. It was not a one-way coupling due to the fact that the variations in the fluid field were *dependent* of the structural variations. In actual fact, an objective of the work was to see how the structural displacements actually influenced the hydraulic behavior of the reactor. Therefore, the FSI coupling interpolated the displacement of the structure on the fluid boundary (in a pure one-way coupling this would not occur). However, the coupling could not be considered a strong two-way coupling either. The computational cost of reaching convergence of both displacements and forces within every time step (what characterizes a strong two-way coupling), was too high for the reach of this work.

It became clear that the best definition was that of a *weak* two-way coupling: one where the fluid solution was dependent of the displacement interpolation, but where inner time-step convergence was not required. Figure 21 represents this Thesis´s coupling.

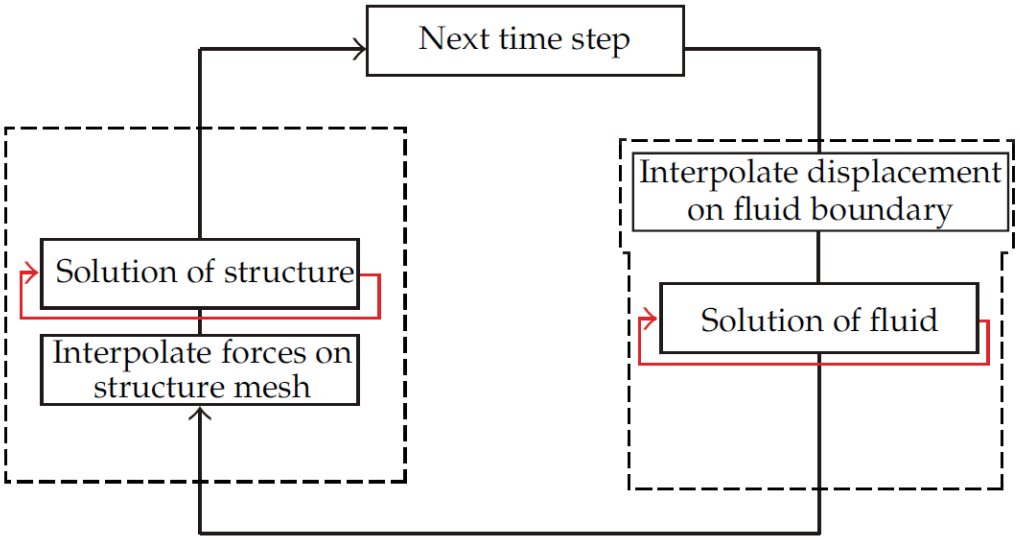

Figure 21: Weak Two-way FSI Interface Coupling.

4 Model Implementation

The Computational Fluid Dynamics modeling approach explained in Chapter 2 selects ANSYS CFX as a suitable program with which to carry out the PWR porous medium simulation. Furthermore, in Chapter 3, the initial details and characteristics of the simulation are set. Matters such as the geometrical dimensions of the model, its boundary conditions or the equivalency between the Loss Coefficients and the pressure losses are dealt with. In this Chapter, the next step will be taken. Initially the transfer of the structural data into the CFX model will be implemented. This will be followed by the development of a Linux environment Shell script able to control and automate the simultaneous transfer of hydraulic loads and structural displacements. A correct implementation of this Shell script, will lead to the consolidation of the Fluid-Structure Interaction Interface and enable the critical analysis of the obtained results.

4.1 Structural Displacement Transfer Strategy

Once the CFD model had been established and characterized in ANSYS CFX, the first step towards the FSI Interface coupling was the adaptation of the preprocessing file "*PreInputFile.ccl*", to the displacement transfer strategy. This Thesis used structural displacement data of the Core Fuel Assemblies coming from the Finite Element Method that was solved by ASNYS Mechanical APDL. A total of three displacement data files were used: "*displacementsy.csv*", "*gaps.csv*", "*rotz.csv*", with the respective displacements, gaps sizes and rotations of the 15 FAs at the grid levels.

The mesh setup was executed through the file "*MeshSetupWoGaps.pre*", provided by [9], to represent the meshing and geometry of the FAs in the graphical interface of ANSYS CFX. However, some adaptations were necessary, such as the extension from 7 FAs to 15 (in order to simulate a whole row of the Core) or the relocation of the coordinate positions of these FAs.

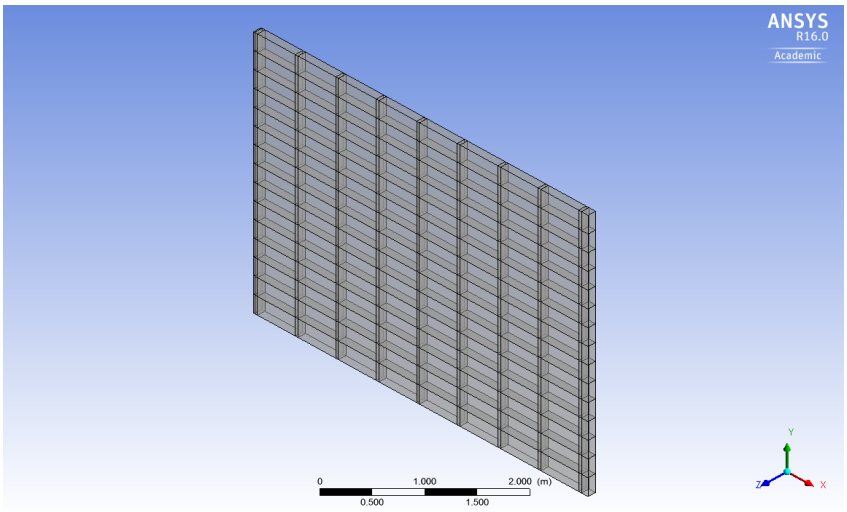

Figure 22: Initial Mesh extended to 15 FAs (Equivalent to 1 Full Core Row).

The model setup was done with a CFX Command Language File controlled by a Perl script.

4.1.1 Implementing the Displacement of the Rods

To begin with, the FA Rod deformation was characterized. The model used divided each FA into 9 Spacer Grids and 10 Rod sections, resulting in a total of 11 displacements in the "*displacementsy.csv*". The most accurate way to describe Rod deformation was by calculating an interpolation line between each Spacer Grid and the next (using the two respective displacements in the Y Plane). This was done by the Similar Triangle method, which enabled the plotting of a linear interpolated equation.

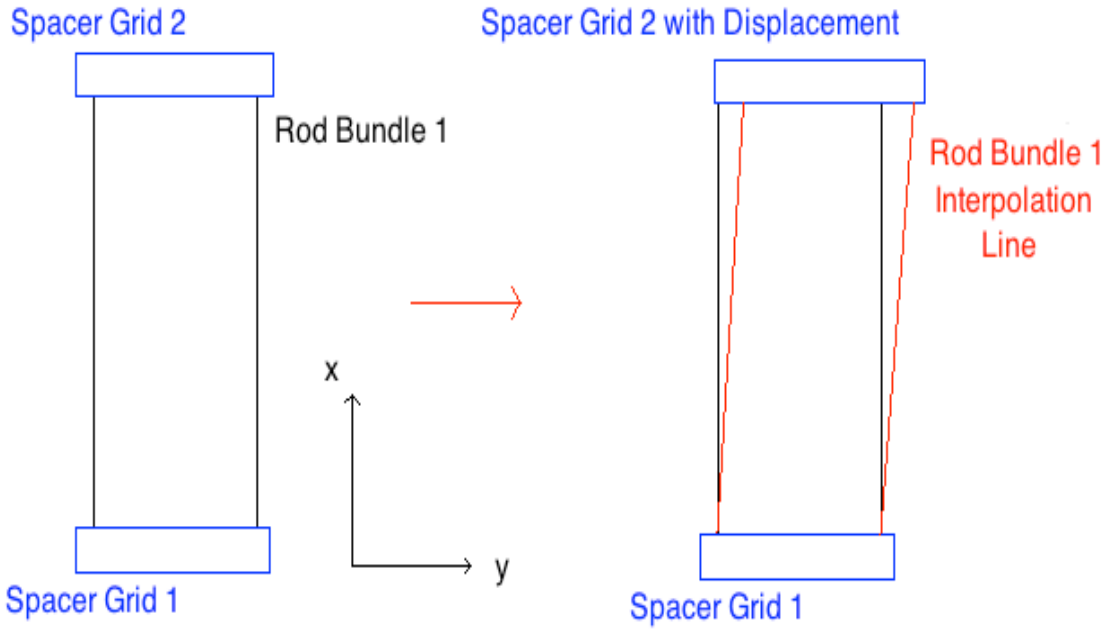

Figure 23: Interpolation Line of the Displacement of the Rods.

As Figure 23 shows, each Rod section could be re-plotted as a linear interpolated equation between two points: the point in the Spacer Grid (SG) underneath it (from where it starts, in this case SG 1 which has displacement 0) and the point in the SG above it (where it ends, in this case SG 2 which has a given displacement).

To calculate and introduce this interpolation equation in the preprocessing file, the Similar Triangles method was used. Figure 24 shows the two similar triangles in red and green.

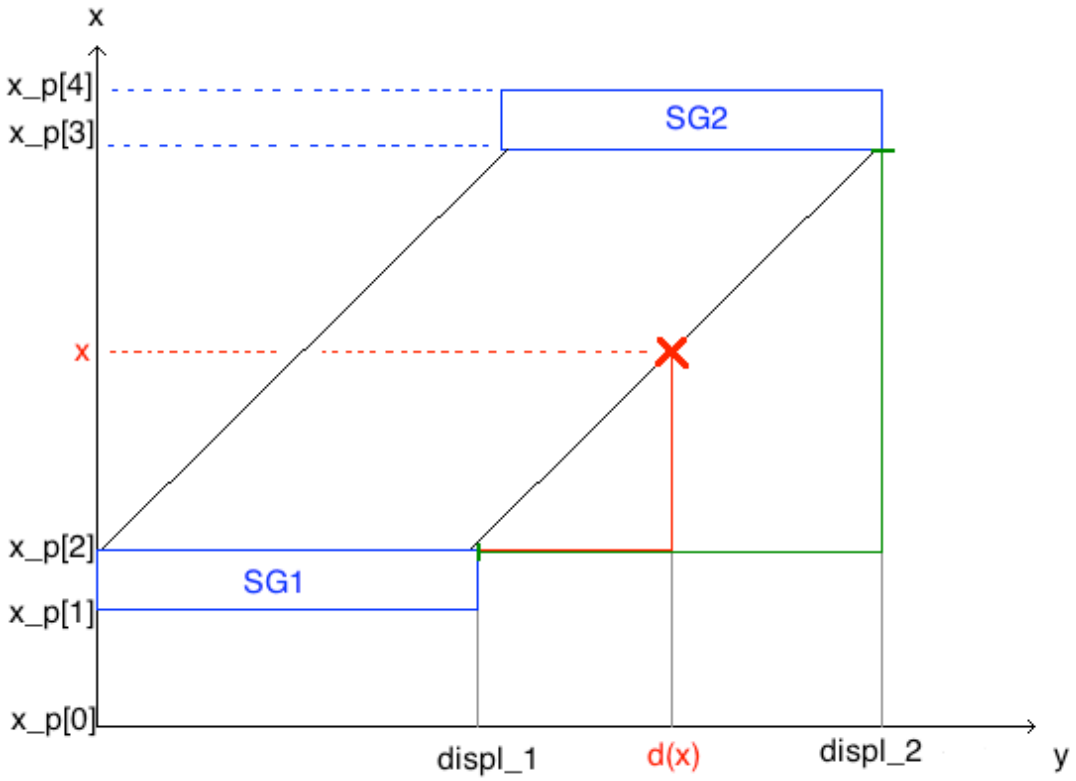

Figure 24: Similar Triangles method for Rod deformation.

The dimensions of the green triangle were already known: displ_1 and displ_2, as well as the x_position [2] & x_position [3]. Assuming that all Similar Triangles are proportional, the red triangle dimension quotient could be made equal to the green triangle quotient. Therefore, for any given point x along the Rod height, the differential displacement d (x) can be found:

$$\frac{\dfrac{d(x) - displ\_1}{x - (x_{pos}[2])}}{Red\ Triangle} = \frac{\dfrac{displ\_2 - displ\_1}{(x_{pos}[3]) - (x_{pos}[2])}}{Green\ Triangle}$$

Rearranging:

$$d(x) = displ\_1 + \frac{x - (x_{pos}[2])}{(x_{pos}[3]) - (x_{pos}[2])} \times (displ\_2 - displ\_1)$$

This linear interpolation equation d(x) was then inserted in the preprocessing file "*PreInputFile.ccl*" and run for every Rod Bundle, as shown in Appendix 7.1.

The next two figures show the plot and evaluation of the interpolation line for the Rod Bundle 2 8 (the eighth Rod Bundle of the second FA) in ANSYS CFX for verification purposes.

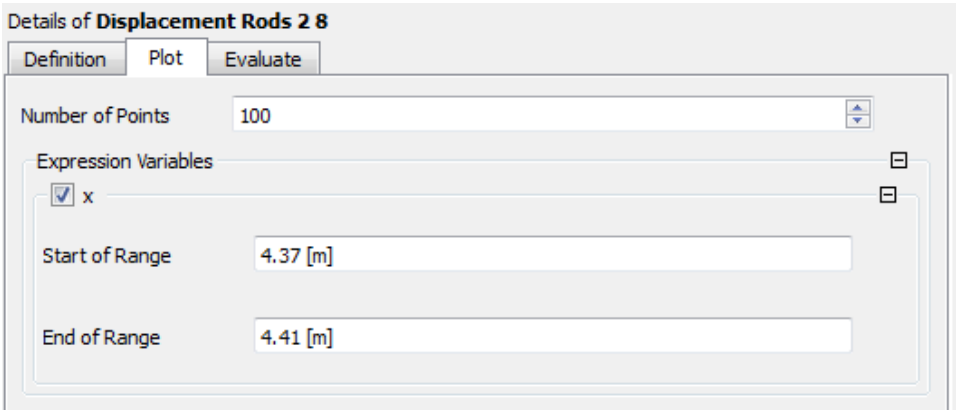

Figure 25: Plotting Range for the Rod Bundle 2 8.

Figure 26 confirms that Rod Bundle 2 8 is found at an axial height of around 4m and has experimented bowing in the dimensions of about 4mm.

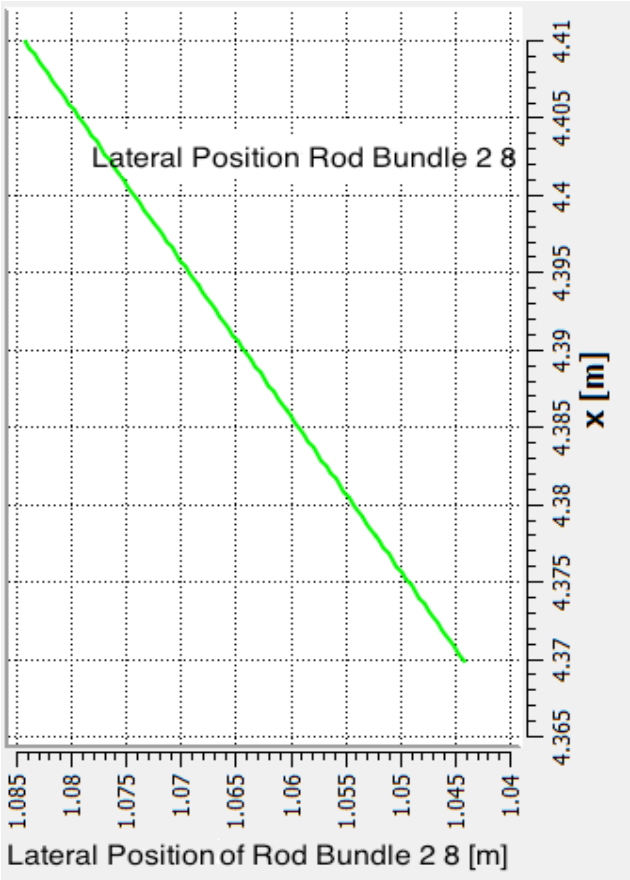

Figure 26: Lateral Position of Rod Bundle 2 8.

4.1.2 Implementing the Rotation of the Spacer Grids

The next step was using the *"rotz.csv"* file, in order to also calculate the extent up to which the Spacer Grids were rotated. The angle of the rotation of the Spacer Grids was given by APDL mechanical through the mentioned file, therefore it was only necessary to use this rotation angle to obtain a linear deformation equation that joined the lower part of the grid to the upper one.

Figure 27 shows SG 1 with and without rotation. By drawing a Centerline between x_pos [1] and x_pos [2], and considering the tan of angle Theta [tan(θ)], for any differential point of the adjacent leg x (in green), the respective opposite leg (in purple) can be found. This opposite leg will determine the linear equation (in red), which will represent the new deformed shape of the Spacer Grid with the given rotation Theta. Mathematically:

$$\tan(\theta) \times \left(x - \frac{x_{pos}[1] + X_{pos}[2]}{2} \right) = Opposite$$

where:

$$\frac{x_{pos}[1] + X_{pos}[2]}{2} = Centerline$$

Two possibilities exist:

1. The differential point x (in green) lies underneath the Centerline: the result of x – CL = a negative value. Therefore, tan (θ) multiplied by a negative adjacent will equal a negative opposite, which will result in a differential point (in red) to the left side of the original SG shape (in blue).

2. The differential point x (in green) lies above the Centerline: the result of x – CL = a positive value. Therefore, tan (θ) multiplied by a positive adjacent will equal a positive opposite which will result in a differential point (in red) to the right side of the original SG shape (in blue). Such as the one that would result from the purple opposite in Figure 27.

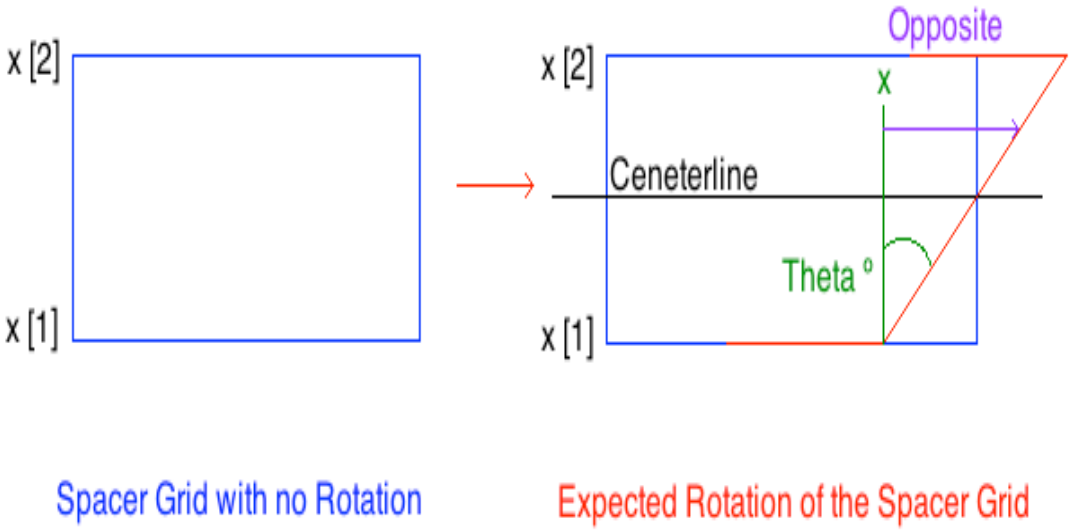

Figure 27: Spacer Grid Rotation Diagram.

Again, this trigonometric operation was inserted in the preprocessing file and run for each of the 9 Spacer Grids of every FA by iterative looping.

In the following figures, the definition, plot and evaluation of the rotation of SG 2 2 (the second Spacer Grid of the second FA) is shown in ANSYS CFX.

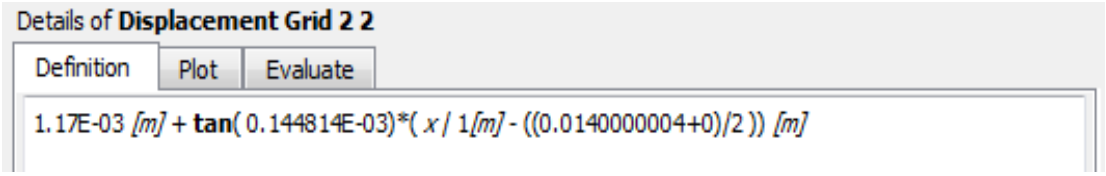

Figure 28: Displacement Equation of Spacer Grid 2 2.

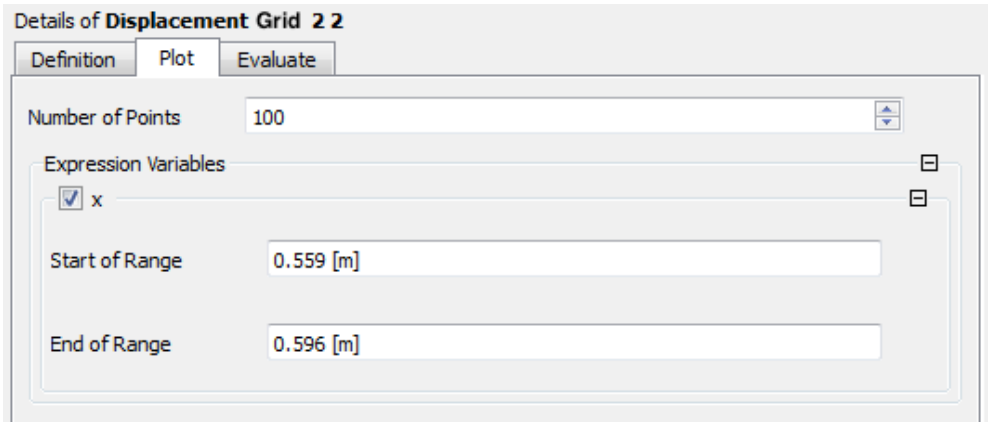

Figure 29: Plotting Range of Spacer Grid 2 2.

Figure 30 shows a clear example of the SG deformation that has been explained. In it we can see how SG 2 2 has rotated to the left. The height of the SG is of 4cm (in the axial direction), while the deformation it undergoes is of only 5 micrometers (5 E-6 and in the transversal direction). Although it is considerably low, the deformation should still be considered.

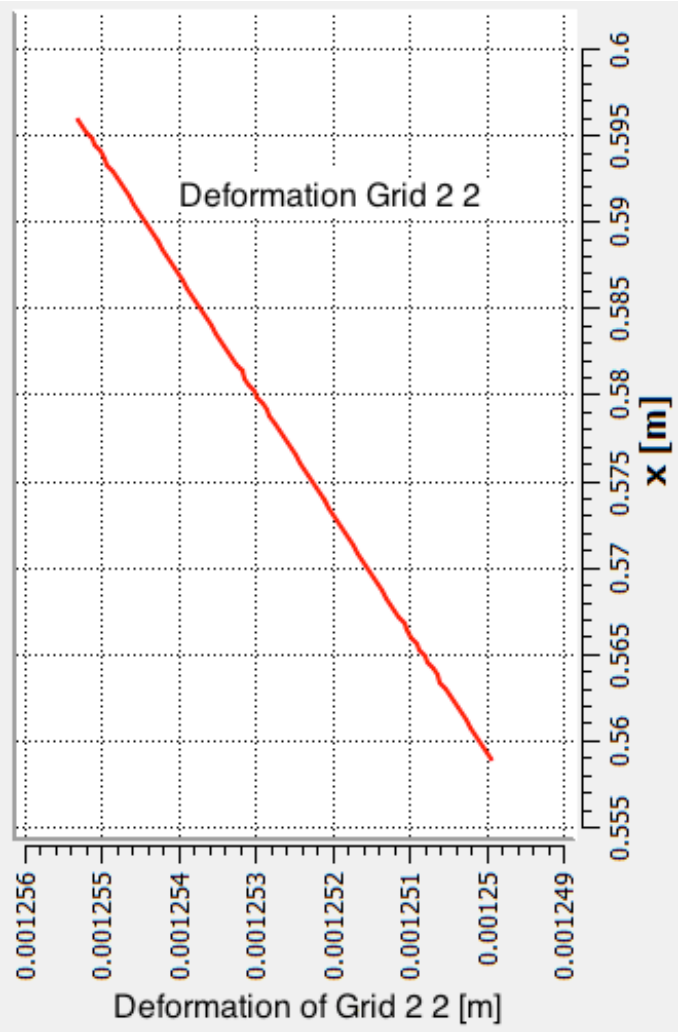

Figure 30: The Bowing-caused Deformation ocurring in Spacer Grid 2 2.

4.1.3 Adapting the Displacement of the Rods & SG to the Loss Coefficients (K) of the gaps.

The final step of the structural displacement transfer strategy was the adaptation of the original FA Gap geometry to the deformed FA Gap geometry. In other words, the work done in subsections 0 & 4.1.2 had been in charge of implementing the Rod and Spacer Grid structural deformation. Now, however, the geometry of the gaps between each FA had to be adapted to this deformation present in the whole structure.

As the porous model does not have any physically meshed gap region in it to avoid being too computationally expensive and also to improve convergence, the gap geometry was simulated by a step function of the Loss Coefficient (K). The Loss Coefficients dropped to a value of 0 in the 2 mm where the gaps were present (this can be seen in Figure 31). By implementing this step function for the Loss Coefficients, the gaps were defined and the result was equivalent to them being physically present.

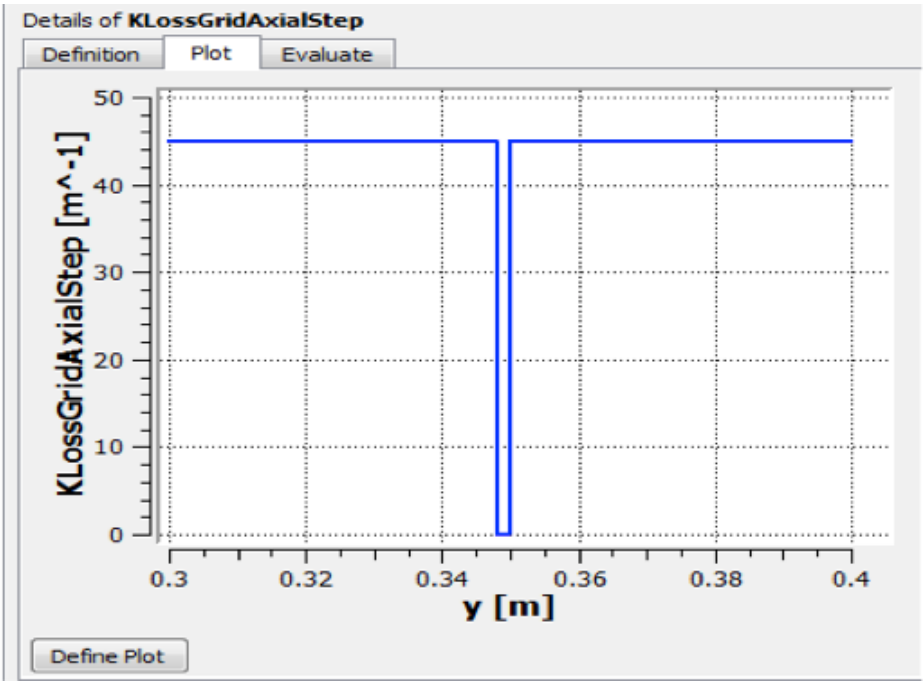

Figure 31: Axial Loss Coefficient (K) Gap Step Function.

The objective now was to transfer the displacements of each individual Rod and SG to its adjacent gap, in order to accurately simulate the deformed dimensions of the gap. Each gap was composed of two halves; the one determined by the FA to its left (and all the SG and Rod Bundles it was made of) and the one determined by the FA to its right (with the respective SG and Rod Bundle deformations, *different* from the ones on the left side FA).

Therefore, an important aspect that had to be considered, was the fact that it was necessary to define the 4 Loss Coefficients ($K_{loss\ rods\ crossflow}$, $K_{loss\ rods\ axial\ flow}$, $K_{loss\ \ grid\ crossflow}$, $K_{loss\ \ grid\ axial}$) inside every FA loop and for every individual FA, as these Loss Coefficients were used inside the given loops to create the “artificial” gaps.

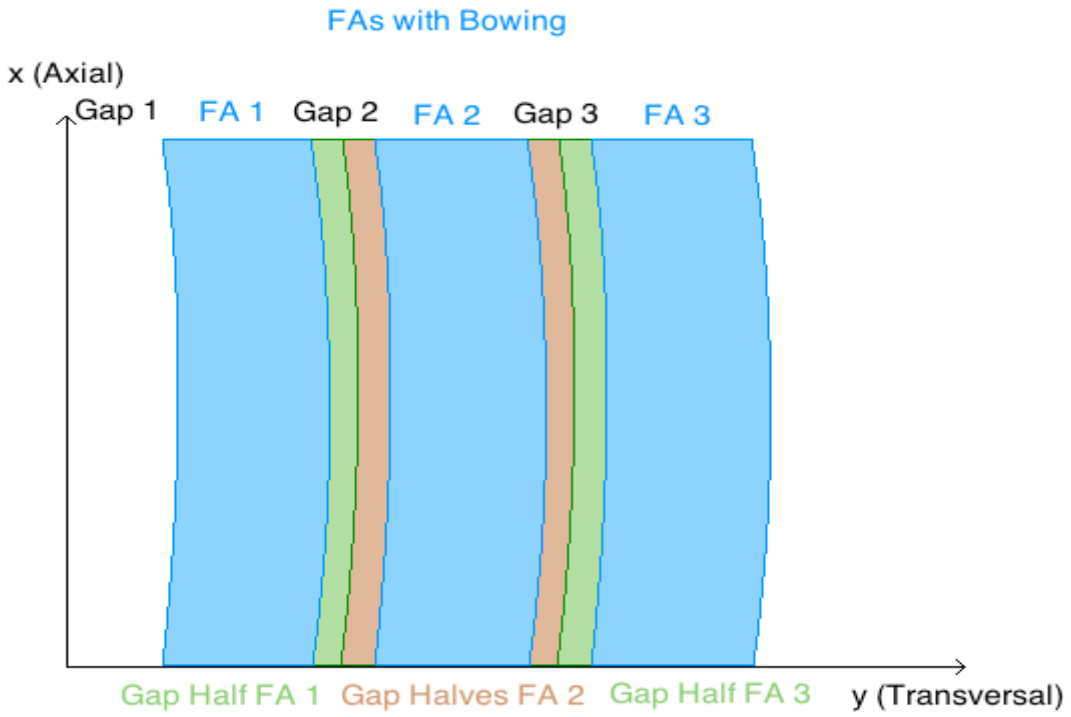

Figure 32: FA Gap Characterization.

Figure 32 reflects the idea behind the gap characterization. For each FA loop both halves of the adjacent gaps were defined. The numerical value of the 4 Loss Coefficients dropped to 0 in both the green and orange gaps (the gaps offer no opposition to flow). However, the location in which these coefficients dropped to 0 was no longer symmetrical or uniform. It no longer consisted of a straight 2 mm wide gap like in Figure 31, but instead it was composed by uneven linear equations, dependent on the bowing each SG or Rod Bundle had undergone.

The result of these displacements, was that some of the gaps inside the core closed completely, while others widened further. A nearly closed gap can be seen below in Figure 33.

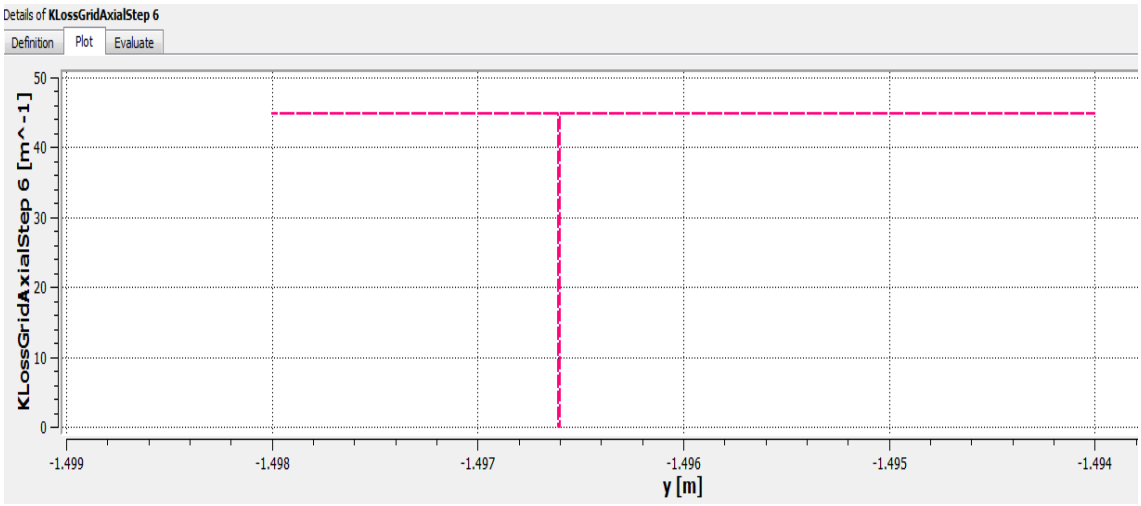

Figure 33: Closed Gap Step Function.

In Figure 34 the central FA is shown. Half of it falls on right of the origin and half on left. Meanwhile, the Loss Coefficient drops from 118 m^{-1} to 0 at -0.115 m and + 0.115m respectively (representing the end of the FA and the beginning of the gap). Appendix 7.1 shows the implementation of the step functions of the Loss Coefficients (K).

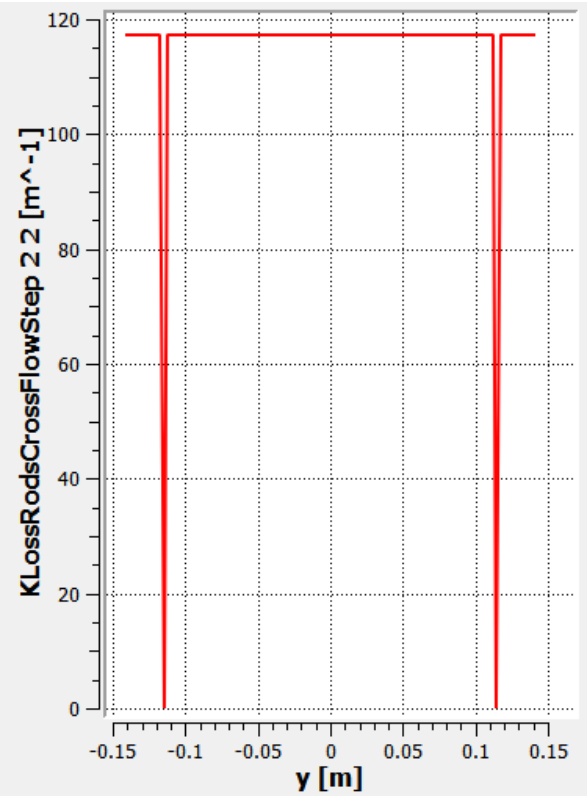

Figure 34: Graphical Representation of the central FA and its two gaps (-0.115 m to +0.115 m).

4.2 Mesh Displacement Transfer Strategy

After successfully implementing the structural displacements caused in the Spacer Grids and Rod Bundles, a next step in order to attain more precise results was deforming the Mesh according to the FA structural displacements. The result of subsection 4.1 was the creation of the mentioned Loss Coefficient gaps, which linked the deformation caused by the hydraulic loads to the new geometries of the FA-dividing gaps (no longer uniform as mentioned previously). This lead to an accuracy problem: the points in space where the new deformed gaps lie are no longer matching the parts of the Mesh with a higher resolution. The Mesh, originally, is finer close to the 2 mm where each non-deformed gap is present, this way better results can be obtained in the initial non-deformed conditions, as the higher losses and faster flow speeds in the gaps can be more precisely measured.

Now, however, the Mesh remains finer in the 2 mm where the old gaps used to be and coarser in the space where the new deformed gaps fall.

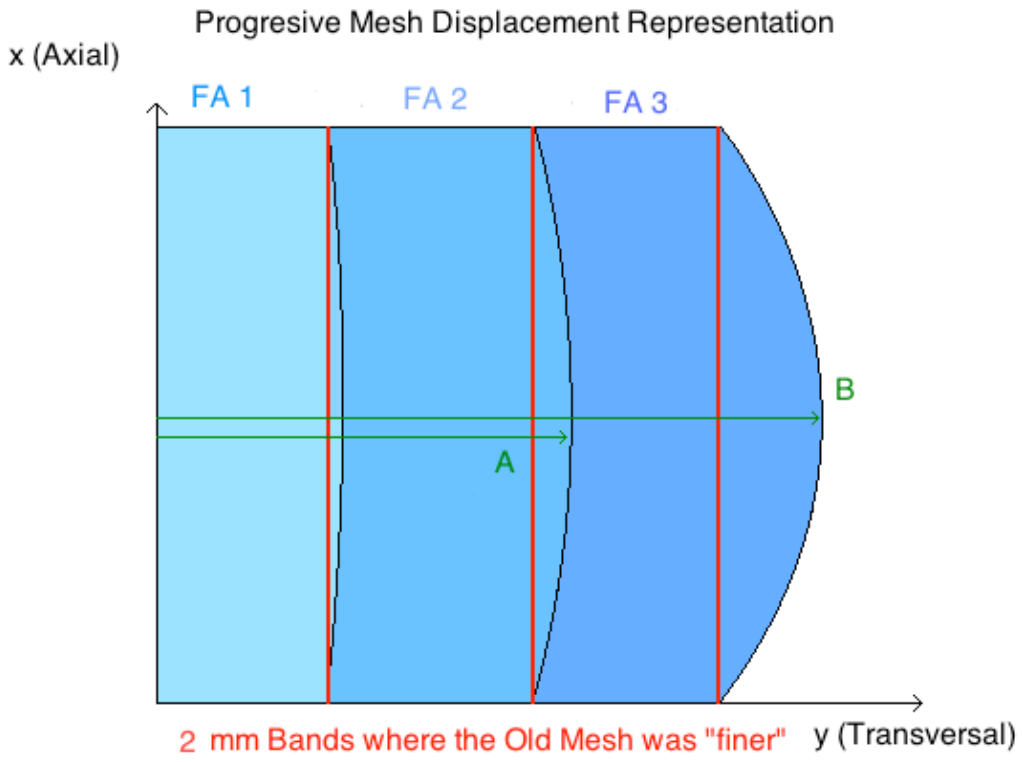

Figure 35: Mesh Displacement Representation with the "Finer" Old Mesh 2 mm Bands.

The solution to avoid this problem is relatively simple: the deformation of the SGs and Rods has to be pre-set in the actual Mesh also, in order for them to match and for the gap areas to be directly above the more "fine" areas of the Mesh. Figure 35 shows the deformation implemented into the Mesh (represented in several tones of blue). The old "finer" Bands of the Mesh (in red) have been shifted to the new border areas (in black), which will have the new gaps directly above them. It can be seen that the Mesh deformation is a gradual deformation from light blue (minimal deformation), to dark blue (which accounts for the deformation for the first three areas in the Mesh) and this would continue for all the 15 FAs.

The Mesh deformation can be done by using the variables created for the displacements of the grids and rods in 0 & 4.1.2. An interpolation line of the Mesh deformation can be calculated as a function of the Y co-ordinate position. Again in Figure 36, two green lines labeled A & B respectively account for this progressive Mesh deformation in Y.

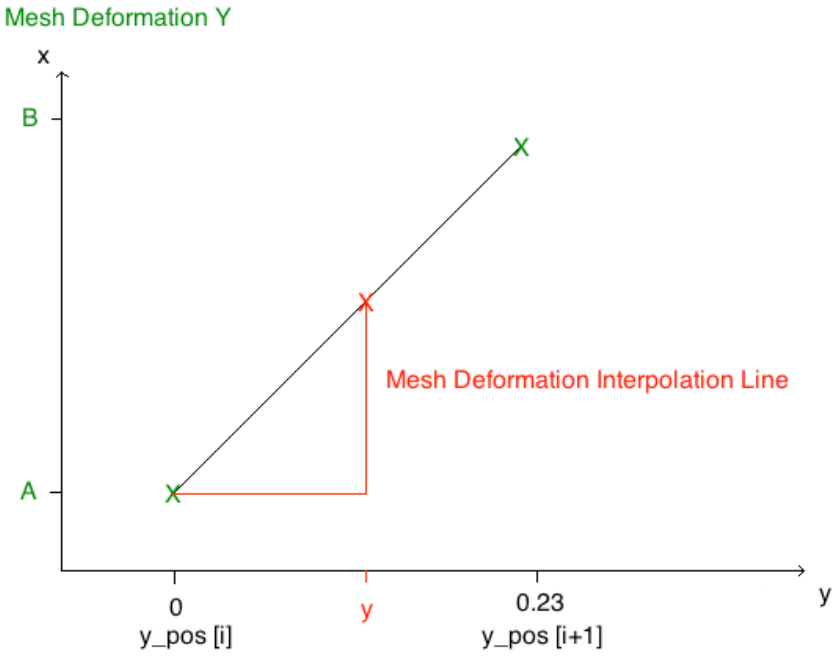

Figure 36: Similar Triangles Method for Mesh Deformation.

The interpolation line between A & B can be obtained as a function of the Y position (y_pos) by using the Similar Triangles method again (as in 0).

$$\frac{B - A}{FA\_width} = \frac{Interpolation\ Line}{y - y_{pos}[i]}$$

Rearranging:

$$d(y) = A + \frac{B - A}{FA\_width} \times (y - y_{pos}[i])$$

With B and A being the centerlines of the gaps between two displaced adjacent FAs in their correspondent Axial Level (SG 1-9 & Rods). Taking $j as the reference for the axial level numbering and $i as the FA number, the centerlines (for example B) would be calculated by subtracting the displacement of FA $i at an axial level $j (to the left of the centerline) from the displacement of FA $i+1 at that same axial level $j (to the right of the centerline) and then dividing by two. I.e.:

$$B = \frac{Displ.Grid\ \$(i+1)\ \$j - Displ.Grid\ \$i\ \$j}{2}$$

The results of the Mesh Deformation can be clearly seen in Figure 38, which shows the deformation caused by the S-shape bowing set of data seen in Figure 37. The structural displacements have been correctly transferred to the Mesh and follow the same pattern as the deformed structure itself. The S-shaped bowing is the highest in the axial levels Uy 4 & Uy 8 of

Figure 37. This results in Spacer Grids 3 & 7 being the two positions with maximum Mesh deformation (axial levels in green-to-blue & red-to-yellow-to-green-to-blue) in Figure 38.

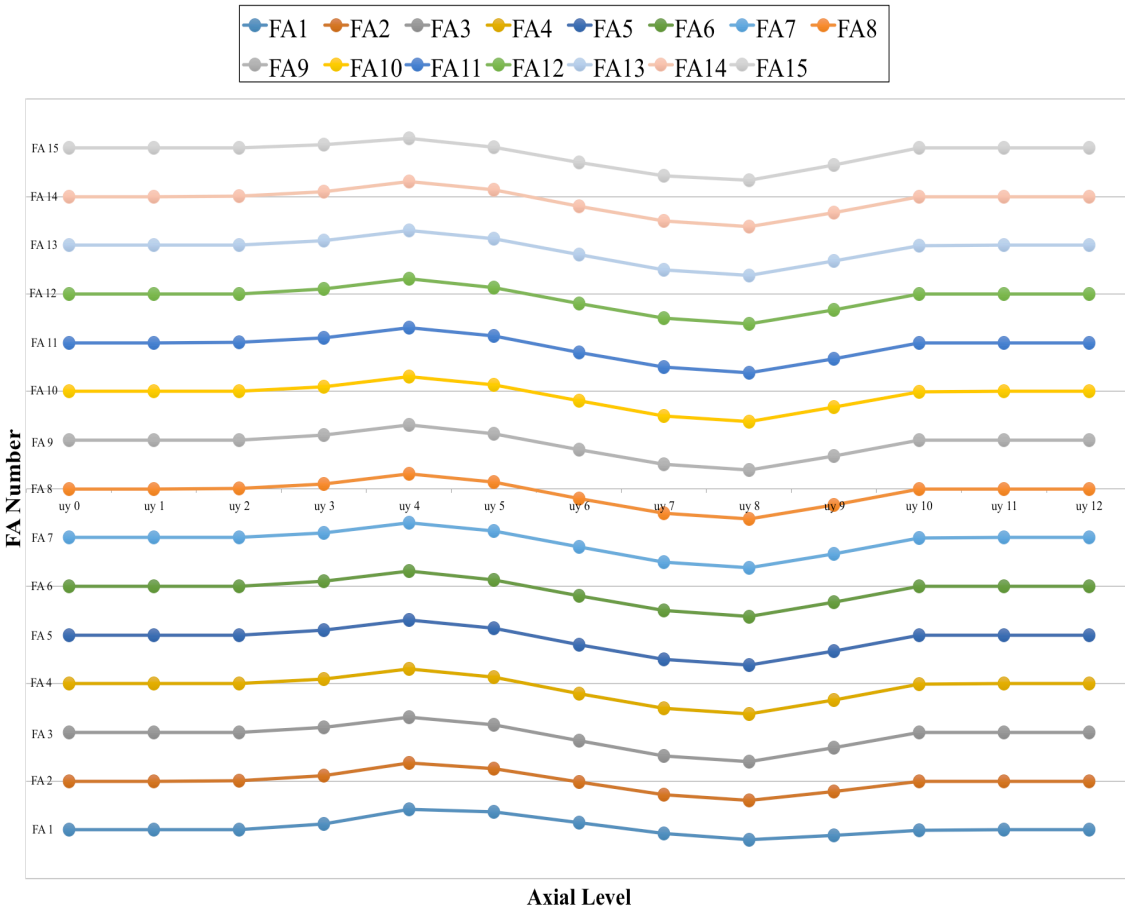

Figure 37: S-Shaped FA Bow deformation.

The immediate result of this Mesh displacement implementation is a higher degree of accuracy in the results. In fact, the hydraulic forces extracted from CFX where significantly different in certain parts of the core, hence motivating Subsection 4.3 and setting a path for further research.

Finally, Figure 39 verifies the result of the expected Mesh shift. It can be seen that SG 3 experiences a displacement of around + 3 mm, while SG 7 of - 6.4 mm, which then is interpolated gradually towards the rest of the axial directions. The chart represents an axial Sample Cut-Line drawn at a transversal position of -0.9 m (where the maximum deformation starts to occur in SG 7). In the plot of the transversal Mesh shift against the axial height, the inflexion points of SG 3 & 7 can bee seen. The maximum positive displacement of SG 3 (3 mm) is located at 1.2 m in the X–axis, and the maximum negative displacement of SG 7 (- 6 mm) is located at 3.4 m in the X–axis. The correct implementation of the S-shaped bowing into the CFD model is, therefore, proved.

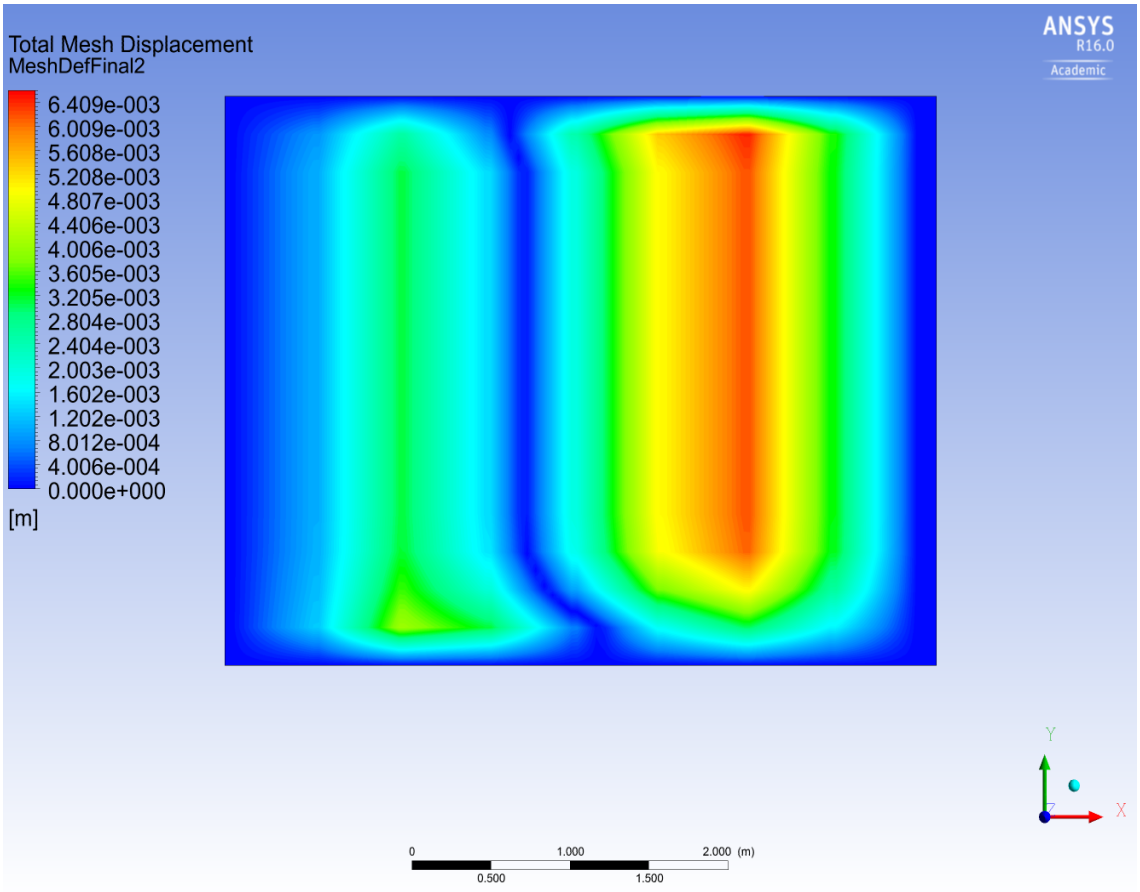

Figure 38: Deformed Mesh due to S-Shaped bowing.

As a last remark, the 9 Spacer Grids can been seen in Figure 39 as the 9 abrupt points linking the Rods (approximately at 0 m, 0.6 m, 1.2 m, 1.8 m… 3.4 m, 4 m, 4.5 m). It is only reasonable that the SGs are rougher points in the above chart, as SGs rotate differently from Rods due to their different geometry. In fact, this outcome reinforces the validity of the implementation of the Structural displacements.

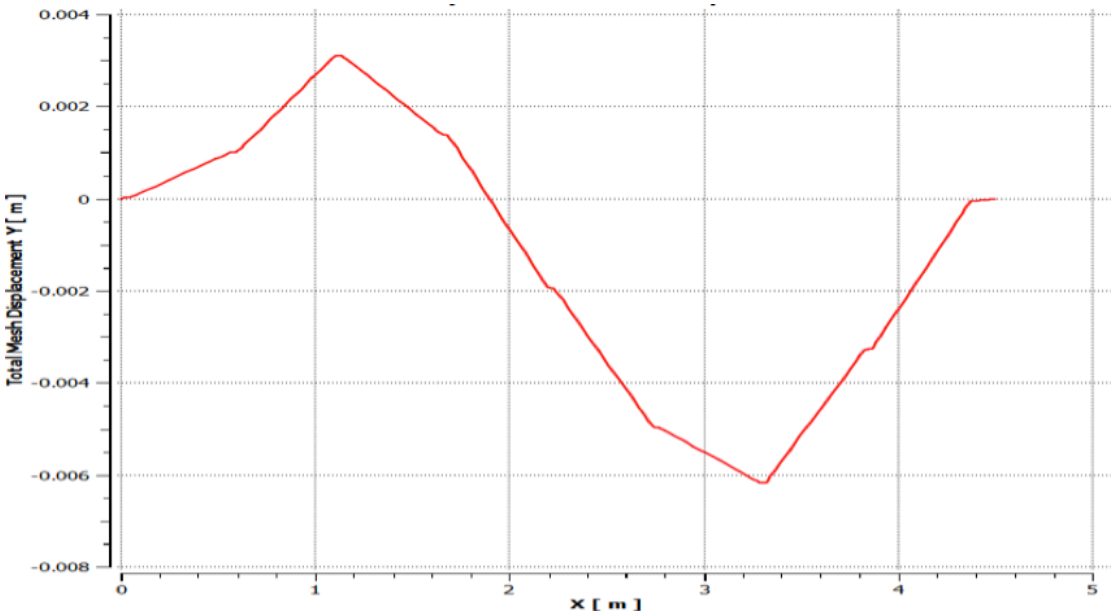

Figure 39: Cut Line of Transversal Mesh Displacement vs. Axial height.

4.3 Results & Scope of the Mesh Displacement Analysis

The outcome of the Axial and Transversal Hydraulic forces resulting from the Displaced Mesh analysis called for further explanation. In general, the results obtained were inside an acceptable deviation margin. However, in the case of the Transversal forces a very significant percentage difference appeared in the critical areas of the core (SG 3 + Rods 3 & SG 7 + Rods 7 & adjacents). Two approaches were taken to analyze the results: the Normalized Root Mean Square Deviation and the Relative Deviation.

4.3.1 Root Mean Square Deviation

For the deviation analysis, the Non-deformed Mesh Hydraulic forces results were taken as the predicted reference values, and the Deformed Mesh Hydraulic forces were considered the observed values. The Root Mean Square Deviation (RMSD) was used to measure the difference between both sets of results.

$$RMSD = \sqrt{\frac{1}{n} \times \sum_{t=1}^{n} (Yp - Yo)^2}$$

Equation 18: Root Mean Square Deviation. *(4-1)*

Setting “n” as the number of Fuel Assemblies (15), “Yp” as the Non-Deformed Mesh predicted values and “Yo” as the Deformed Mesh predicted values. The two sets of data were compared on the 19 axial levels determined by SGs 1-9 & Rods 1-10 (Appendix 7.1.4). The most problematic areas of the Mesh (SG 3 & SG 7 seen in subsection 4.2) resulted in the highest deviations. This is only logical, as the higher precision of the Deformed Mesh in areas of higher structural displacement, led to a greater difference in the results of the hydraulic forces.

4.3.2 Normalized Root Mean Square Deviation

The RMSD of the entire Mesh was also normalized both with reference to the normalized mean of the whole sample of the Non-deformed Mesh values and also with reference to the maximum value out of the whole set. This time it was calculated as a single value over the entire Mesh (not in each of the 19 axial levels).

Normalized RMSD of the axial forces X

RMSD (N)	Normalized. Mean (N)	Maximum Value (N)
0.675	117.24	140.66

Normalized RMSD (Mean) %	0.57
Normalized RMSD (Max.) %	0.48

Table 3: Normalized RMSD axial forces (μ, Max.).

Normalized RMSD of the transversal forces Y

RMSD (N)	Normalized. Mean (N)	Maximum Value (N)
0.282	3.88	11.82

Normalized RMSD (Mean) %	7.2
Normalized RMSD (Max.) %	2.4

Table 4: Normalized RMSD transversal forces (μ, Max.)

4.3.3 Relative Deviation

Finally, and as a third control measure the relative deviation from one data set to the other was also calculated and then the RMS of this relative deviation was done. The differences between the predicted and observed values were divided by the reference predicted values (from the Non-deformed Mesh).

RMS of the Relative Deviation: Axial Forces %	0.56
RMS of the Relative Deviation: Transversal Forces %	1.23

Table 5: Relative RMSD.

The RMS of the relative deviation of the axial forces was very close to the normalized RMSD and also under 1%. However, the RMS of the relative deviation of the transversal hydraulic forces (the most influential ones for this Thesis´s aim) was over 1% (1.23%). In addition the normalized RMSDs were also well over 1% (7,2% & 2,4%).

A closer look into the results showed that in the critical areas of the reactor, transversal hydraulic forces had a difference of up to 40% in their magnitude with and without Mesh Deformation. The fact that the axial forces were barely affected by a more precise Mesh and the transversal forces did have significant differences was, nevertheless, reasonable. Axial forces have a relatively "independent" nature to minor variations in the rotations and displacements within the reactor (the "cos θ" for the axial vertical component might vary slightly). The transversal components however are very sensitive to these minor variations caused by the more precise Mesh (the "sin θ" for the transversal component can change from 0 to a given value).

Having proved that such a considerable difference can be caused by the Mesh fineness, the base is set for further research concerning a Mesh optimization & precision study. This extended research, however, falls out of the scope of this Thesis. It is because of this that this Thesis will move on to implementing a Non-deformed Mesh only and conclude up to what extent the FSI Interface affects the Bowing phenomenon in a Non-deformed Mesh.

4.4 The Linux Interface & Shell Script

Once the Structural displacements and the Mesh accuracy problem had been dealt with, the time had come to automate the load and data transfer by working in a Linux environment. The objective was to create a Shell Script that would successfully reproduce the displacement transfer strategy, without the need of executing the ANSYS CFX Graphical User Interface (very computationally expensive, considerably slower and also impossible to automate and loop with no interaction of the user). The mentioned Shell Script would contain all the necessary commands so that with a single submission of the file to the Linux cluster, the output data containing the Hydraulic Loads could be delivered to APDL Mechanical and, in the following time step, the structural displacements (calculated by APDL Mechanical with these given Hydraulic Loads) could be used by CFX to generate the next set of Hydraulic Loads.

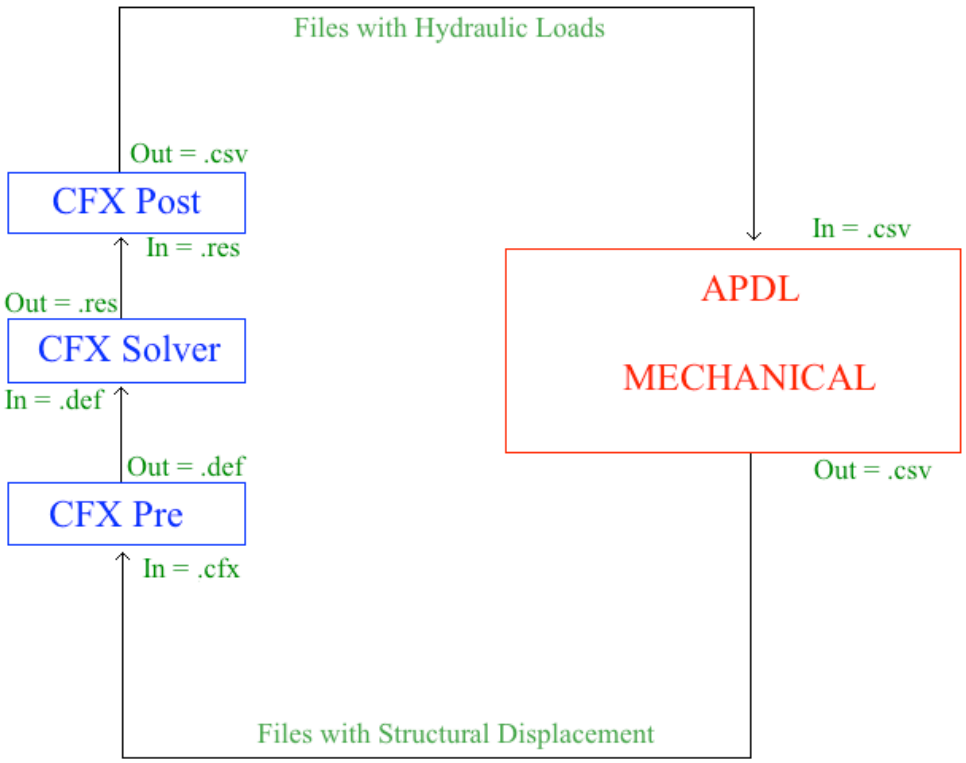

Figure 40: Displacement Transfer Strategy implemented in the Linux environment.

Figure 40 shows a simplified scheme of the data transfer the Shell Script intended to automate. The initial loop would start by using the Structural Deformation Excel files created by APDL Mechanical: *"displacementsy.csv"*, *"gaps.csv"*, *"rotz.csv"* (previously introduced in subsection 4.1). CFX Pre would have the file *"SingleFA_DetailPart3.cfx5"* as input data to generate the Mesh and would then append the modified *"PreInputFile.ccl"* file, which would implement the studied Structural displacements and Mesh Deformation (retrieved from the .csv files coming from APDL Mechanical, Appendix 7.1.2 & 7.1.3). With this information it would then create the CFX Solver input file: *"FinalMesh.def"*. CFX Solver, after carrying out iterative loops until the convergence criterion is reached, would forward the solution results file *"FinalMesh.res"* to CFX Post.

Following up after the calculation of these results, the actual new Hydraulic Loads would then be extracted by the "*PostProcXYForce.cse"* file (Subsection 4.4.2 & Appendix 7.1.5) provided by [9]. Finally, these would be submitted to APDL Mechanical again and the new Structural displacements caused by these Hydraulic Loads would be used as the starting point for the second iterative loop.

4.4.1 Creating the Hydraulic Shell Script

The Shell Script itself would be written in Bash command language. Instead of using the Bash command processor and having to enter the desired commands in the command window, a Shell script was determined as the best way to implement the looping between Hydraulic and Structural data transfer, with the appropriate time step being set up within the script.

The initial script only aimed at including the hydraulic part of the FSI interface, that is to say, what had been done up to now by the ANSYS CFX GUI, marked in blue in Figure 40. The three main commands obtained from the ANSYS manual were Cfx5pre, Cfx5solve and Cfx5post. Each one would do the task assigned to it in batch mode:

- **Cfx5pre**: Generate the Mesh with the *"basename*.cfx"* file (explained in Subsection 4.4) and run the session *"basename *.pre"* to load the "*.ccl"* files and create the "*.def"* file.
- **Cfx5solver**: run the *"basename*.def"* file created above, and iteratively solve and record it in a *".res"* file.
- **Cfx5post**: extract the Hydraulic Loads from the *"basename*.res"* file and transfer them to a "*.csv"* file by using the mentioned "*PostProcXYForce.cse"*.

```
#!/bin/bash

##Load Cfx Mesh and run the session##

cfx5pre -batch $(basename *.pre) $(basename *.cfx)



##Run the solver with the .def file and obtain a result file##

cfx5solve -def $(basename *.def)



#Run the .cse session to extract the hydraulic loads from the results and later erase the result file##

cfx5post -batch $(basename *.cse) $(basename *.res)

rm -f $(basename *.res)

```

Figure 41: Hydraulic Interface Shell Script.

As seen in Figure 41, the Hydraulic script also had to include a small but relevant command: removing the *".res"* file after it had been used by Cfx Post and after the Hydraulic loads had been obtained. This was a necessary step towards facing the coupling with the Structural interface, as the results file could not be overwritten. Therefore, if it was not eliminated, each loop would create a new result file and Cfx Post would not know which one to use and which one was the most recent and valid one (the command *$basename*.res* assumes there is only one *.res* file in the working directory).

4.4.2 Extracting the Hydraulic Loads – Inertial Systems [17]

The extraction of the Hydraulic forces from CFX Post was done by the file "*PostProcXYForce.cse"*, as mentioned in Subsection 4.4. The file, however, requires a brief explanation, as it is operation is very related to fluid mechanics and the dynamics of a fluid.

Within the nuclear PWR the conservation laws of fluid dynamics have to be fulfilled. This Thesis uses the *Conservation of Momentum Law* (briefly explained in Subsection 2.1.1) to extract and obtain the Hydraulic X & Y forces that result inside the rector.

First of all it is necessary to say that, for the setting of the control volume and control surface (CV & CS) and also of the reference system (RS) a stationary state is considered. Both the CV & RS are inertial systems (uniform velocities). This permeates the grouping of the terms of the Reynolds Drag Theorem (RDT):

$$\sum \vec{F_{Ext}} = \frac{d}{dt}\int_{CV} \vec{v}\rho \, dV \; + \int_{CS} \vec{v}\rho \, (\vec{v_{r,CS}} \; d\vec{A})$$

Equation 19: Reynolds Drag Theorem for an inertial system. *(4-2)*

Equation 19 contains three velocities that need to be explained:

- The one inside the CV integral is the velocity with respect to the RS (inertial) of each of the particles within the CV.
- The one inside the CS integral is the velocity with respect to the RS (inertial) of each of the particles travelling through the CS.
- The Vr that appears inside the CS integral is the velocity of each of the particles that cross the CS with respect to the CS itself. In the case of a fixed and non-deformable CV (CS does not move), these last two velocities will be equal.

Meanwhile, the term related to exterior Forces in Equation 19, contains any exterior force applied from the surrounding to the CV (or more precisely, to the fluid that fills the CV at any given time). The following force requires a brief explanation:

- Pressure Forces: these are applied upon the surface areas through which fluid enters or leaves the CV. They are caused due to the fact that the CV is "fictionaly" separated from the rest of the fluid by these precise control surfaces. Therefore, the surrounding fluid exerts a pressure force on the CV and vice-versa.
- Shear forces: these are applied upon all of the six surfaces of the CV by the fluid surrounding it. Shear forces can be understood as deriving from surface tension.

Assuming uniform properties both in the CS & CV and separating into volumetric forces and pressure forces, the equation of *Conservation of Momentum* for the given CV is left as:

$$\sum \vec{F_{Ext}} = \frac{d\,(m\,\vec{v})_{CV}}{dt} + \sum_{Outlets\ i} (\vec{v}\,\rho\,Q)_i - \sum_{Inlets\ j} (\vec{v}\,\rho\,Q)_j$$

Equation 20: Conservation of Momentum Equation. *(4-3)*

In the case of permanent regime, where local variations of properties are zero:

$$\sum \vec{F_{Ext}} = \sum_{Outlets\ i} (\vec{v}\,\rho\,Q)_i - \sum_{Inlets\ j} (\vec{v}\,\rho\,Q)_j$$

Equation 21: Conservation of Momentum Equation in permanent regime. *(4-4)*

Therefore, the "*PostProcXYForce.cse*" file used to extract the hydraulic loads has only to set a given CV with six CS within the reactor and apply these laws of Fluid Mechanics to obtain *forces_y* & *forces_x*. As Figure 42 briefly shows. See also Appendix 7.1.5.

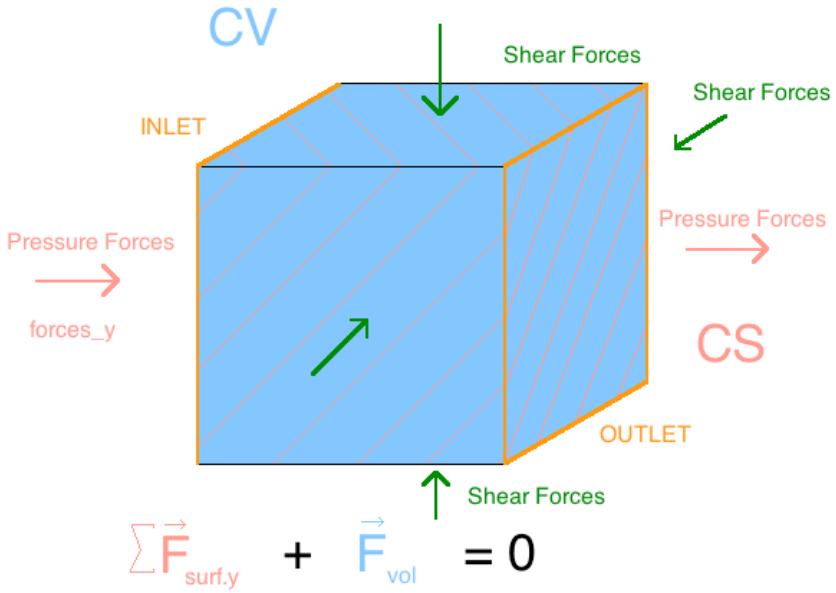

Figure 42: CV for the Conservation of Momentum within the PWR.

4.4.3 The FSI Interface as a whole: Coupling implementation

Having created a functional script for the Hydraulic part of the interface, the next step was to couple the work with the structural part of the interface (right hand side of Figure 40). The one-way coupling method that had been theoretically explained in Subsection 3.3, now had to be designed and practically implemented.

The initial approach that was selected was that of taking a state of *0 Displacement* as a starting point and then running the first hydraulic force loads to obtain a structural base state representing time = 0 h. Therefore, in this first state (Δto), the structure would have no creep strain, as Figure 43 shows.

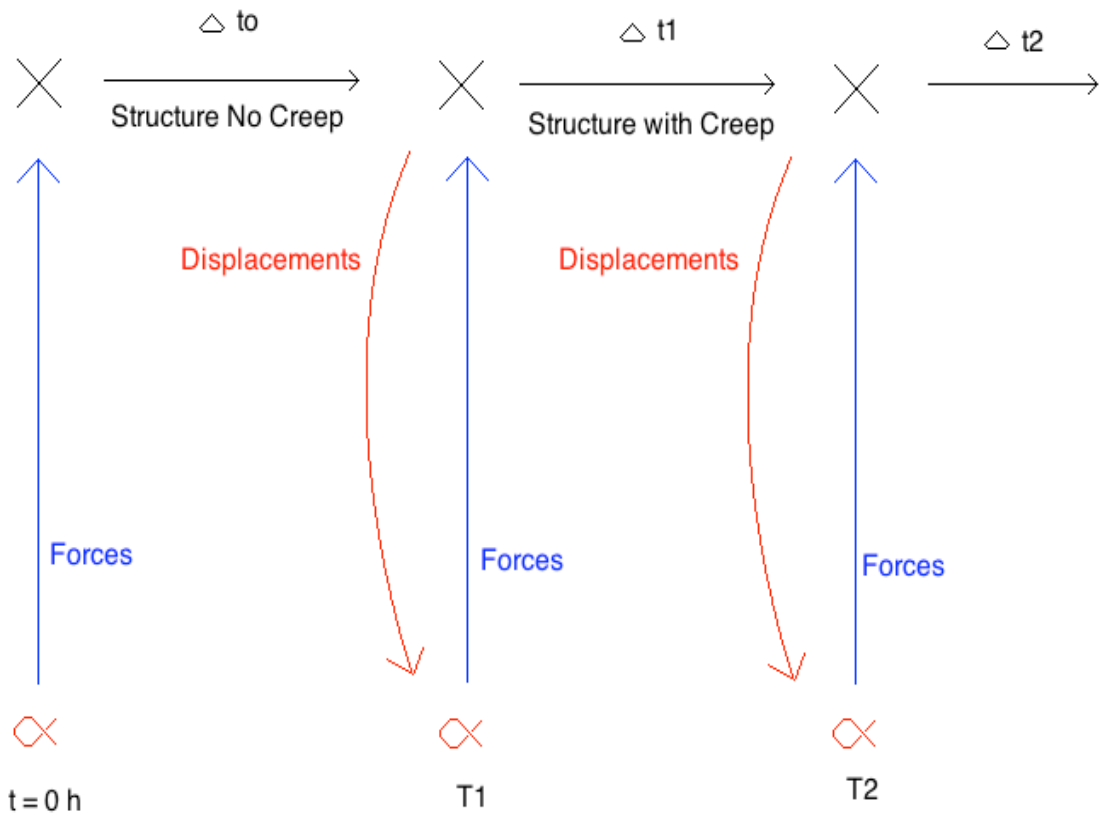

Figure 43: FSI Interface Coupling Time Steps.

The operation of a Nuclear power plants is divided into cycles. Each cycle usually lasts between 12-18 months having an outage for refueling and for security measures verification. Approximately around 1/3 of the nuclear fuel is renovated per cycle. The usual PWR operates 24 hours a day and has around 35 days of refueling outage time per year. This results in 7924 operational hours per cycle (assuming a 12 month cycle).

As the Hydraulic part of the coupling was a steady state simulation and hence, time independent, this Thesis related the time dependency of the FSI interface exclusively to the mechanical part of the coupling. To be more precise, the time parameter was defined exclusively by the creep rate, whose time scale is long compared to inertial effects.

Therefore, after the initialization run of the hydraulic loads at t = 0 h, an arbitrary starting Time 1 (T1) was set at 1 h. Taking into account the operational hours of a PWR complete cycle, a reasonable maximum coupling time step of 1000 hours was fixed. APDL Mechanical would, as a result, complete 8 loops with 8 different hydraulic loads as input for each one. Each loop would have 1000 hours to account for the creep-related structural displacements except the last one, of duration 924 hours.

The outputs of the simulations would be classified into a series of *".csv"* files ranging from 1-9 for both *forces_y* & *forces_x.* The file *"forcesy_1.csv"* for example, would include the initialization run and the forces of the non-creeped structure. The file *"forcesy_2.csv"*, would contain the hydraulic transversal forces at stage T1. The file *"forcesy_3.csv"*, would contain the hydraulic transversal forces resulting after the first coupling time step of 1000 hours had taken place and APDL Mechanical had accounted for 1000 hours of structural creep, and so on…. Finally the last file: *"forcesy_9.csv"*, would comprise the hydraulic loads resulting prior to the last 924-hour cycle.

5 Results

5.1 Qualitative analysis

To begin with the analysis of the results, this Thesis first took a qualitative look at the outcome of the PWR behavior with and without structural displacement. The reference parameter used was the axial velocity (Vu) within the core.

Although the relevant forces for the objective of this Thesis were the lateral Hydraulic forces (*transversal direction*), the fact that these transversal forces would deform the *axial* geometry of the core had to be understood. That is to say, the most visual way with which to detect any influence of lateral hydraulic forces acting on the PWR, was with analysis of the core axial velocity profile. This velocity profile was significantly affected by any variation in the core geometry; the FAs bowing to a greater or lesser extent would lead to the gaps in between themselves being narrowed down until closure, or widened further.

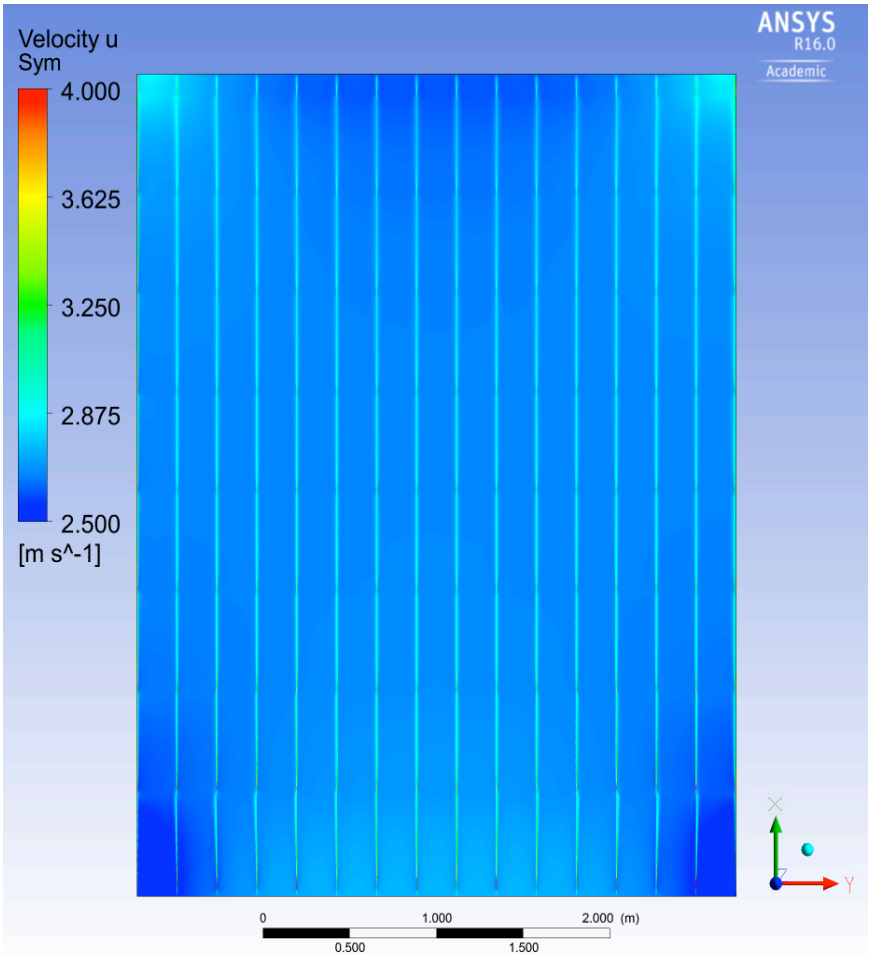

Figure 44: Axial Velocity Profile of the non-deformed core.

Figure 44 shows the axial velocity profile of the non-deformed core (without structural displacements). A continuous and symmetrical profile can be observed, with 15 well-defined FAs (in dark blue) separated by 14 gaps of constant width (in light blue-green). According to the CFX Post results the approximate superficial velocity of the fluid along the FAs is of 2,5 ms^{-1}, while the estimated velocity of the fluid up the gaps is 3,0 ms^{-1}. This represents a rough increase of 20%.

Meanwhile, Figure 45 displays the axial velocity profile of the deformed core with the structural deformations implemented into it. The profile is no longer continuous, nor is it symmetrical; the 15 FAs can be intuited but not easily counted. At the same time the gaps no longer have a constant width.

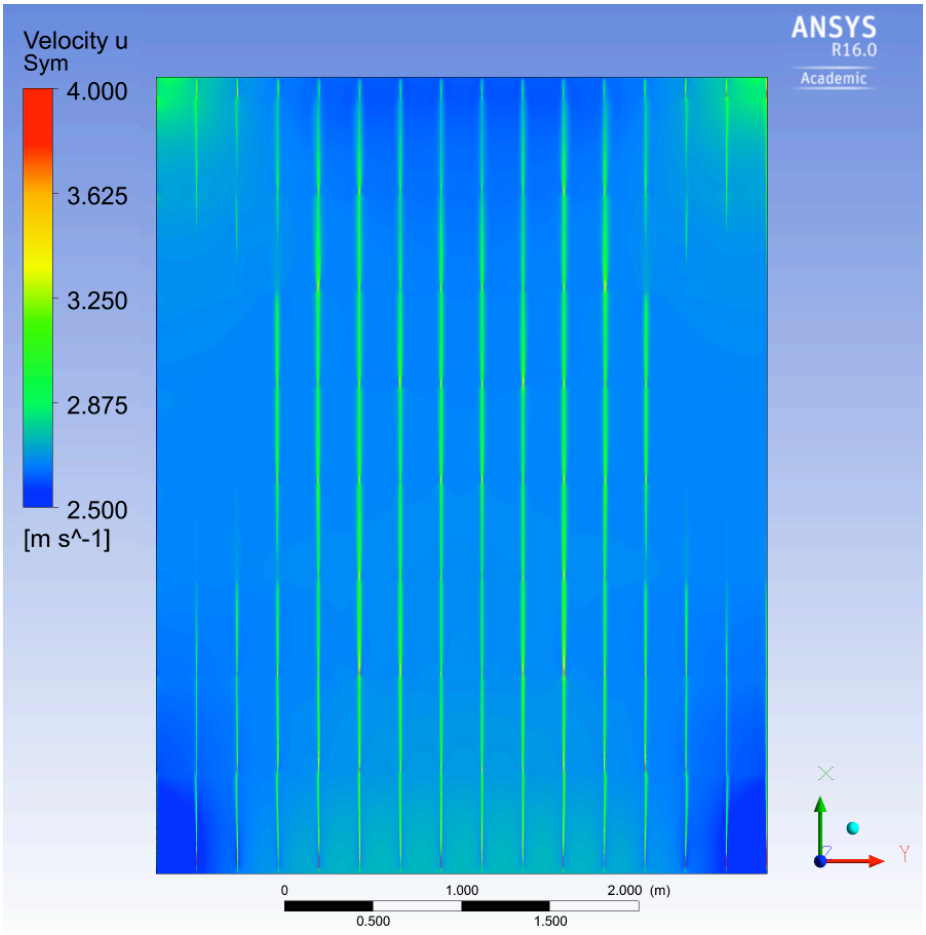

Figure 45: Axial Velocity Profile of the deformed core.

Taking a closer look at the core, it can be seen that the first and last FAs are now under direct physical contact; starting with FAs 1-3 in the left part of the profile, which blend into an "imaginary" single FA from 2m of axial height on. As the displacement profile implemented is symmetrical, results also show quite exact symmetry (minor deviations occur due to simulation differences). Therefore, at the right part of the velocity profile, FAs 13-15 also blend into another "imaginary" single FA from 2m of height on. In the meantime, the central gaps separating FAs 5-11 have widened further due to the bowing towards the outer part of the core (as explained in Subsection 1.5.2). The average percentage increase of the velocity magnitude within these gaps is of up to 10%.

All these observations of the new velocity profile match the expected outcome that would result from a C-shaped bowed core. Figure 46 represents the FA Bow patterns within a reactor. The trend followed is that the predominant pattern of the lateral hydraulic forces tend to travel from the center of the core towards the outsides, increasing their magnitude in the outer perimeter of the PWR and causing a greater structural displacement, as Figure 10 showed in Subsection 1.5.2.

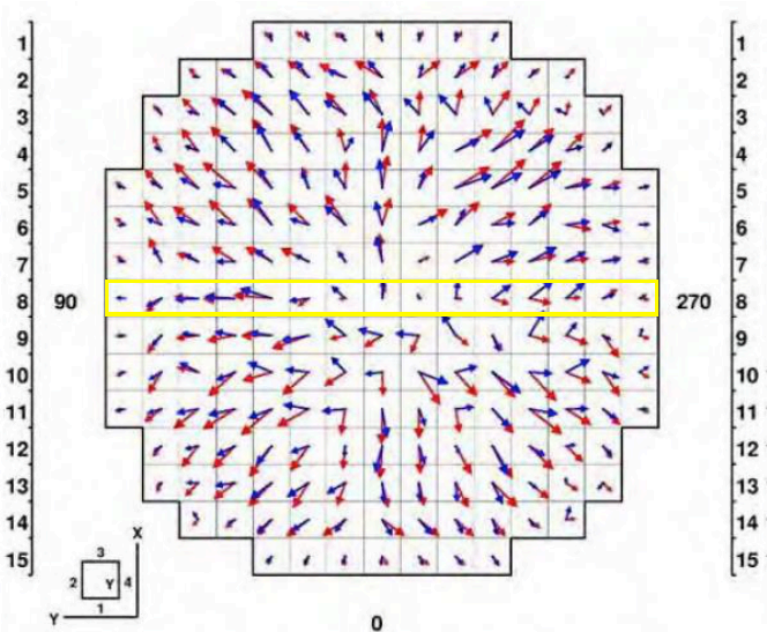

Figure 46: FA Bow Patterns with reactor measurements (blue) and predictions (red) [11].

Figure 45 represents the central row of the core seen in Figure 46 (marked in yellow). It can, hence, be understood that the FA Bow pattern seen leads to the C-Shaped structural deformation shown in Figure 47, which in turn results in the explained velocity profile.

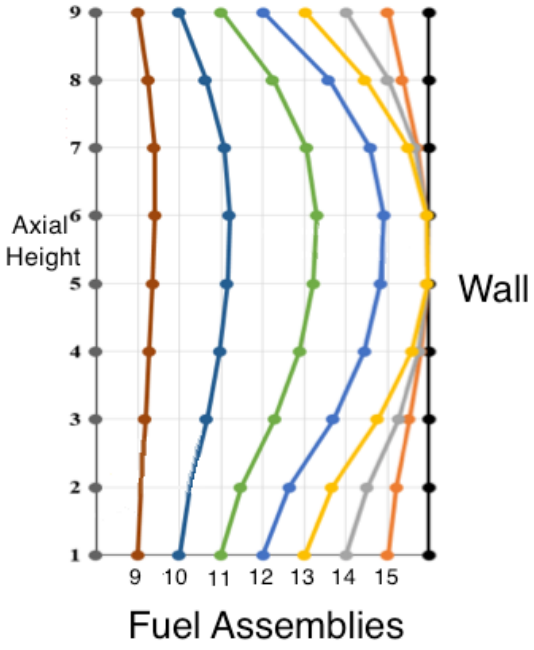

Figure 47: C-Shaped Bowing of the FAs 9-15.

Figure 47 represents FAs 9-15 ranging from the center of the core to the exterior wall. Seen in Figure 46 it reproduces the right hand side of the central row. The greatest deformation occurs in FAs 12 & 13 (light blue and yellow), this accounts for the closing of the gaps in the velocity profile. The wall will act as a rigid barrier against which FA number 15 will impact, limiting the further deformation of the previous FAs.

5.2 Theoretical explanation

Before going on to a quantitative analysis of the results, this Thesis will briefly explain the reason for the observed C-Shaped bowing in the PWR.

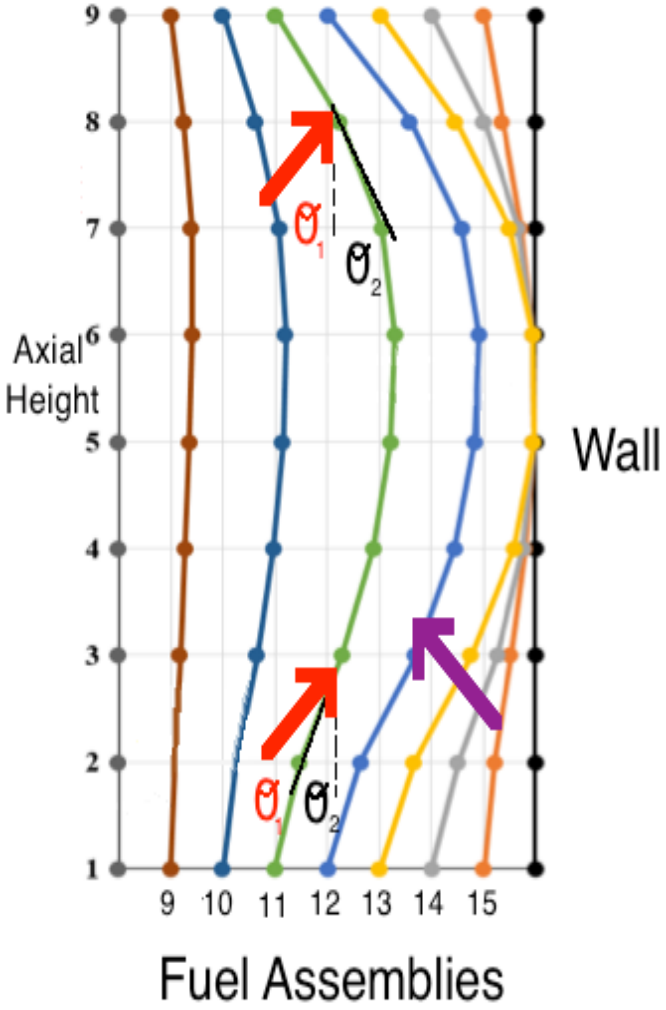

Figure 48: Angles of Attack in C-Shaped bowing.

When the coolant fluid enters the lower part of the PWR, the lateral hydraulic forces travel from the center of the core towards the outsides. Initially, these lateral hydraulic forces (marked in red in Figure 48) will all have a certain angle of attack on the vertical, non-deformed rods (θ_0). The hydraulic forces have a significant transversal component, but it is important to recall that they will also mostly have a positive axial component (coolant travels *up* the core). The composition of the lateral hydraulic loads by these two vector components is responsible for the C-Shaped form of FA bowing, and hence for the backflow going back to the center of the core as a result of the exterior gaps narrowing and redirecting flow (marked in purple in Figure 48).

As the FSI interface operates and the rods start to experiment the bowing phenomenon, the angle of attack of the hydraulic loads on the rods will start to change (Subsection 3.2.2). In the bottom part of the core (axial height 2) the angle of attack of the loads will be determined by the resultant of (θ_1 - θ_2), marked in red and black in Figure 48: the FA is fixed to the ground of the core and the bowing of the rods happens *solidarily* to the main hydraulic load direction, therefore, the angle of attack gets smaller. Meanwhile, in the top of the core (axial height 8) the angle of attack of the loads on the rods will be (θ_1 + θ_2), as the FA is fixed to the top of the core instead and the bowing this time will happen *against* the hydraulic load direction. The

evolution of the FSI will promote this structural effect in each loop and eventually lead to the pronounced C-Shaped bowing. Another consequence of this deformation will be the backflow of the hydraulic loads trying to “squeeze through” the only available and wider areas of the core (the central gaps between FA 8 - 10). This will happen as a result of the impact of the loads against the wall of the core and the gaps besides the wall being completely closed (between FA 14 - 15).

5.3 Quantitative analysis

5.3.1 Hydraulic Forces analysis

To begin with the quantitative analysis, the characterization and the magnitude of the Hydraulic Loads that were being measured had to be carried out. Two separate studies were carried out:

- First, an initial review of the hydraulic loads at time T_0 (See Subsection 4.4.3); before the 8 iterative FSI coupling loops had been completed.
- Second, a comparative force deviation analysis between the resulting transversal forces after loop 8 and the initial transversal forces resulting with no FSI.

Transversal Hydraulic Loads at time T_0

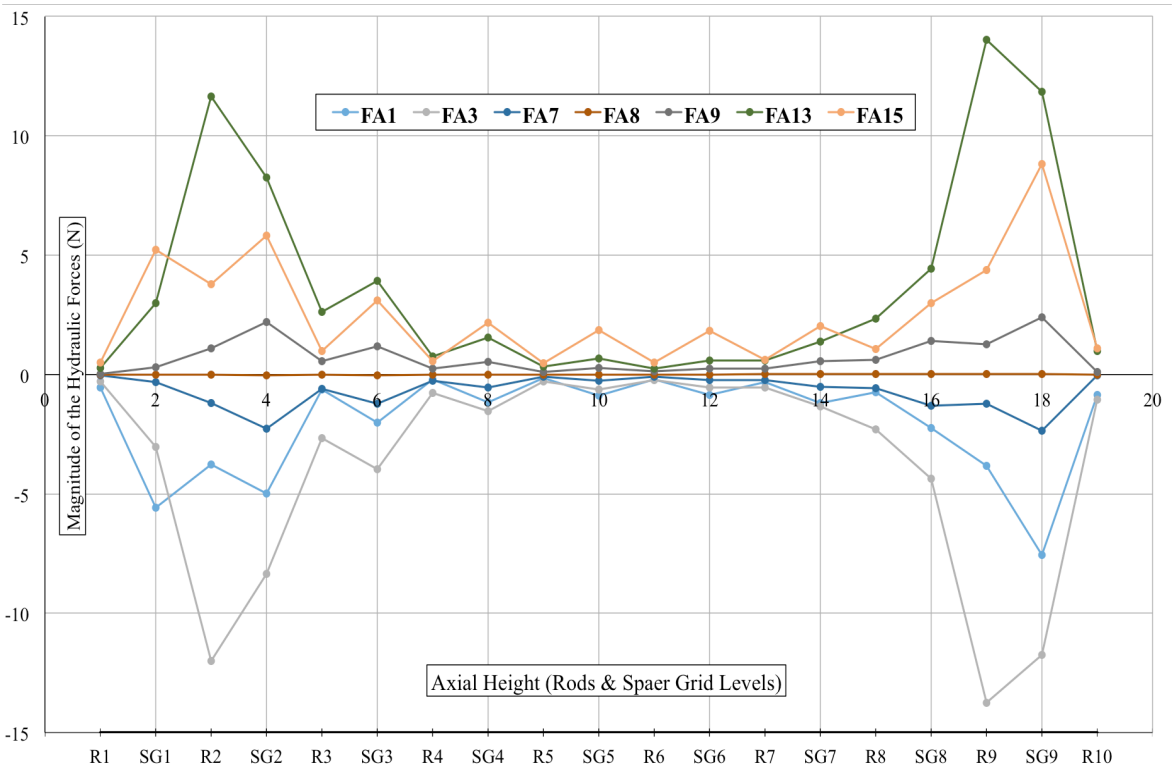

Figure 49: Transversal Hydraulic Forces in the core (N) v.s Axial Height (Axial Levels).

Figure 49 represents the transversal forces applied to the core structure at time T1. In it, the 7 most representative FAs are included: the central FA (FA 8) that has a neutral force profile with

0 N along all the axial levels; the two FAs adjacent to the central one (FA 7 & FA 9); the two exterior FAs (FA 1 & FA 15); and finally the two FAs neighboring the exterior ones (FA 3 & FA 13). The graph shows the 19 axial levels composing a FA (Rods 1-10 + Spacer Grids 1-9) plotted against the absolute values of the Hydraulic Loads measured at each axial level and for each FA.

Several observations can be made. To begin with, the symmetrical condition described qualitatively in Subsection 5.1 is, to a large extent, verified. Except minor differences due to computational simulation variations, FAs 1 & 3 & 7 are a consistent reflection of FAs 9 & 13 & 15. The consideration taken in Figure 10 is also corroborated. The load profile distribution followed by any of the FAs is that of two peaks (12-14 N) in the axial heights corresponding to Rods 2 & 9, and a decrease to much lower values (0-2 N) towards the mid-height of the core (Rods 5 & 6). This, as mentioned previously, justifies the structural C-Shaped bowing.

Taking a closer look at the load profiles with reference to the axial levels another conclusion can be drawn. Figure 49 shows the *absolute* magnitudes of the hydraulic loads. As mentioned above, the highest absolute loads occur at around 0.5 m and 4 m of height (the areas of the core with greatest instability and non-uniform flow). Meanwhile, towards the center of the core, flow stabilizes and has much lower transversal components. This exposes the fact that the central SGs (SG 4 & 5 & 6) have loads of higher magnitude acting upon them than the central Rods (Rods 4 & 5 & 6 & 7). Although the surface area of these SGs is much lower than the surface area of the Rods, SGs have a higher transversal loss coefficient (Subsection 3.2). Therefore, with flow having become rather constant in the middle of the core, SGs offer a higher resistance to the axial progress, causing a redistribution of the flow system close to the grids and incrementing the transversal local currents in the adjacent areas.

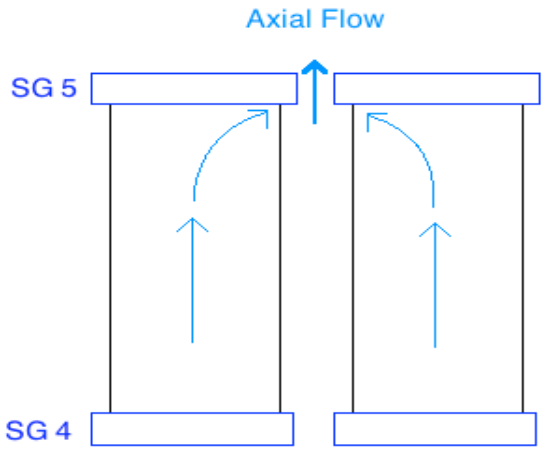

Figure 50: Flow redistribution to the gaps.

Figure 50 shows SGs number 4 & 5 of any two given FAs. The axial flow encounters higher resistance in the SGs and forces its way through the gaps, leading to local eddy currents and transversal load peaks in the grids.

Deviation of the transversal Hydraulic Loads

As a comparative force deviation analysis several approaches could be followed. To begin with the RMS Error (RMSE) is the fundamental measure of deviation. It directly quantifies the

similarity between two datasets (seen in Subsection 4.3). However, in cases of wide data ranges such as the Hydraulic Force Loads, the RMSD is most likely greatly affected by the width of the data range and hence, weakens the quality of the comparison and its relevance. The Quadratic Mean (QM) on the other hand does not aim at quantifying the exact similarity between two data sets. It represents the equivalent force throughout the domain that produces FA deformation.

$$Quadratic\ Mean\ = \sqrt{\frac{1}{N}\left(\sum_{i=1}^{N} X_i^2\right)}$$

Equation 22: Quadratic Mean. *(5-1)*

Considerable hydraulic load differences occur in the core when working with and without FSI. Therefore, using the RMSD approach as a reference to measure FSI effect may lead to wrong conclusions, as it takes into account all local force changes between the compared datasets. Local variations between the two datasets went up to a 202.6% of relative deviation in the most critical areas of the reactor (Appendix 7.3.1). Therefore, this Thesis used the approach of the QM in order to asses the global effect of the coupling on the FAs as a whole, trying to reduce the effect of local variations in the force distribution. "N" was set as the number of Fuel Assemblies (15) and for both the FSI and the No FSI the Quadratic Mean was calculated. Then the QM relative deviation was obtained by taking the No FSI dataset as the reference value and the FSI dataset as the observed value.

$$QM\ relative\ deviation\ [\%] = 100 * \frac{\sqrt{\frac{1}{N}\left(\sum_{i=1}^{N} X_{No\ FSI}^2\right)} - \sqrt{\frac{1}{N}\left(\sum_{i=1}^{N} X_{FSI}^2\right)}}{\sqrt{\frac{1}{N}\left(\sum_{i=1}^{N} X_{No\ FSI}^2\right)}}$$

Equation 23: Quadratic Mean Relative Deviation. *(5-2)*

QM of the transversal Hydraulic Loads

QM No FSI (N)	QM FSI (N)
6.818	7.739

QM Relative Deviaiton %	13.51

Table 6: QM & QM Relative Deviation (No FSI & FSI).

Having obtained a 13.5 % deviation between the two QMs, the influence of the FSI on the hydraulic loads could be assessed as strongly significant.

5.3.2 Displacement analysis

To complete the quantitative analysis a review of the effect of the FSI on the structural displacements was also done. An effective way of comparing the structural deformation was by studying the gap sizes between FAs and their change in magnitude. The initial dimensions of all the gaps in a non-deformed core were of 2 mm. This analysis, however, compared the End of Cycle gap dimensions of the FSI case with that of the No FSI case. In both of them the final

gap dimensions were expected to have experienced a given deformation, that is to say both cases would differ from the T0 gap sizes of 2 mm. Unlike in subsection 5.3.1 where the hydraulic loads of the No FSI case were the exact same at the EOC than at T0.

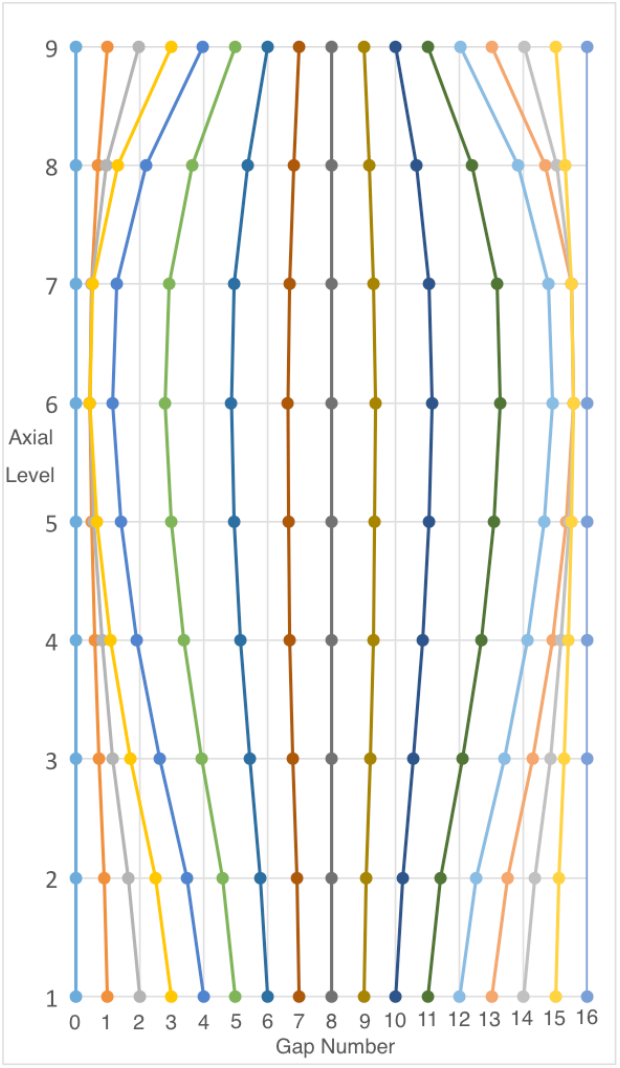

Figure 51: Gap deformation in the FSI Case at EOC.

Figure 51 represents the 16 Gaps separating the 15 FAs and their structural deformation pattern on each of the 9 axial levels for the FSI Case. Their separation of 2 mm has been subtracted and made dimensionless so that the change in magnitude and the global picture can be appreciated for the whole row. The structural pattern showing the C-Shaped bowing explained in Subsection 5.2 is, again, verified.

Meanwhile, Figure 52 shows the comparison between the differences in the structural displacements of the 15 FA at the 9 axial levels. The case in which the FSI displacement was higher than the No FSI displacement has been taken as positive. A higher difference in displacement can be observed at the top axial levels of the core, where the fluid flow caused greater deviations. This positive difference is, however not appreciated at the bottom of the core, where the differences in displacements are much smaller.

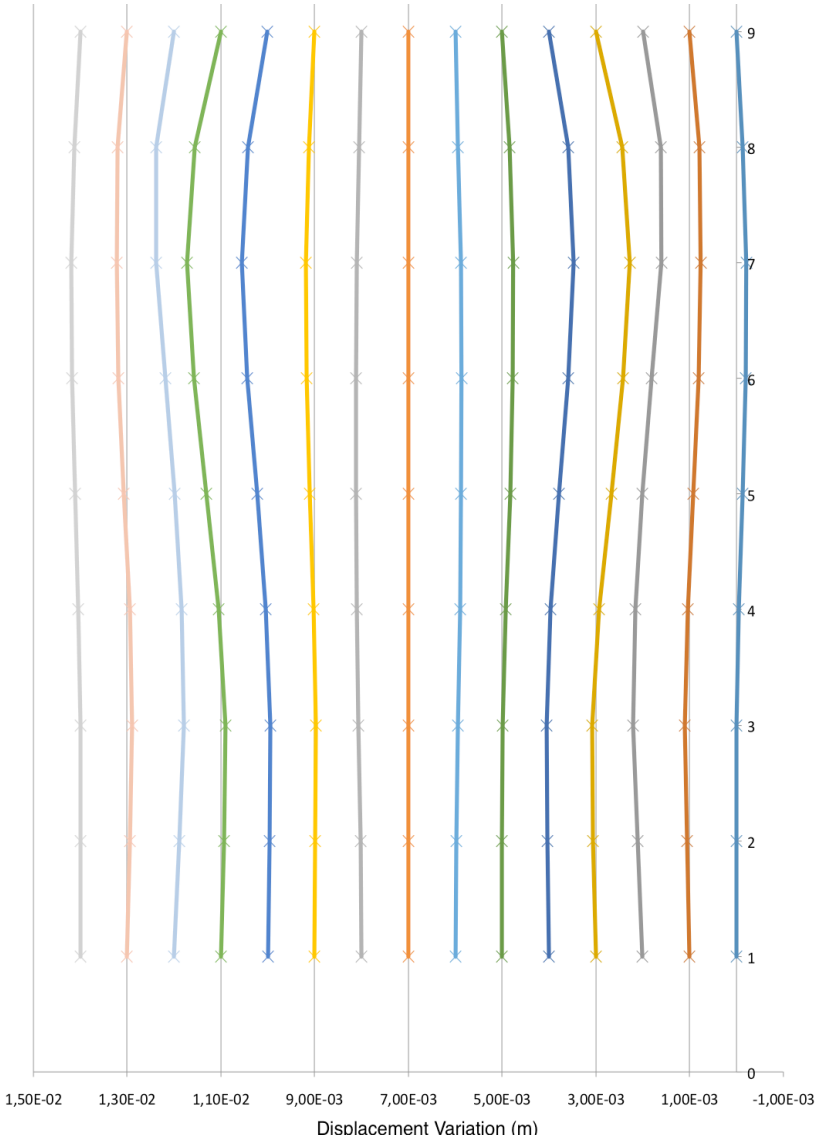

Figure 52: FSI vs. No FSI Displacement Differences.

To evaluate the deviations of the gap sizes with and without FSI only Axial Levels 2-7 were compared. Everything between SG 2 and SG 7, as SG 1 and SG 9 barely had any structural displacement. This would lead to more clear-cut results while at the same time maintaining a rigorous evaluation. This time, as the dataset range of the Gap size magnitudes was not so big, the Normalized Root Mean Square Deviation could be used without causing misleading conclusions. The No FSI case was taken as the reference value and the FSI case as the observed value and the same procedure as in Subsection 4.3 was followed.

Normalized RMSD of the Gap displacements

RMSD	Normalized Mean
1.42 E-4	2.28 E-3

Normalized RMSD (%)	6.22

Table 7: Normalized RMSD (No FSI & FSI).

QM of the Gap displacements

QM No FSI (m)	QM FSI (m)
2.287 E-3	2.316 E-3

QM Relative Deviation (%)	1.28

Table 8: Normalized QM (No FSI & FSI).

Table 7 shows, a Normalized RMSD of 6.22 % was obtained. It must be noted that, although far from the 13 % QM relative deviation of the Hydraulic Loads, a 6 % deviation in the structural results is also significant. In fact, the FSI effects were never expected to be as strong in the Structural as in the Hydraulic part of the coupling. The reasons for this are diverse. On one hand, the structural side had several time dependent factors influencing variability such as the creep law employed in the structural calculations, the growth during burn-up of the fuel etc. On the other hand, other variability factors such as the spring hold down forces also made the structural calculations more complex and, hence, diluted or partially hid the effect of the FSI on the structure. As seen in Table 8, the QM relative deviation of the structural results was, therefore, lower (1.28 % compared to the 6.22 % RMSD). Eliminating locality influence by using the QM matched the already coherent structural variation: the structure unlike the hydraulic loads was again proved to shift as a unit, relatively independent to local divergences.

6 Conclusions

The objective of this work was to implement a reliable Fluid Structure Interaction Interface to accurately predict and estimate the FA bow on a complete core level. The necessity for accurate FA Bow predictions arises from the safety and operational problems the phenomenon of Bowing can induce. With respect to the safety impact, deformation of the FA can interfere in the correct insertion and functionality of Control Rods. This, in turn, can lead to IRI episodes, which can jeopardize the safety of the nuclear power plant in the event of a Scram or a quick shutdown necessity. FA bow also induces performance problems by altering the coolant flow through the uneven FA structures and, hence, affecting the optimal Thermal Margins for operation. With the work of this Thesis a more accurate prediction of the magnitudes of the FA bowing dimensions was to be attained, enabling a better prevention of its negative effects.

Simulating the complete hydraulics and mechanics of a PWR reactor core would be too computationally expensive. This Thesis, instead, employed a porous model with loss coefficients of resulting similar characteristics to that of the real geometry.

To begin with, the simulation setup had to account for the geometrical dimensions and also for the given pressure losses that were to account for the real core geometry simulation. Next, the model implementation had to cover several issues. First was the structural displacement transfer strategy in which both Rod and SG displacements were mathematically calculated and incorporated to the code. These displacements then served as the base for the loss coefficient implementation (K values dropped to 0 in the areas of the core where the new deformed gaps lie). Second was the mesh displacement transfer strategy. The mesh displacement was done based on the outputs of the structural displacements and the accuracy of its simulated results was a great success. However, its computational cost was too high and this work had to discard further research within the field. Setting, nevertheless, a path for subsequent investigation.

The next step towards the implementation of the FSI was the coupling of the structural part to the hydraulic one. A weak two-way coupling was used: one where the fluid solution was dependent of the displacement interpolation, but where inner time-step convergence was not required. Finally, the Shell script coupling both simulation parts of the FSI Interface was carried out in a Linux environment.

All the results obtained and discussed in this work prove that the influence of a FSI Interface coupling is significant for the output of the FA Bow magnitudes.

On one hand, to evaluate the impact caused by the FSI Interface on the lateral hydrodynamic forces acting upon the FA structure, the Quadratic Mean (QM) approach was used as a reference for the deviation study. It was chosen as the best option as it is not influenced by the different local force distributions within the domain. The relative deviation of the QMs when comparing cases with and without FSI was 13.5 %. Although the porous model implementation contained uncertainty regarding its input parameters and initial assumptions (such as the inlet velocity profile), it was demonstrated that the lateral hydraulic force distribution is very sensible towards FSI.

On the other hand, to asess the impact caused by the FSI on the structural displacements, the normalized RMSD approach was used. A milder influence of the FSI was noticed than with the hydraulic part, around a 6 % deviation was appreciated. As explained in the results, the time dependency and the great amount of variability in the factors affecting the structural displacement side calculations partially diluted the effect of the FSI. The influence of the coupling on the structure, remains, however, unquestionable.

Having considered the weight and impact of the FSI coupling on the magnitudes of the FA bow dimensions, the question remains weather or not the considerable improvement on the veracity of the predictions is worth the additional computational expense it requires? Is the impact of the FSI coupling effect high enough as a post to the other great number of variability factors (velocity profiles, creep time dependent laws, hold down forces variation…)?

This Thesis sets the path for future research within the field of FSI couplings and for further work within the CFD of Nuclear Reactors. The possibility of reassessing the Mesh deformation and resetting parameters in order to obtain even more accurate results still lies open. While the performance of the CFD simulations in a 3-Dimensional representation of the Fuel Assembly row can also be a possible object of future study. Another topic that has also fallen out of the scope of this Thesis is the investigation of the quality of the used coupling scheme. The prospect of an in depth analysis of the sensitivity of results to the coupling time step as well as a comparison to a strong two-way coupling remain unexplored. Quite clearly, many opportunities still exist.

7 Appendix

7.1 Andreas Wanninger´s Structural Code Adaptation [15]

7.1.1 Definition of Grids, Rods, Axial Levels and Arrays

```
# State file created:  2015/05/15 18:09:41
# CFX-14.5 build 2012.09.19-21.47
!use Math::Trig;
!$numgrids=9;
!$numrods=$numgrids+1;
!$numFA=15;
!$numgaps=8;
!$numdisp=$numrods+1;
#! flag for switching on mesh deformation (0: no, 1: yes)
!$meshdef=0;
#!
# !define arrays which will collect strings with all locations for the respective boundary
!$fluidlocations="";
!$inletlocations="";
!$outletlocations="";
!$walllocations="";
!$ysymlocations="";
!$zsymlocations="";
!my @stepfunctionaxg=("") x $numgrids;
!my @stepfunctiontrg=("") x $numgrids;
!my @stepfunctionaxr=("") x $numrods;
!my @stepfunctiontrr=("") x $numrods;
#! Define axial levels array
!my @x_pos = (
!0.00000000e+0,
!1.40000004e-2,
!5.09999990e-2,
!5.59000015e-1,
!5.96000016e-1,
!1.10400009e+0,
!1.14100003e+0,
!1.64900005e+0,
!1.68599999e+0,
!2.19400001e+0,
!2.23100019e+0,
!2.73900008e+0,
!2.77600002e+0,
!3.28400016e+0,
!3.32100010e+0,
!3.82900023e+0,
!3.86600018e+0,
!4.37400007e+0,
!4.41100025e+0,
!4.50000000e+0);
!
#! Define FA "pitch"
!$pitch_FA=0.23;
!$gapsize=2e-3;
!
#!#! Define y positions array
!my @y_pos=[(0) x $numFA];
!#y position of 1st FA
!$y_pos[0]=-7*$pitch_FA;
#!corrected displacment for case when gap closes: not necessary for new model
!my @disp_corr_y= ([(0) x $numgaps], [(0) x $numdisp]);
!my @lowergrids= [(0) x ($numgrids+1)];
!my @uppergrids= [(0) x ($numgrids+1)];
!my @height= [(0) x ($numgrids+1)];
!my @gap= [(0) x (2*$numFA)];
!
```

7.1.2 Retrievement of APDL Results from csv Files

```
##########################################################
# Read APDL results from csv files
##########################################################
#!read gaps distances from APDL csv output file
!my $file = 'gaps_8.csv';
!my @gaps;
!open(my $fh, '<', $file) or die "Can't read file '$file' [$!]\n";
!while (my $line = <$fh>) {
!    chomp $line;
!    my @fields = split(/,/, $line);
#!    shift(@fields); #to remove the first number which is a line header
!    push @gaps, \@fields;
!}
#!just to check if file has been read correctly
!   open(my $out, '>', 'test1.txt') || die("Unable to open somefile.txt: $!");
!foreach my $row (@gaps) {
!    print $out join(",", @{$row}) . "\n";
!}
#!read displacements from APDL csv output file
!$file = 'displacementsy_8.csv';
!my @disp_y;
!open($fh, '<', $file) or die "Can't read file '$file' [$!]\n";
!while ($line = <$fh>) {
!    chomp $line;
!    my @fields = split(/,/, $line);
#!    shift(@fields); #to remove the first number which is a line header
!    push @disp_y, \@fields;
!}
#!just to check if file has been read correctly
!   open($out, '>', 'test2.txt') || die("Unable to open somefile.txt: $!");
!foreach my $row (@disp_y) {
!    print $out join(",", @{$row}) . "\n";
!}
#!read rotations from APDL csv output file
!$file = 'rotationsz_8.csv';
!my @rot_z;
!open($fh, '<', $file) or die "Can't read file '$file' [$!]\n";
!while ($line = <$fh>) {
!    chomp $line;
!    my @fields = split(/,/, $line);
#!    shift(@fields); #to remove the first number which is a line header
!    push @rot_z, \@fields;
!}
!#
```

7.1.3 Expressions Definition for Structural Displacements

```
105 ##################################################
106 # EXPRESSION DEFINITIONS FOR MESH DEFORMATION
107 ##################################################
108 !if ($meshdef == 1){
109
110     !for ($i=1;$i <= $numFA; $i++) {
111     !if ($i==1){
112     ! $gap[2*$i-2]=2*$gapsize;
113     ! $gap[2*$i-1]=$gapsize;
114     !}elsif($i==$numFA){
115     ! $gap[2*$i-2]=$gapsize;
116     ! $gap[2*$i-1]=2*$gapsize;
117     !}else {
118     ! $gap[2*$i-2]=$gapsize;
119     ! $gap[2*$i-1]=$gapsize;
120     !}
121     !$y_pos[$i-1]=$y_pos[0] + ($i-1) * $pitch_FA;
122  # Define expressions for grid levels
123     LIBRARY:
124     CEL:
125     EXPRESSIONS:
126     #left side addition, right side subtraction
127     # disp[0][x]=header
128     # disp[x][0]=displacement bottom of foot (=0)
129     # disp[x][1]=displacement top of foot
130     Displacement Grid $i 0 = 0 [m]
131     Displacement Grid $i 10 = 0 [m]
132     !$lowergrids[0] =0;
133     !$uppergrids[$numgrids] =0;
134     !for ($j=1;$j <= $numgrids; $j++) {
135         Displacement Grid $i $j = $disp_y[$i][$j+2] [m]  + tan( $rot_z[$i][$j+2])*
136         ( x / 1[m] - (($x_pos[$j+1]+$x_pos[$j])/2 )) [m]
137
138         !$lowergrids[$j] = $disp_y[$i][$j+2] + tan($rot_z[$i][$j+2])*
139         ($x_pos[2*$j]-($x_pos[2*$j]+$x_pos[2*$j-1])/2 );
140         !$uppergrids[$j-1] = $disp_y[$i][$j+2] - tan($rot_z[$i][$j+2])*
141         ($x_pos[2*$j]-($x_pos[2*$j]+$x_pos[2*$j-1])/2 );
142
143  #Stepfunction for axial grid
144  !$stepfunctionaxg[$j-1].="      step( y/1[m] - ( $y_pos[$i-1]-$pitch_FA/2
145  + $gap[2*$i-2]/2 + $disp_y[$i][$j+2]
146  + ( tan($rot_z[$i][$j+2]) * ( x/1[m] - (($x_pos[2*$j]+$x_pos[2*$j-1])/2) ) )))";
147
148  !$stepfunctionaxg[$j-1].="*step(($y_pos[$i-1]+$pitch_FA/2 - $gap[2*$i-1]/2
149  + $disp_y[$i][$j+2] + (tan( $rot_z[$i][$j+2])*
150  ( x / 1[m] - (($x_pos[2*$j]+$x_pos[2*$j-1])/2 ))))-y/1[m])+";
151
152  #Stepfunction for transversal grid
153  !$stepfunctiontrg[$j-1].="      step(y/1[m] - ( $y_pos[$i-1]-$pitch_FA/2
154  + $gap[2*$i-2]/2 + $disp_y[$i][$j+2]
155  + ( tan($rot_z[$i][$j+2])*( x / 1[m] - (($x_pos[2*$j]+$x_pos[2*$j-1])/2) ) )))";
156
157  !$stepfunctiontrg[$j-1].="*step(($y_pos[$i-1]+$pitch_FA/2 - $gap[2*$i-1]/2
158  + $disp_y[$i][$j+2]  + (tan( $rot_z[$i][$j+2])*
159  ( x / 1[m] - (($x_pos[2*$j]+$x_pos[2*$j-1])/2 )) ))-y/1[m])+";
160
161     !}
162     END
163     END
164     END
```

```
# Define expressions for rod bundles
   !for ($j=1;$j <= $numrods; $j++) {
   !$height[$j-1] = ($x_pos[2*($j-1)+1]-$x_pos[2*($j-1)]);
   LIBRARY:
   CEL:
   EXPRESSIONS:
   Displacement Rods $i $j  = $lowergrids[$j-1] [m] +
   (( x / 1[m] - $x_pos[2*($j-1)]) / $height[$j-1]) *
   ($uppergrids[$j-1] - $lowergrids[$j-1]) [m]

   Angle Rods $i $j = atan(( $disp_y[$i][$j+2] - $disp_y[$i][$j+1] )
   /($x_pos[2*$j-1] - $x_pos[2*$j-2]))

   AngleofAttack $i $j = abs( asin(Velocity v /VelocityFree) - Angle Rods $i $j)

   CorrectionFactor $i $j = 6*abs(sin(AngleofAttack $i $j))^1.7/
   (cos((pi/2-AngleofAttack $i $j)/2)^1.7)

   KLossCrossFlow $i $j = FrictionFactorPeybernes *
   CorrectionFactor $i $j *PorosityCore^2 *
   PitchToDiameter^2 / (Pitch * ( PitchToDiameter-1)^2 )/ PorosityCore^2

  #Stepfunction for axial rod
  !$stepfunctionaxr[$j-1].="step(y/1[m]-($y_pos[$i-1]- $pitch_FA/2
  + $gap[2*$i-2]/2 + ($lowergrids[$j-1] + (( x / 1[m] - $x_pos[2*($j-1)]) / $height[$j-1])
  * ($uppergrids[$j-1] - $lowergrids[$j-1]))  ))";

  !$stepfunctionaxr[$j-1].="*step( ($y_pos[$i-1]+ $pitch_FA/2 - $gap[2*$i-1]/2 +
  ($lowergrids[$j-1] + (( x / 1[m] - $x_pos[2*($j-1)]) / $height[$j-1]) *
  ($uppergrids[$j-1] - $lowergrids[$j-1]))  ) -y/1[m])+";


  #Stepfunction for transversal rod
  !$stepfunctiontrr[$j-1].="step(y/1[m]-($y_pos[$i-1]-$pitch_FA/2 +  $gap[2*$i-2]/2 +
  ($lowergrids[$j-1] + (( x / 1[m] - $x_pos[2*($j-1)]) / $height[$j-1]) *
  ($uppergrids[$j-1] - $lowergrids[$j-1]))  ))";

  !$stepfunctiontrr[$j-1].="*step( ($y_pos[$i-1]+ $pitch_FA/2 - $gap[2*$i-1]/2 +
  ($lowergrids[$j-1] + (( x / 1[m] - $x_pos[2*($j-1)]) / $height[$j-1]) *
  ($uppergrids[$j-1] - $lowergrids[$j-1]))  ) -y/1[m])+";


    END
    END
    END
   !}
   !}
   !for ($j=1;$j <= $numgrids; $j++) {
   # Remove last + from string
   !chop($stepfunctionaxg[$j-1]);
   !chop($stepfunctiontrg[$j-1]);
   LIBRARY:
   CEL:
   EXPRESSIONS:
   KLossGridAxialStep $j= KLossGridAxial * ( $stepfunctionaxg[$j-1] )
   KLossGridLateralStep $j = KLossGridLateral * ( $stepfunctiontrg[$j-1] )
   END
   END
   END
   !}
```

```
#MeshDeformation

#Mesh Grid Deformation

    !for ($j=1;$j <= $numgrids; $j++) {

    LIBRARY:
    CEL:
    EXPRESSIONS:

        !for ($i=2;$i <= $numFA; $i++) {
            !$iminus=$i-1;

            MeshDefGrids $i $j = (Displacement Grid $iminus $j + Displacement Grid $i $j )/2
        !}
        !for ($i=1;$i <= $numFA; $i++) {
            !$iplus=$i+1;
            MeshDefGrids 1 $j = 0
            MeshDefGrids 16 $j = 0

            InterpolationMeshGrids $i $j = MeshDefGrids $i $j [m] +
            (((MeshDefGrids $iplus $j - MeshDefGrids $i $j)/$pitch_FA) *
            (y / 1[m] - ($y_pos[$i-1] - $pitch_FA/2)))
        !}
    END
    END
    END
    !}

#Mesh Rod Deformation

    !for ($j=1;$j <= $numrods; $j++) {

    LIBRARY:
    CEL:
    EXPRESSIONS:

        !for ($i=2;$i <= $numFA; $i++) {
            !$iminus=$i-1;

            MeshDefRods $i $j = (Displacement Rods $iminus $j + Displacement Rods $i $j)/2
        !}
        !for ($i=1;$i <= $numFA; $i++) {
            !$iplus=$i+1;
            MeshDefRods 1 $j = 0
            MeshDefRods 16 $j = 0

            InterpolationMeshRods $i $j = MeshDefRods $i $j [m]  +
            (((MeshDefRods $iplus  $j - MeshDefRods $i $j)/$pitch_FA) *
            (y / 1[m] - ($y_pos[$i-1] - $pitch_FA/2)))
        !}
    END
    END
    END
    !}
```

7.1.4 Root Mean Square Absolute Deviation Mesh Analysis

Absolute Deviations of the axial forces X (19 axial levels)

RMS Deviations (N)																		
Rods 1	SG1	Rods 2	SG2	Rods 3	SG3	Rods 4	SG4	Rods 5	SG5	Rods 6	SG6	Rods 7	SG7	Rods 8	SG8	Rods 9	SG9	Rods 10
0.02	0.01	0.22	0.46	0.58	0.62	0.60	0.65	0.36	0.54	0.65	1.46	0.92	1.38	0.85	0.53	0.39	0.03	0.10

Table 9: Deviation of the axial forces from Deformed to Non-deformed Mesh (2 d.p.).

Absolute Deviations of the transversal forces Y (19 axial levels)

RMS Deviations (N)																		
Rods 1	SG1	Rods 2	SG2	Rods 3	SG3	Rods 4	SG4	Rods 5	SG5	Rods 6	SG6	Rods 7	SG7	Rods 8	SG8	Rods 9	SG9	Rods 10
0.01	0.02	0.24	0.37	0.07	0.24	0.16	0.68	0.14	0.47	0.08	0.39	0.27	0.47	0.14	0.15	0.14	0.09	0.04

Table 10: Deviation of the transversal forces from Deformed to Non-deformed Mesh (2 d.p.).

7.1.5 Retrievement of CFX Results (Hydraulic Loads)

```
# State file created:  2015/05/15 18:09:41
# CFX-14.5 build 2012.09.19-21.47
COMMAND FILE:
  CFX Post Version = 14.5
END
    !$numgrids=9;
    !$numrods=$numgrids+1;
    !$numFA=15;
    !$numgaps=16;
    !$numaxpos=$numgrids+$numrods;
    !$porosity=0.556;
    !$factor3D=2.3;     #factor to account for real depth of FA vs mesh depth of 0.1m
    # CREATE 2D ARRAYS FOR FROCES (FA IN ROWS, AXIAL POSITIONS IN COLUMNS) #####
    !my @force_x = ([(0) x $numFA], [(0) x $numaxpos]);
    !my @force_y = ([(0) x $numFA], [(0) x $numaxpos]);
    ##############################################
    # LOOP OVER FAs ##############################
    ##############################################
    !for ($i=0;$i <= $numFA-1; $i++) {
      !if ($i==0){
      ! $i2= "";
      !}else{
      ! $i2= $i+1;
      !}
     # LOOP OVER AXIAL ROD LOCATIONS ##############
     !for ($j=1;$j <= $numrods; $j++) {
       # the first FA is given no number (""), the others are numbered as $i (starting from 2)
        !$rodsxplus="RODS2DXPLUS $j $i2";
        !$rodsxminus="RODS2DXMINUS $j $i2";
        !$rodsyplus="RODS2DYPLUS $j $i2";
        !$rodsyminus="RODS2DYMINUS $j $i2";
        !$rodszplus="RODS2DZPLUS $j $i2";
        !$rodszminus="RODS2DZMINUS $j $i2";
      !if ($i==0){
      #remove last blank to avoid error
        !chop($rodsxplus);
        !chop($rodsxminus);
        !chop($rodsyplus);
        !chop($rodsyminus);
        !chop($rodszplus);
        !chop($rodszminus);
      !}
     # SUM UP X- AND Y- FORCES FOR RODS ######################
     !$force_x[$i][2*$j-2]=-(force($rodsxplus,"x") + force($rodsxminus,"x")
     !+ force($rodsyplus,"x") + force($rodsyminus,"x")
     !+ force($rodszplus,"x") + force($rodszminus,"x"))*$factor3D*$porosity;    #multiply with real depth and porosity
     !$force_y[$i][2*$j-2]=-(force($rodsxplus,"y") + force($rodsxminus,"y")
     !+ force($rodsyplus,"y") + force($rodsyminus,"y")
     !+ force($rodszplus,"y") + force($rodszminus,"y"))*$factor3D;      #multiply with real depth
     !}
     # LOOP OVER AXIAL GRID LOCATIONS ########################
     !for ($j=1;$j <= $numgrids; $j++) {
     # the first gap is given no number (""), the others are numbered as $i (starting from 2)
        !$gridxplus="GRID2DXPLUS $j $i2";
        !$gridxminus="GRID2DXMINUS $j $i2";
        !$gridyplus="GRID2DYPLUS $j $i2";
        !$gridyminus="GRID2DYMINUS $j $i2";
        !$gridzplus="GRID2DZPLUS $j $i2";
        !$gridzminus="GRID2DZMINUS $j $i2";
      !if ($i==0){
```

```
61          #remove last blank to avoid error
62            !chop($gridxplus);
63            !chop($gridxminus);
64            !chop($gridyplus);
65            !chop($gridyminus);
66            !chop($gridzplus);
67            !chop($gridzminus);
68          !}
69        # SUM UP X- AND Y- FORCES FOR GRIDS ####################
70        !$force_x[$i][2*$j-1]=-(force($gridxplus,"x") + force($gridxminus,"x")
71        !+ force($gridyplus,"x") + force($gridyminus,"x")
72        !+ force($gridzplus,"x") + force($gridzminus,"x"))*$factor3D*$porosity;
73        !$force_y[$i][2*$j-1]=-(force($gridxplus,"y") + force($gridxminus,"y")
74        !+ force($gridyplus,"y") + force($gridyminus,"y")
75        !+ force($gridzplus,"y") + force($gridzminus,"y"))*$factor3D;
76      !}
77      !}
78      # PRINT FORCES INTO FILE 'FORCES.TXT' ####################
79      !   open(my $out, '>', 'forcesx.csv') || die("Unable to open somefile.txt: $!");
80  #   !   print $out " forces x:\n";
81      !foreach my $row (@force_x) {
82      !    print $out join(",", @{$row}) . "\n";
83      !}
84      !close($out);
85      !   open($out, '>', 'forcesy.csv') || die("Unable to open somefile.txt: $!");
86  #   !   print $out "\n forces y:\n";
87      !foreach $row (@force_y) {
88      !    print $out join(",", @{$row}) . "\n";
89      !}
90      !close($out);
```

7.2 FSI Interface Looping - Bash Code

```
#!/bin/bash

#[ -z $1 ] && echo "Usage: sendjob.sh <Work Path>" && exit 1

#[ ! -d $1 ] && echo "Specified work directory does not exist!" && exit 2
. /etc/profile
#cd $1
export WorkPATH=$(pwd)
export jobName=$(basename $WorkPATH)
mkdir -p output
mkdir -p outcsv
# shared memory job on uv2, 16 cores are to be used
export cpus=2
export ANS_USER_PATH=/home/hpc/pr58ca/di72bec/work/ANSYSmech/BeamModel/FA_Models_1/Model1/InputFiles/UserMatLib
export ANS_COMPILER_PATH="/lrz/sys/intel/compiler/composer_xe_2015.5.223/bin/intel64/ifort"

#remove previou output (insert check before!!)
#rm $jobName.stdout
#rm $jobName.r??[0-9]

#echo "Check for parallel ..." application

echo "Write Job script ..."

cat > job.sh << EOT1
#!/bin/bash

#SBATCH -o $WorkPATH/output/$(basename $WorkPATH).%j.%N..out
#SBATCH -D $WorkPATH
#SBATCH -J $(basename $WorkPATH)
#SBATCH --get-user-env
##
##Options for serial job
#SBATCH --clusters=serial
#SBATCH --partition=serial_mpp2
##
##Options for OpenMP job
##SBATCH --clusters=mpp2
##SBATCH --nodes=1-1
##SBATCH --cpus-per-task=$cpus
##
##Options for MPI jobs
##SBATCH --clusters=mpp1
##SBATCH --ntasks=$cpus
##
#SBATCH --mail-type=end
#SBATCH --mail-user=andreas.wanninger@ntech.mw.tum.de
#SBATCH --export=NONE
#SBATCH --time=01:00:00

export OMP_NUM_THREADS=$cpus

. /etc/profile
source /etc/profile.d/modules.sh

module load ansys/16.0
module load cfx/16.0
# link user library directory
export ANS_USER_PATH=/home/hpc/pr58ca/di72bec/work/ANSYSmech/BeamModel/FA_Models_1/Model1/InputFiles/UserMatLib
export ANS_COMPILER_PATH="/lrz/sys/intel/compiler/composer_xe_2015.5.223/bin/intel64/ifort"
```

```
cd  $WorkPATH

((t_end=7920+1))
#dt1='`echo "scale=4;10^-3" | bc`'  #definening floating point number in shell script
dt1=1
dt2=1000
t_ls_ini=\$dt1 #\$dt+100    !time at end of load step
restar=0
creep=0
gridcreep=0
swell=1
flow=1
grad=0
let tcheck=\$t_end-\$dt2
t_ls=\$t_ls_ini
inisflag=0          #0: do nothing, 1: write, 2: read
ls_count=0
n_cycle=1
n_fa=1

for ((n=1;n<=n_cycle;n++))  #loop over cycles
do

## initial steps before reactor operation
for (( k=4; k<=4; k+=3))
#for k in {1..4}
do

#set holddown case
hdcase=5 #\$k

if (( ls_count > 1 ))
then
    restar=1
    flow=1
#    creep=1
#    inisflag=2
   inisflag=0
   ((ls_remove=ls_count-1))
#   rm $jobName.r*\$ls_remove   #remove previous restart file to save disk space
#else
#   inisflag=2
fi

cat > ScriptVariables.parm << EOT2
/NOPR
*SET,JOBNAME ,'$jobName'
*SET,T_END , \$t_end
*SET,HDCASE,\$hdcase
*SET,T_LS , \$t_ls
*SET,DT, \$dt1
*SET,CREEP, \$creep
*SET,GRIDCREEP, \$gridcreep
*SET,RESTAR, \$restar
*SET,SWELL, \$swell
*SET,INISFLAG,\$inisflag
*SET,FLOW, \$flow
*SET,GRAD, \$grad
*SET,LS_COUNT,\$ls_count
*SET,N_FA,\$n_fa
*SET,_RETURN ,  0.000000000000
```

```
*SET,_STATUS ,  1.000000000000
/GO

EOT2

##Load Cfx Mesh and run the session##

cfx5pre -batch $(basename *.pre) $(basename *.cfx)

##Run the solver with the .def file and obtain a result file##

cfx5solve -def $(basename *.def) -chdir $WorkPATH -name $(basename *.def .def)

##Run the .cse session to extract the hydraulic loads from the results and later erase the result file##

cfx5post -batch $(basename *.cse) $(basename *.res)

rm -f $(basename *.res)

##Parallel OpenMP
##"/lrz/mnt/sys.x86_64/applications/ansys/v160/ansys/bin/ansys160"
-b -p aa_r -np $cpus -dir $WorkPATH -j $jobName -s read -l en-us -t -d X11 -i "MainInput.inp"
-JOBNAME $jobName -restar \$restar| tee -i -a "$jobName.stdout"
##Serial
"/lrz/mnt/sys.x86_64/applications/ansys/v160/ansys/bin/ansys160"
-b -p aa_r -dir $WorkPATH -j $jobName -s read -l en-us -t -d X11 -i "MainInput.inp"
-JOBNAME $jobName -restar \$restar| tee -i -a "$jobName.stdout"

#remove previous restart file and how?


#t_ls=`echo "scale=4;\$t_ls+\$dt1" | bc`
#increment load step time, floating point arithmetics necessary (equivalent to: let t_ls=\$t_ls+\$dt1)
((t_ls += dt1))
#increment load step time, floating point arithmetics necessary (equivalent to: let t_ls=\$t_ls+\$dt1)
((ls_count++))          #increment load step nember

done


#set load step time to size of dt2
((t_ls = dt2 + t_ls_ini))
#active creep, grid gridcreep and growth
creep=1
gridcreep=0
swell=1
flow=1
grad=1
restar=1
restarstep=$ls_count
hdcase=5

while [ \$t_ls -le \$t_end ]
do

cat > ScriptVariables.parm << EOT
/NOPR
*SET,JOBNAME ,'$jobName'
*SET,T_END , \$t_end
*SET,HDCASE,\$hdcase
```

```
*SET,HDCASE,\$hdcase
*SET,T_LS , \$t_ls
*SET,DT, \$dt2
*SET,CREEP, \$creep
*SET,GRIDCREEP, \$gridcreep
*SET,RESTAR, \$restar
*SET,RESTARSTEP, \$restarstep
*SET,SWELL, \$swell
*SET,FLOW, \$flow
*SET,GRAD, \$grad
*SET,LS_COUNT,\$ls_count
*SET,_RETURN ,  0.000000000000
*SET,_STATUS ,  1.000000000000
/GO

EOT

##Load Cfx Mesh and run the session##

cfx5pre -batch $(basename *.pre) $(basename *.cfx)

##Run the solver with the .def file and obtain a result file##

cfx5solve -def $(basename *.def)

##Run the .cse session to extract the hydraulic loads from the results and later erase the result file##

cfx5post -batch $(basename *.cse) $(basename *.res)

rm -f $(basename *.res)

##Parallel OpenMP
##"/lrz/mnt/sys.x86_64/applications/ansys/v160/ansys/bin/ansys160"
-b -p aa_r -np $cpus -dir $WorkPATH -j $jobName -s read -l en-us -t -d X11 -i
"MainInput.inp" -JOBNAME $jobName -restar \$restar| tee -i -a "$jobName.stdout"
##Serial
"/lrz/mnt/sys.x86_64/applications/ansys/v160/ansys/bin/ansys160"
-b -p aa_r -dir $WorkPATH -j $jobName -s read -l en-us -t -d X11 -i
"MainInput.inp" -JOBNAME $jobName -restar \$restar| tee -i -a "$jobName.stdout"

#increase load step time while making sure last load step time equals end time
if [ \$t_ls -gt \$tcheck -a \$t_ls -lt \$t_end ]
then t_ls=\$t_end
else
((t_ls += dt2))         #increment load step time (equivalent to: let t_ls=\$t_ls+\$dt1)
fi

((ls_count++))          #increment load step nember

echo \$t_ls
done

set load step time to size of dt2
t_ls=`echo "scale=4;\$t_end+\$dt1" | bc`
#increment load step time, floating point arithmetics necessary (equivalent to: let t_ls=\$t_ls+\$dt1)
t_ls=\$(( t_end + dt1 ))
#inactive creep, grid gridcreep and growth
creep=0
grad=0
gridcreep=0
#swell=0
```

```
flow=0
restar=1

#for (( k=4; k<=4; k+=3))
#do
#
##set holddown case
#let hdcase=5-\$k
#
##last run: save inistate
#if [ \$k -eq 1 ]
#then
#inisflag=0 #1
#else
#inisflag=0
#fi
#
#cat > ScriptVariables.parm << EOT2
#/NOPR
#*SET,JOBNAME ,'\$jobName'
#*SET,T_END ,\$t_end        !t_ls is now automatically t_end
#*SET,HDCASE,\$hdcase
#*SET,T_LS ,\$t_ls
#*SET,DT, \$dt1
#*SET,RESTAR, \$restar
#*SET,SWELL, \$swell
#*SET,INISFLAG,\$inisflag
#*SET,FLOW, \$flow
#*SET,GRAD, \$grad
#*SET,LS_COUNT,\$ls_count
#*SET,_RETURN ,  0.000000000000
#*SET,_STATUS ,  1.000000000000
#/GO
#
#EOT2
#
#"/lrz/mnt/sys.x86_64/applications/ansys/v160/ansys/bin/ansys160"
-b -p aa_r -np $cpus -dir $WorkPATH -j $jobName -s read -l en-us -t -d X11 -i
"MainInput.inp" -JOBNAME $jobName -restar \$restar| tee -i -a "$jobName.stdout"
#
##t_ls=`echo "scale=4;\$t_ls+\$dt1" | bc`
#increment load step time, floating point arithmetics necessary (equivalent to: let t_ls=\$t_ls+\$dt1)
#((t_ls += dt1))            #increment load step time (equivalent to: let t_ls=$t_ls+\$dt1)
#((ls_count++))         #increment load step nember
#
#done       #done end-of-cycle loop

done        #done loop over cycles

EOT1
#exit 1

echo "Submit Job ..."

chmod 744 job.sh

#./job.sh > FSI.out &
sbatch job.sh

```

7.3 Results: FSI Vs. No FSI Analysis

7.3.1 Hydraulic Loads

Relative Local Deviations of the transversal forces Y as a % (19 axial levels & 15 FA)

Relative Local Deviations																		
Rods 1	SG1	Rods 2	SG2	Rods 3	SG3	Rods 4	SG4	Rods 5	SG5	Rods 6	SG6	Rods 7	SG7	Rods 8	SG8	Rods 9	SG9	Rods 10
2,5	1,9	17,2	40,5	18,0	8,3	42,9	50,5	3,8	13,5	0,3	11,9	2,5	12,4	13,9	0,3	16,3	11,8	9,6
8,2	7,3	17,9	27,0	31,8	22,1	4,1	55,6	74,7	202,6	47,8	49,3	47,6	25,6	39,0	13,2	27,0	4,8	14,5
12,6	10,9	20,9	8,7	34,5	9,2	50,8	41,3	27,2	150,1	14,3	6,4	50,2	29,9	43,2	1,8	43,8	11,7	27,5
15,1	13,1	20,9	8,7	43,1	59,9	38,0	22,2	58,0	111,5	16,1	13,9	58,2	23,9	66,9	7,8	49,7	13,2	38,3
15,2	12,4	21,2	30,2	26,8	41,1	54,2	114,3	52,4	75,6	6,2	26,7	57,1	10,6	76,9	66,3	38,1	3,4	32,8
11,3	7,6	2,1	48,5	42,7	62,4	5,0	71,1	22,5	12,9	3,6	36,5	55,9	44,4	22,3	48,3	19,9	0,2	21,1
7,6	3,6	2,7	3,4	20,3	98,5	39,1	29,2	32,3	0,6	6,6	16,2	64,2	45,8	45,6	63,4	21,9	33,8	21,5
Central FA 8 (values approximately 0)																		
13,2	3,2	0,3	1,9	18,6	93,8	37,4	33,4	30,0	1,7	78,7	184,6	82,4	74,8	44,3	63,2	22,4	34,6	50,2
9,0	7,6	1,0	47,1	40,8	62,2	0,8	57,8	28,2	8,6	6,9	29,3	58,9	43,7	22,5	49,6	19,2	3,0	36,8
16,6	12,5	21,8	32,2	25,6	44,8	56,5	105,4	52,4	74,9	8,3	28,0	55,2	10,7	76,4	69,5	39,6	6,4	38,2
14,9	13,3	21,3	7,3	44,8	62,9	36,7	21,9	58,3	111,7	17,3	15,2	57,2	23,1	67,8	6,9	50,2	12,5	40,7
12,7	11,0	21,0	8,6	34,8	10,2	50,0	41,7	27,6	148,5	15,3	6,5	53,7	30,3	42,6	0,6	43,2	10,8	29,2
8,2	7,2	17,9	27,0	31,8	22,1	3,6	55,5	76,2	202,5	43,3	48,3	47,0	25,4	39,3	13,0	26,9	4,8	14,4
2,7	2,0	17,9	40,5	20,5	8,4	46,6	50,5	3,2	13,3	6,5	12,2	7,2	12,5	12,1	0,3	15,8	11,8	9,7

Table 11: Relative Local Deviations of the Transversal Forces (%).

Bibliogrpahy

[1] Markmann, K.: Copenhagen Accord pledge. Nature 464 (2010) 7292, p. 1126-1128.

[2] Flowserve: ABWR power tests simulation by using a dual RELAP5 nuclear power plant simulation platform. Nuclear Engineering and Design 249 (2012) p. 41-48.

[3] Macian, R.: Grundlagen der Thermal Hydraulik in Nuklearsystemen. 1 (2014) p. 245.

[4] Andersson, T.: A decade of assembly bow management at Ringhals. In: Structural Behaviour of Fuel Assemblies for Water Cooled Reactors: Proceedings of a Technical Meeting Held in Cadarache, France, 22-26 November 2004, 2005. International Atomic Energy Agency p. 129. ISBN: 9201051050.

[5] Levasseur, B.: 3-D Modeling of Fuel Assemblies Growth and Bow for EDF PWRs. (2009)

[6] Horváth, Á.: On numerical simulation of fuel assembly bow in pressurized water reactors. Nuclear Engineering and Design 265 (2013) p. 814-825.

[7] Peybernès, J.: Evaluation of the forces generated by cross-flow on PWR fuel assembly. IAEA-TECDO 1454 (2005) p. 13

[8] Bieder, U.: CFD ANALYSIS OF NON-AXIAL FLOW IN FUEL ASSEMBLIES. (2009)

[9] Wanninger, A.: PHD. (2015)

[10] Stabel, J.: Fuel assembly bow: Analytical modeling and resulting design improvements. In: Transactions of the 13. International Conference on Structural Mechanics in Reactor Technology. v. 1, 1995.

[11] Lascar, C.: AREVA NP's advanced thermal hydraulic methods for reactor core and fuel assembly design. (2009)

[12] Dr. Ing. Cabrera Rochera, E. / Department of Engineering Hydraulics & Water Treatments of the ETSII at the UPV / *Introduction to Fluid Dynamics,* Vol. 4.

[13] Komar, A.: Covariant conservation laws in general relativity. Physical Review 113 (1959) 3, p. 934.

[14] Nield, D.: Mechanics of Fluid Flow Through a Porous Medium. Springer 2013. ISBN: 1461455405.

[15] Ryskamp, J. M.: Depletion analysis of mixed-oxide fuel pins in light water reactors and the advanced test reactor. Nuclear technology 129 (2000) 3, p. 326-337.

[16] Chelbi, M.: Bachelor Thesis: Construction of a 2D CFD Model for the Analysis of Steady-state Axial and Lateral Hydraulic Forces in a PWR Reactor Core Based on a Porous Me- dium Approach. (2015)

[17] O. C. Zienkiewicz and R. L. Taylor, *The Finite Element Method*, vol. 1, Butterworth-Heinemann, 5th edition, 2000.

[18] Nield, D.: Mechanics of Fluid Flow Through a Porous Medium. Springer 2013. ISBN: 1461455405.

THESIS BUDGET

1 Introduction

The following section has the objective of carrying out an economic analysis of the costs allocated to this Master Thesis. To do this, it is necessary to evaluate both the equipment used and the wearing down of this equipment. The manpower employed to carry out and simulate the work and its posterior analysis, will also be estimated.

There will, therefore, be four subsections to the Thesis Budget: budget of the workforce, budget of the equipment, budget of the tangible assets used and budget of the LRZ Cluster usage-to-expenditure ratio.

1.1 Workforce

There were two significant contributors in the completion of this Thesis:

1) The TUM Mechanical Engineering and Management master student, dedicated full-time to the research project for a 7 month period.
2) The TUM Dipl. Ing. researcher from the Lehrstuhl für Nukleartechnik, dedicating a 10% of his total active hours to the mentoring and assistance of the Master´s student.

1.2 Equipment

With respect to the equipment used there are also two main areas to consider:

1) The physical equipment used (hardware).
2) The programmes used for simulation and analysis (software).

To properly allocate the cost of the equipment on the completion of the Thesis, it is necessary to take into account both the amortization and the useful lifespan or operating life of the apparatus used. The amortization cost can be calculated by:

$$A = \frac{C \cdot t \cdot n}{T}$$

with:

C: acquisition cost of the equipment (EUR).

n: usage level of the equipment.

t: usage time of the equipment for this project.

T: total operating life of the equipment.

1.3 Tangible assets

Tangible assets are those consumed during the execution of this project. This refers to all the material that, once used during the course of the thesis, will be considered as worn-out and no longer be employed. In this field there is mainly office material such as pens, notebooks, staples etc.

The sum of the tangibles is only mildly relevant for this project and they are, therefore, considered as a whole.

1.4 LRZ TUM / LMU Cluster

One last relevant factor to consider for the budget calculation is the cost of the LRZ cluster simulation hours. Both of the universities in Munich, the TUM and the LMU, use a common high-speed cloud cluster to assist their research projects and save simulation time in their execution.

To access the cluster each individual Chair of the TUM has a set number of monthly hours that it has to administrate. The cost for the upload and usage of 1 simulation hour is confidential material, but after contacting the TUM “Abteilung für technischer Support und Diensteilung” (technical support department of the TUM) an approximated amount of 0,45 EUR/hour was established for the CPU processing level employed (level 2).

2 Budget

In the following section the breakdown and explanation of the costs associated to each of the 4 subsections of the budget will be done.

2.1 Workforce

To determine the cost of the workforce the two mentioned contributors have to be catalogued by their degree and status.

The two contributors are, therefore, a Graduate Mechanical engineer working under the HIWI programme of the TUM (programme offered by the university for student insertion into the working world) and a Senior Mechanical engineer with a PHD highered by the Nuchlear Energy Department. The working conditions in Germany imply the following:

- They will both receive 12 salaries per year.
- They will have 30 vacation days per year.
- The minimum contribution base in Germany is of 1067,4 EUR/month.
- Contribution for contingencies for the Department of Nuclear Energy:
    - Common contingencies & insurance 23,6%.
    - Unemployment 5,5%.
    - Training 0,6%
- Rentenversicherung (equivalent to the IRPF) of 20%.
- Diets of 4 EUR/day for a total of 140 working days.
- A Graduate Mechanical engineer under the HIWI programme will have a net salary of 800 EUR/month.
- A Senior Mechanical engineer in Germany will have a net salary of 2800 EUR/month.

First, to account for the number of total hours:

	Monthly working Hours	Number of Months	Dedication	Total Hours
Graduate engineer	160	7	100%	1120
Senior engineer	160	7	10%	112

Budget Table 1: Total workforce hours.

Now the cost for the Department of Nuclear energy of the Graduate engineer under the HIWI programme:

Concept	Units	Amount
Net Salary	Euros/unit	800
Common Contingencies	Euros/unit	188,8
Unemployment	Euros/unit	44
Training	Euros/unit	4,8
Rentenversicherung (Exempt)	Euros/unit	0
Diets	Euros/unit	560
Gross Salary (monthly)	Euros/unit	1037,6
Gross Salary (7 month period)	**Euros/year**	**7823,2**

Budget Table 2: Cost of the Graduate engineer.

The cost of the Senior engineer with a 10% dedication for the Department:

Concept	Units	Amount
Net Salary	Euros/unit	2800
Common Contingencies	Euros/unit	660,8
Unemployment	Euros/unit	154
Training	Euros/unit	16,8
Rentenversicherung	Euros/unit	560
Diets	Euros/unit	560
Gross Salary (monthly)	Euros/unit	4191,6
Gross Salary (7 month period)	Euros/year	29901,2
Gross expenditure with 10% Dedication	**Euros/year**	**2990,12**

Budget Table 3: Cost of the Senior engineer.

Therefore, the final cost of the workforce results in:

Contributor	Units	Amount
Graduate engineer	Euros/hour	**6,99**
Senior engineer	Euros/hour	**26,70**

Budget Table 4: Hourly cost of workforce.

2.2 Equipment

Calculating the amortization cost of the main equipment involved, as explained in the previous subsection, the result is:

Equipment	Cost of aquisition (EUR/unit)	Useful Lifetime (years)	Usage Time (h)	Usage Level	Cost (EUR)
PC - HP Z440	1886,39	4	900	100%	221,06
ANSYS CFX Software - 1 license	1556,9	2	600	75%	182,45
				Total	**403,51**

2.3 Tangible Assets

As the tangible assets are not of great relevance for the scope of this budget, they are all included into one main cost.

Material	Cost of aquisition (EUR/unit)	Cost (EUR)
Tangible Assets	40	40,00
	Total	**40,00**

2.4 LRZ TUM/LMU Cluster

As explained in subsection 1.4 of the Budget, the final CFX and Bash Loop simulations of this Thesis were carried out and supported by Munich´s LRZ combined TUM and LMU Cluster.

Having obtained an approximated cost of the CPU processing level used (level 2), the expense of the total Thesis simulation could be calculated.

Towards the end of the Thesis, once the FSI had been successfully set up a total of 9 simulations were necessary (including the trial one).

As explained in subsection 4.4.3 of the Thesis Report, the operation of a Nuclear power plants is divided into cycles. Each cycle usually lasts between 12-18 months having an outage for refueling and for security measures verification. The usual PWR operates 24 hours a day and has around 35 days of refueling outage time per year. This results in 7924 operational hours per cycle (assuming a 12 month cycle).

In real time, 8-22 hours of simulation in the LRZ cluster environment would account for these 7924 hour cycles of the reactor. After the trial and initial simulation, convergent results were reached in simulations 7&8., hence setting the endpoint of the computational expenses.

Concept	Units	Amount
Trial Simulation	Hours	8,00
Simulation Case 1	Hours	12,00
Simulation Case 2	Hours	12,00
Simulation Case 3	Hours	14,00
Simulation Case 4	Hours	14,00
Simulation Case 5	Hours	22,00
Simulation Case 6	Hours	22,00
Simulation Case 7	Hours	22,00
Simulation Case 8	Hours	22,00
	Total hours	148,00
	Total Cost (EUR)	**66,60**

Budget Table 5: Simulation hours & Cost.

The cost of 148 simulation hours at a tariff of 0,45 EUR/hour resulted in 66,6 EUR.

2.5 Final Budget

Once the cost associated to the workforce, equipment, tangible assets and LRZ cluster has been calculated, the real cost of the total project can be obtained. To do this, first, the Material Execution Budget (MEB) is calculated. The MEB represents the sum of the items mentioned previously. However, the general expenses of light, water, furniture and additional material or equipment that is also consumed during the Thesis completion is not considered in the MEB. Therefore, these general expenses are accounted for as 15% of the MEB and also included in the Investment Budget.

As a last step, a 21% VAT (Value Added Tax) has to be added to the final Investment Budget and the Final Project Budget is calculated.

Concept	**Total Cost (EUR)**	
Workforce		10.813,32 €
Equipment		403,51 €
Tangible Assets		40,00 €
LRZ Cluster		66,60 €
MEB (Material Execution Budget)		**11.323,43 €**
General Expenses (15%)	1.698,51 €	
Investment Budget		**13.021,95 €**
VAT(21%)	2.734,61 €	
Total Budget		**15.756 €**

Budget Table 6: Final Project Budget.

Therefore, the Total Budget of the Thesis "Study of the Set Up of a FSI between PWR fuel assemblies and the reactor coolant" mounts to:

#Fifteen thousand seven hundred and fifty-six#

Valencia, March 2017.

Signed: Jaime G. Ruiz Antón-Pacheco.